Spatially Resolved Spectroscopy of Faint Star-Forming Galaxies & their Environments in the High Redshift Universe

Mairéad Hurley B.Sc.

A Thesis Submitted for the Degree of
Doctor of Philosophy

December 2010

School of Physical Sciences, Faculty of Science & Health
Dublin City University, Ireland

Research Supervisors: Dr. Brenda Frye & Dr. Turlough Downes

I hereby certify that this material, which I now submit for assessment on the programme of study leading to the award of PhD is entirely my own work, that I have exercised reasonable care to ensure that the work is original, and does not to the best of my knowledge breach any law of copyright, and has not been taken from the work of others save and to the extent that such work has been cited and acknowledged within the text of my work.

Signed:

ID No.: 56124813

Date: 30th November 2010

Contents

List of Figures

List of Tables

Abstract

Spatially Resolved Spectroscopy of Faint Star-Forming Galaxies & their Environments in the High Redshift Universe

by

Mairéad Hurley

Dublin City University

This thesis is concerned with the spectroscopic observations of distant galaxies, $1 < z < 5$. The galaxies presented here are intrinsically faint such that their flux is dominated by ordinary star formation rather than galaxy-galaxy merging and/or strong nuclear activity. Such studies are normally untenable owing to the faintness of this type of galaxy. The approach used in this work is to select objects gravitationally-lensed by massive foreground clusters of galaxies. Cluster lensing boosts galaxy brightnesses by factors of ten or more whilst simultaneously magnifying the object size, allowing for the detailed study of ordinary objects at high redshift. We present spectroscopic data for a strongly-lensed galaxy at $z = 0.79$ from which we measure the physical conditions in the interstellar medium and characterise the star formation history/activity. Significant spatial variations in its star formation activity and metallicity are apparent. We also present evidence for an overdensity of neutral hydrogen in the vicinity of a galaxy at $z = 4.9$, which we interpret as gas infall onto an object which still has yet to accumulate the bulk of its gas mass. A study of the field of the lensing cluster Abell 1689 is presented, which utilises the excellent spatial resolution of the G800L grism on board the Hubble Space Telescope. Observations of two Einstein Ring galaxies at $z \sim 2 - 3$ are also presented, with the spectrum of one of these displaying evidence for large scale gaseous outflows. Studies such as these are crucial for understanding the physics governing young galaxies as they form. These results are discussed in the context of the current paradigm of galaxy evolution.

Acknowledgements

Firstly, I'd like to thank Brenda Frye, my primary supervisor who has been a constant source of encouragement, good ideas, advice and guidance all through my time at DCU. I'm extremely grateful for all the opportunities she has given me, particularly the chance to spend some time working with her in San Francisco in 2010, which was extremely beneficial to my thesis work. I'd also like to thank my co-supervisor Dr. Turlough Downes, who has been very supportive, and was always available to lend an ear and give me advice and encouragement. I'm very grateful to all the staff and co-students in the NCPST and the physics department in DCU. Also thanks to the Science Foundation Ireland and the Physics Department for paying me while in Ireland, and the University of San Francisco for funding my trip there. I have to thank my collaborators-Dan Coe for all the photometry, and chats over beers in Valencia. Sangeeta Malhotra and James Rhoads for Magellan time. Evan Kirby and Raja Guhathakurta for Keck time, and particularly to Raja for all his help on the science side also, and encouraging words! Thanks to Steven Finkelstein and Brad Holden for SED help during my shaky early days. Also thanks to Ivo Labbé for IMACS help and scripts and always being kind enough to reply to pesky emails full of questions from me.

I'd like to thank the folks in Galway from my undergraduate days there. On the teaching side Ray Butler, Matt Redman, Aaron Golden & Mike Redfern who gave me so much help and encouragement. Likewise Gregg Hallinan and co. in the IT Department postgrad office in my summer there. For all the craic over the years as well as a small bit of studying, I have to thank my co-conspirators in the Physics and Astronomy course in Galway, in particular Aisling, Ronan, Enda, Brian, and of course Cathal and John by default even though they're technically pesky engineers. I still remember that "Mercury, Venus, Earth, and Mars are the four terrestrial planets" (with a little melody to match the words) ever since a very late night sing song in Grattan Park so turns out I learned at least one bit of astronomy through you lot!! Huge thanks to Liz who has been a great friend, linked as we are through music and physics, and even though she's still in Galway we've never been too far apart thanks to gmail chat, so I owe her a big thank you for all the rants, gripes and moans she's had to listen to about the hard life of a PhD student, and all her good advice on above topic!

I have to express my gratitude to the people I met at the Carnegie Observatories back in 2005, who inspired me to take the plunge and start my PhD in astronomy-Barry Madore, Wendy Freedman, and all the postdocs there, especially Daisuke Kawata, Ivo Labbé and Kurt Adelberger.

Thanks to all the folks I've shared an office with here in DCU who have made life a little more bearable on grey, rainy, Dublin days-thanks Ruth, Paddy, Conor, Daragh and recently Matt, and all our neighbours from the offices either side who pass through now and again-Mossy, Conor, Jiang Xi, Colm, Éanna, Séamus, Joe, Jack and Catherine. Sincere apologies to the boys for the amount of time Ruth and I spent discussing knitting, recipes, Ruth's wedding plans, and in general wrecking your heads with girlie talk-and covering a wall with pictures of meaty-faced handsome men! Have to say I enjoyed all the chats and craic though! Also thanks to the students who have now moved on, reminding me that finishing this thing is definitely possible-Phil, John, Ricky, Padraig, Caroline and Eoin to name but a few!

Above all, I want to thank all my friends & family for putting up with me for the past few years. Well done to my parents for learning to deflect the question from elderly neighbours wanting to know "is she qualified yet?" or "but what will she be qualified FOR?" You've both been so supportive of me all through the years and I really can't put into words how grateful I am for everything you have done for me. Thanks also to my lovely siblings who now have nothing to live up to after the eldest had to spend 21 years in school - so cheers Dermot, Eileen, Deirdre and Seán. Also thanks to Granny, Roisin, all the O'Callaghans, and all on the Hurley side.
Conal, you're finally getting your mention-not going to write a chapter about you as you requested, but thanks for being so patient and supportive and for always asking "How are the stars?" and for generally taking my mind off all the bad things and always making me laugh! Thanks as well for keeping me sane and for putting up with my incessant whining and failure to make dinner while writing up, I'll never moan again I promise! And for telling people I was

studying star signs, and was going to be qualified to write a horoscope column, cheers for that one!

Finally thanks to all the rest of the gang for providing constant distraction and forcing me away from my studies now and again even though that was a difficult feat to achieve - Jacqui, Joan, Liz, Lorraine, Siobhan, Sarah, Caroline, Brian & Fiona and all the rest, thanks for all the tunes and laughs and road trips, here's to many more! And speaking of road trips, thanks to Galldubh for bringing me to Germany this year, every time I read the one line of this thesis I wrote while on the tour bus I think fondly of all the great plans I had for those three weeks! Some of those great plans were definitely scuppered by a combination of the German police, St. Patrick's Day and a bus load of drunk mullet-headed skiers/80's soap stars, I would have written loads that day if it wasn't for them! I also have to say a special thanks to Colm Green for sitting me down, feeding me and talking me out of giving up on this PhD business when I was very close to doing just that! So many more friends I'd like to acknowledge but I'm running out of space but needless to say, thanks to you all for everything, and if you're actually reading this....I'd recommend putting it down right about now, it's all downhill from here on in!!

1

Introduction

1.1 Thesis Motivation

This thesis is concerned with the study of star-forming galaxies across a range of redshifts(z), from the early Universe at $z \sim 5$ to the relatively recent at $z \sim 1$. Questions surrounding the exact nature of the processes involved in galaxy formation and the evolution of structure growth in the Universe remain unresolved, with a number of open issues yet to be addressed. A fundamental goal is to understand completely how the complex objects that surround us today at $z = 0$ grew from the tiny perturbations in the all-pervasive Cosmic Microwave Background. Star-forming galaxies represent valuable tracers of this cosmic history. The addition of new data to the already-accumulated reservoir of knowledge about the distant Universe is key to pushing the boundaries of our understanding, and unlocking the answers to these mysteries. Observational data is paramount, as it can be crucial in demonstrating the validity of theoretical hypotheses and constraining inputs to simulations. As recently as 1998-1999, the observations of Type Ia supernovae by two independent groups, (Perlmutter et al. 1999; Riess et al. 1998) have shown that supernovae at cosmological distances are ~ 0.25 magnitudes dimmer than they would be in a decelerating Universe, proving the positive, non-zero nature of the cosmological constant ($\equiv$ vacuum energy density Ω_Λ) and thus proving that the expansion of the Universe is accelerating. This discovery has led directly to the current most widely-held cosmological model - the inflationary ΛCDM (Λ Cold Dark Matter) Universe, composed of $\sim 4\%$ baryons, $\sim 22\%$ dark matter, and $\sim 74\%$ dark energy. The dark energy term is accounted for in this model by the cosmological constant, and implies that the majority of the energy density budget of the Universe is dominated by a unknown form with a large negative pressure. This model accounts for a number of observed properties of the Universe such as the cosmic microwave background (CMB) and large scale structure; however, the fundamental questions regarding the nature of dark energy and dark matter remain unanswered.

In this currently-accepted paradigm, our Universe was created in the Big Bang, and for the following fractions of a second, the temperature and density were enormous, but rapidly decreasing. At 10,000 years after the Big Bang, the Universe was a “primordial soup” - with electrons, protons and photons moving around in an environment which was constantly cooling and expanding. An atom would form, a photon would immediately destroy it, and this loop continued for about 380,000 years until the temperature dipped to below 3000K, at which point the plasma of free nuclei and electrons could condense to form atoms. As no further scattering of the radiation could occur without the free electrons required for Thomson scattering, the matter and radiation were decoupled, and the Universe became matter-dominated. This point in time is known as the last scattering surface, as the Universe became transparent to radiation. During this epoch of recombination, protons and electrons formed atoms, whilst the photons were granted a sudden increase in mean free path length and became free to hurtle through space and time towards us. These relic photons were constantly cooled as they did so, and at the present day are observed at microwave wavelengths, as what is known as the cosmic microwave background (CMB). The CMB has been very accurately mapped by the Wilkinson Microwave Anisotropy Probe (WMAP), which recently presented the results of 7 years of integration (e.g. Komatsu et al. (2010)). The CMB is isotropic to 1 part in 10^5, but it is these tiny anisotropies observed in the early Universe which are the seeds for subsequent structure growth. The tiny density and temperature perturbations became amplified by gravity, and so these regions which started out slightly denser than the average began to contract, as the gravitational forces in these regions were also slightly stronger than average. These contractions continued for hundreds of millions of years until within them, the first stars and galaxies were born. The cosmic density of matter Λ_m is hugely dominated by an unknown form of matter called “dark matter”, accounting for 84% of the matter in the Universe at the present day (Loeb 2007). The presence of dark matter (DM) has been inferred observationally from flat rotation curves of galaxies, the structure of galaxy groups and clusters, X-ray measurements of the mass-to-light (M/L) ratio of galaxy clusters, and gravitational lensing results. A small fraction of DM can be made up of baryons, and the recent success of the OGLE and MACHO surveys of gravitational microlensing in the Milky Way halo have provided observational evidence for the existence of baryonic dark matter in the form of Massive Compact Halo Objects (MACHOs). However, the majority of DM must be non-baryonic, and the nature of the particles comprising it are still undetermined, but thought to be weakly interacting elementary particles. These DM particles can interact with each other and with other particles only through gravity, and also do not emit or absorb radiation. In the early Universe, this DM was only affected by gravitational forces, and so the gravitational Jeans instability which causes structure to form by collapse of self-gravitating systems was not opposed by a radiative pressure force and so DM rapidly began to clump into condensations which are known as dark matter haloes. In this nascent Universe populated by DM haloes, DM perturbations can grow to such an extent that one region of space may become significantly more dense than the mean density, and it is in these overdensities that stars begin to form. The first stars (Population III stars) are as yet undetected, but are thought to be massive, short-lived objects which exploded and enriched their surroundings with metals. Galaxies began to take shape, and the first quasars (QSOs) lit up. Both of these populations of bright young objects provided a source of UV radiation which gradually caused a phase transition in which the intergalactic medium (IGM) went from being fully neutral to almost fully ionised. The epoch of this transitional phase is known as the epoch of reionisation. The nature of the sources which initiated and drove the reionisation process are not fully known, but a widely-accepted scenario is one in which reionisation began with expanding spheres or bubbles of ionised gas around each galaxy, until the bubbles overlapped, and the entire Universe became ionised, and transparent. This process took place between $z \sim 17$ & $z \sim 6$. The studies of absorption due to neutral hydrogen along the line of sight toward QSOs (e.g. Fan et al. (2006); Becker et al. (2007)), and the evolution and clustering of Lyman-α emitting galaxies (Malhotra and Rhoads 2004) indicate that reionisation proceeded inhomogeneously, and was most likely reaching the overlapping stage prior to completion close to $z \sim 6$. Results from the WMAP 5-year data indicate a significantly higher reionisation redshift of $z = 10.4 \pm 1.4$ (Komatsu et al. 2009). Future low-frequency studies of the 21-cm transition of neutral hydrogen aim to explore the ionisation history of the Universe to even higher redshifts of $z \sim 6 - 15$ (see e.g. Loeb (2007); Pritchard et al. (2010) for discussion). Recent studies of the space density of quasars at high redshifts show a decline in their number at the highest redshifts. This indicates that ordinary star-forming galaxies must have provided a large fraction of the photon budget required to ionise the IGM and must continuously do so to the present day in order to keep the IGM in the high state of ionisation in which it is observed since the completion of reionisation. The question of how a galaxy can produce UV photons which can escape the galaxy into the IGM without being absorbed by the neutral hydrogen within the galaxy is a fundamental one, and to date only a small number of observations of the escaping photons have been made (e.g. Iwata et al. (2009), Steidel et al. (2001); Shapley et al. (2006)). It is clear that ordinary galaxies have played a crucial role in shaping our Universe, and observational studies of the diverse galaxy population across a wide range of redshifts play an essential role in determining the processes involved in shaping the Universe as we see it today.

Galaxy formation is a process which extends from the early stages of the Universe to the present day. The classic picture of galaxy formation outlined in seminal papers such as Rees and Ostriker (1977), White and Rees (1978) and Silk (1977) involves gas falling into dark matter haloes, becoming shocked and heated to the virial temperature. For a galaxy with a mass similar to that of the Milky Way, the shocked gas reaches a temperature of $\mathrm{T}_{vir} \sim 10^6$K. In the dense inner regions of the haloes, this gas efficiently radiates its thermal energy, loses its pressure support and settles into compact disks where it can form stars. In recent years, this picture has been modified with the introduction of the idea of cold mode accretion. Analytical and hydrodynamical simulations have revealed that most of the gas is never strongly shocked as it flows toward the central forming galaxy-it accretes instead in a filamentary cold mode maintaining a temperature of 10^5 K (e.g. Kereš et al. (2005); Dekel and Birnboim (2006)). These authors show that the cold mode dominates in galaxies with masses $\lesssim 2 \times 10^{10} M_\odot$, and completely dominates high redshift accretion at all masses. This picture is in agreement with a ΛCDM cosmology. In such a cosmological model, structure is built in a hierarchical manner. Galaxies form at the centre of dark haloes as gas cools, condenses and fragments into stars. Larger early-type ellipticals are formed relatively late from mergers between late-type spiral galaxies of similar mass (De Lucia et al. 2006), while the largest virialized objects, galaxy clusters, form later as galaxy haloes aggregate into more massive systems. These clusters of galaxies are arranged into a larger-scale pattern of filaments, separated by huge voids. This so-called "cosmic web" is observed in deep galaxy surveys, and is also reproduced by galaxy formation simulations such as the Millennium simulation (Springel et al. 2005), which is based on the cosmological parameters of a ΛCDM Universe, as well as observed properties of galaxies. The excellent agreement between the observed clustering and simulations is shown in Figure 1.1, reproduced from Springel et al. (2006). The left and top wedges (blue) represent the galaxy distribution obtained from large spectroscopic surveys-the Two-degree Field Galaxy Survey (2dFGS, left) and the Sloan Digital Sky Survey (SDSS, top). These bear a striking similarity to the mock catalogues constructed from the Millennium simulation shown in the bottom and right (red) wedges. Observations can also help to probe fundamental scales for galaxy formation. Recent models by Muñoz and Loeb (2010) of observations of ~ 100 galaxies at redshifts of $z = 7-8$ taken with the Wide Field Camera 3 (WFC3) on board Hubble Space

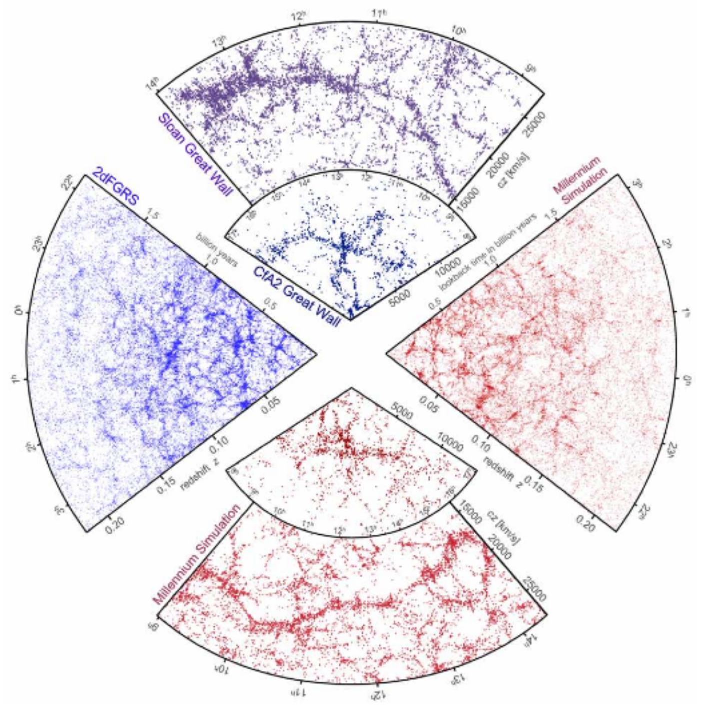

Figure 1.1: *Large-scale galaxy clustering observed by galaxy surveys, compared with the results from a simulated Universe. Image taken from Springel et al. (2006).*

Telescope (HST) shows a minimum halo mass per galaxy of $\sim 2.5 \times 10^9 M_\odot$, with a suppression of galaxy formation in lower mass haloes. It is not yet clear why there is a preferred or characteristic mass scale for galaxies. Eyles et al. (2005) find that galaxies can have substantial masses of $10^{10} M_\odot$ as early as $z = 6$, and time scales of star formation at $z = 6$ have been shown to be as long as 200-300 Myrs (Labbé et al. 2006), suggesting that galaxies were actively forming stars and building up mass while the process of reionisation was still ongoing. HST WFC3/IR has recently been used to detect a sample of galaxies at $z \sim 7 - 8$ (Bouwens et al. 2010) with substantial ages (>100 Myrs), indicating a possible onset of star formation as early as $z > 10$ (Labbé et al. 2010).

The results of a galaxy formation model such as the Millennium simulation (Figure 1.1) are tied innately to its ability to simultaneously combine the best known values for the cosmological parameters with the observed properties of galaxies. In-depth studies of ordinary star-forming galaxies such as the ones described in this thesis increase the wealth of available data which characterises the galaxy population at a particular redshift. The spectroscopic studies of high-redshift galaxies are frequently hampered by the distance and faintness of the sources involved, and the constraints of the telescopes used to observe them. In general, studies of such galaxies are limited to large volumes of poorly resolved data, which can often provide important information about the general properties of a class of galaxies, but are insensitive to the subtle variations between individual objects. This thesis is concerned with small volumes of high quality data which allows the study of such variations. The study of these individual objects is realised despite their intrinsic faintness thanks to the gravitational lensing effect. Lensing boosts the brightness of the background source, and because surface brightnesses are conserved, also increases object sizes. The observed lensing effect also provides a powerful means to study the mass distribution of the lens. Some of the strongest observational evidence for dark matter comes from the study of the mass distribution of gravitational lenses. Constrains on the dark energy equation of state parameter w_x have recently been tightened by Jullo et al. (2010), who utilise multiple images formed by gravitational lensing towards the massive cluster A1689 to create a parametric model which simultaneously constrains the cluster mass distribution and the equation of state for dark energy. These constraints are combined with those from X-ray clusters and WMAP 5 year data, and are consistent with results from other methods. This result reduces the 2σ contours on the dark energy equation of state parameter w_x by $\sim 30\%$. The basis of this approach is that the position of multiple images in the field of a massive lensing cluster (see Chapter 2) are strongly dependent on the distribution of the mass in the lensing cluster, whilst simultaneously being tied to the cosmology-dependent angular-diameter distances between source, lens and observer. Combining the positions and redshifts of a number of multiple images of an array of background sources allows the derivation of constraints on Ω_m and w_x. The multiply-imaged galaxy at $z = 4.9$ which is the topic of Chapter 5 is one of the 12 multiply-imaged galaxies used in the work of Jullo et al. (2010), proving the utility of high S/N spectroscopic studies in cluster fields for cosmology as well as to explore galaxy formation and the IGM.

1.2 Thesis Outline

The outline of this thesis is as follows:

Chapter 2: **Gravitational Lensing**

This chapter will provide a brief overview of the topic of gravitational lensing. All of the galaxies I have studied have been magnified due to gravitational lensing, which arises from the deflection of the light from a distant object as it impinges on the gravitational potential of an intervening massive structure in the Universe. This effect can significantly boost the brightness and size of the distant background source.

Chapter 3: **Observations**

This thesis is largely based on observational data from both ground and space based telescopes. This chapter contains a detailed description of each of the observations used directly in this work. Some of the datasets have been been provided by collaborators, while I have been directly involved in the planning and observations of the Magellan and Keck datasets outlined in this chapter.

Chapter 4: **Reduction of Multislit and Longslit Spectroscopic Data**
The analysis of spectral data from distant galaxies first requires the careful extraction of the faint, background-limited signal from the raw images which are output by the telescope. In order to achieve this aim, I developed a custom-built data reduction code which is outlined in this chapter. This describes the steps involved in reducing the data acquired from the observations outlined in Chapter 3.

Chapter 5: **A Gravitationally Lensed Galaxy at $z = 4.9$: Results**
In this chapter I present and analyse the spectroscopic data acquired for a distant red galaxy at $z \sim 5$ in the field of the massive galaxy cluster Abell 1689. The huge mass of the galaxy cluster makes it an extremely effective gravitational lens, and the distant galaxy in question has had its flux boosted by a factor of ~ 10. An in-depth look at a star forming galaxy at such a high redshift is a rare phenomenon, facilitated by this lensing effect. This chapter also presents measurements of the neutral hydrogen content in the environment of this galaxy, as well as the technique used to determine the spectral energy distribution of the galaxy with the evolutionary stellar population synthesis models of Bruzual and Charlot (2003).

Chapter 6: **Hubble Space Telescope Grism Survey of Galaxy Cluster Abell 1689**
The field of the massive galaxy cluster A1689 was observed using the G800L grism on board the Hubble Space Telescope's Advanced Camera for Surveys. This chapter presents an analysis of the grism spectroscopy obtained for 42 galaxies in a flux-limited sample with $i_{775} < 27.3$.

Chapter 7: **Detailed Spectroscopic Analysis of a Strongly Lensed Galaxy at $z = 0.79$**
The grism observations presented in Chapter 6 revealed three spatially resolved star-forming regions in a gravitationally-lensed galaxy at $z = 0.79$. Chapter 7 presents the analysis of further spectroscopic data of this galaxy which was acquired at the Keck and Magellan telescopes. The spectral features are used to infer characteristics of the galaxy, and to examine variation across the spatial extent of the galaxy.

Chapter 8: **VLT Observations of Two Strongly Lensed Lyman Break Galaxies**

This chapter begins with an overview of Lyman-Break Galaxies (LBGs), which are ordinary star-forming galaxies at redshifts $z \sim 2-5$, representative of the epoch when star formation was at its peak of activity in the history of the Universe. Whilst substantial numbers of LBGs have been discovered to date, the large distance and the intrinsic faintness of the sources render observations challenging, and detailed studies of such galaxies can only be obtained by observing examples of this class of galaxy which have been gravitationally lensed. The number of known cases of lensed LBGs is tiny in comparison, < 20. This chapter presents the observations of two such galaxies at $z \sim 2.4$ and $z \sim 3.6$.

Throughout this thesis, the cosmological parameters assumed are as follows: $H_0 = 70$ km s^{-1} Mpc^{-1}, $\Omega_{m,0}$=0.3, and $\Omega_{\Lambda,0}$=0.7. All magnitudes quoted are in the AB system (Oke and Gunn 1983), unless otherwise stated.

2

Gravitational Lensing

2.1 Gravitational Lensing

All of the galaxies studied in this work have been made more accessible to the observer due to the phenomenon known as “gravitational lensing”. This chapter begins with an introduction to lensing, and a review of recent progress. For a more in-depth theoretical treatment of lensing, the reader is directed to the excellent reviews by Blandford and Narayan (1992) and Narayan and Bartelmann (1995).

2.1.1 Lensing Theory

Gravitational lensing is a prediction of Einstein’s General Theory of Relativity, and arises due to the fact that gravity can deflect light rays. The deflection of light due to the gravitational effect of massive bodies is a phenomenon which was first confirmed observationally in 1919, when a total solar eclipse meant that measurements could be taken of the relative positions of background stars close to the Sun. The effect of lensing is manifold- as well as shifting the observed location of a single background source, it can also cause magnification, distortion of the image, and the creation of multiple images of the source. For the effect of such lensing to be observed, there must be a relative alignment between source, lensing mass and observer. A photon emitted from the source in the direction of the observer must pass close to the massive intervening lensing object on its path toward the observer. The photon is accelerated towards the lens due to its gravitational potential. This results in a shift in the observed position of the source. The idealized layout is shown in Figure 2.1, adapted from Narayan and Bartelmann (1995), Figure 5. The source emits a

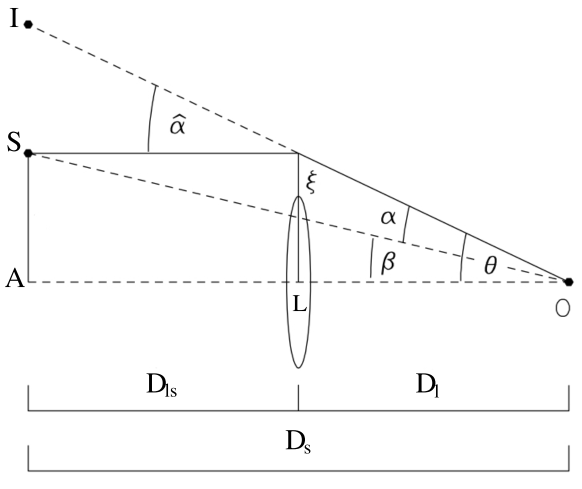

Figure 2.1: *Schematic layout of gravitational lensing situation, adapted from Narayan and Bartelmann (1995). The light ray from source S travels toward the observer, and encounters the thin lens L at impact parameter* ξ*, which causes its path to be deflected by the deflection angle* $\vec{\hat{\alpha}}$*. This means the observer sees the image at position I. The angle between the optic axis A and the true source position is given by* β*, while the angle subtended by the optic axis and the image is* θ*. The reduced deflection angle* α *is then given by* $\vec{\beta} = \vec{\theta} - \vec{\alpha}(\vec{\theta})$*. The angular diameter distances between observer and source (*D_s*), lens and source (*D_{ls}*) and lens and observer (*D_l*) are also shown.*

light ray which impinges on the lens at a distance or impact paramter ξ from the arbitrarily defined optic axis A. The ray is deflected by angle $\vec{\hat{\alpha}}$, creating an image which is deflected by an angle $\vec{\theta}$ from the optic axis. In terms of the mass M of the lens (assumed to be circularly symmetric in this case), the deflection angle is described by $\vec{\hat{\alpha}} = 4\mathrm{GM}(\xi)/\mathrm{c}^2\xi$. The angle between the optic axis and the true source position is $\vec{\beta}$. The reduced deflection angle is given by $\vec{\alpha} = (\mathrm{D}_{ls}/\mathrm{D}_s)\vec{\hat{\alpha}}$. The distances shown in Figure 2.1 are angular diameter distances, which are distances defined so that the relation "separation = angle × distance" holds, even in curved spacetime. As can be seen in Figure 2.1, $\theta\mathrm{D}_s = \beta\mathrm{D}_s$ - $\hat{\alpha}\mathrm{D}_{ls}$, and the lens equation can be inferred:

$$\vec{\beta} = \vec{\theta} - \vec{\alpha}(\vec{\theta}) \tag{2.1}$$

The lensing depends strongly on the surface mass density of the lens, which in real astrophysical systems is not always constant. The lens equation is a mapping $\theta \rightarrow \beta$ from the lens plane to the source plane, but in general this is non-invertable; for a single source position $\vec{\beta}$ there can be multiple solutions corresponding to multiple image locations $\vec{\theta}$. If we describe the projected distance ξ in terms of angular distance we have $\xi = \theta \mathrm{D}_l$ and we can write the lens equation:

$$\beta(\theta) = \theta - \frac{D_{ls}}{D_l D_s} \frac{4GM}{c^2 \theta} \tag{2.2}$$

In a scenario where the source, lens and observer are perfectly aligned, the source lies exactly on the optic axis and $\beta = 0$. In this scenario, the source is imaged as a ring, known as an Einstein ring. In such a case, we can write the lens equation in terms of the radius of the ring, known as the Einstein radius:

$$\theta_E = \left[\frac{4GM(\theta_E)}{c^2} \frac{D_{ls}}{D_l D_s} \right]^{1/2} \tag{2.3}$$

These chance alignments are rare in nature, and aberrations in the lensing systems such as an asymmetric mass distribution in the lens can serve to further reduce the chances of observing such a phenomenon, but a number of almost-complete Einstein Rings have been observed, including those described in Chapter 8. An image of such a system is shown in Figure 8.3. The Einstein radius is an important parameter for a lensing system. Multiple imaging tends to occur only for sources within the radius, and any sources inside it experience strong magnification compared to objects outside. One useful property of a gravitational lens is that the imaged source has its brightness and color preserved, since the geometry of a light path is independent of wavelength. However, the image can be distorted in one of two ways-it can be magnified, and it can be stretched. The apparent solid angle of a source is changed by lensing, and so magnification can be simply defined as the ratio between the solid angle of the image and the source - magnification = image area / source area. The magnifiction μ is given by

$$\mu = \frac{\theta}{\beta} \frac{d\theta}{d\beta} \tag{2.4}$$

The distortion of the source with coordinates β_i to image θ_j is given by the Jacobian or distortion matrix $\mathcal{A}_{ij}$:

$$\mathcal{A}_{ij} \equiv \frac{\partial \beta_i}{\partial \theta_j} = \delta_{ij} - \phi_{,ij} = \begin{pmatrix} 1 - \kappa - \gamma_1 & -\gamma_2 \\ -\gamma_2 & 1 - \kappa + \gamma_1 \end{pmatrix} \tag{2.5}$$

The parameter κ, the convergence, controls the image size and is related to the lens surface mass density. $\gamma = \gamma_1 + i\gamma_2$ is the complex shear which controls the distortion. $\phi_{,ij}$ is the cosmological lensing potential. The set of points in the source plane which have $det\mathcal{A}_{ij} = 0$ have formally infinite magnification and is called the caustic. The corresponding set of points in the image plane is known as the critical curve. Objects lying on or close to a caustic in the source plane are very strongly magnified.

2.1.2 Gravitational Lensing in Observational Astronomy

In recent decades, gravitational lensing has become an exceptionally useful tool in various aspects of astrophysics. While the theory and astrophysical applications had already been developed in the 1960s, it did not enter the realm of observational astronomy until 1979, with the discovery of a multiply imaged quasar (Walsh et al. 1979). In general, lensing which produces multiple images of a background source is described as "strong" lensing. Most multiply imaged quasars and Einstein rings detected thus far are examples of galaxy-galaxy lensing- where the imaging is caused by the lensing effect of a foreground galaxy. In the case of the two Einstein rings described in Chapter 8, the lenses are massive elliptical galaxies at $z \sim 0.4-0.5$. The galaxies at $z \sim 5$ and $z \sim 0.8$ described in Chapters 5 and 7 have been gravitationally lensed by a significantly larger mass lens; a galaxy cluster. Galaxy clusters are the largest virialized bound mass structures in the Universe with typical masses of M $\sim 10^{14} - 10^{15} M_{\odot}$. Galaxy clusters are dominated by elliptical and S0 galaxies, with a much lower fraction of spiral galaxies than is observed in the field. The intracluster medium is also extremely bright at X-ray wavelengths. Such huge structures allow large scale lensing with extremely large Einstein radii. Rich clusters with a central mass concentration can produce giant arcs, which are formed when a background galaxy is aligned with one of the caustics. Less dramatic smaller arcs are also observed. A cluster field often hosts a large number of background images which are magnified and distorted by varying amounts depending on their proximity to the caustic and their alignment with the cluster. Objects which are weakly distorted and magnified are described as arclets. The location of the source with respect to the caustic will also determine how many images of the galaxy should be observed. The positions of the multiple images depend strongly on the lens mass distribution. In general, odd numbers of images are produced by nearly every source position (Burke 1981), but one of these is a centrally located demagnified image which usually cannot be observed. In general though, at least one of the images will be magnified (Schneider 1984). The $z \sim 5$ galaxy described in this work is an example of a multiply-imaged galaxy, with two definite image detections made. As the gravitational field of a lens is independent of the state and nature of the matter generating it, gravitational lensing is an ideal tool for studying the total matter in cosmic objects, both luminous and dark. Lens models can be used to constrain the mass in the inner part of the lensing galaxy or cluster. In the case of galaxy-galaxy lensing, substructure can be detected and studies made of the interstellar medium (ISM). Much progress has been made in the field of recovering the mass profiles of clusters from lensing constraints. In order to obtain accurate mass estimates, detailed models must be obtained by fitting galaxy image positions and fluxes. A simple mass model for a lens is a Singular Isothermal Sphere (SIS); however, this is an over-simplification, and any realistic lens model requires an elliptical mass distribution and an external shear. Cluster models will often also include individual galaxy-scale potentials for the brightest cluster galaxy (BCG) and other large ellipticals. The galaxies described in Chapters 5, 6 and 7 have been detected in the field of the massive cluster Abell 1689 which lies at a redshift of $z = 0.188$. A1689 is one of the largest known clusters, with an Einstein radius of $\sim 50''$, and accordingly is one of the most well-studied clusters. A number of mass models of this cluster have now been produced by various groups, including those of Broadhurst et al. (2005), Limousin et al. (2007), Coe et al. (2010) and Jullo et al. (2010). The basic starting point for cluster mass models is the detection of multiple counter-images of a number of galaxies, allowing the positioning of the radial and tangential critical curves of the lens. As an example, Coe et al. (2010) report 135 images of 42 individual galaxies in A1689. The position of the critical curve can help estimate the position of further counter-images, and as more image pairs are detected, the more accurate this positioning becomes. With the critical curves in place, a mass-model for the cluster can be estimated and refined. A1689 consists of two groups of galaxies - a main one at the centre which is also the peak of the X-ray emission, and a secondary group located to the North-East. This can be seen in Figure 3.2.

Statistical studies of weakly lensed arclets in galaxy clusters also leads to mass estimates for clusters. Objects which are weakly lensed cannot be identified individually as lensed images, but the distortion can be identified statistically. Strong lensing probes the mass in the inner regions of clusters, while weak lensing can be used out to much larger angular distances from the centre of the cluster. The distortion from several arclets at different points in the cluster field can be averaged to determine the mass distribution of the cluster. The method pioneered by Kaiser and Squires (1993) produces a parameter-free mass map from the averaged distortions. Results for strong and weak lensing can be successfully combined to recover cluster mass profiles, e.g. Umetsu and Broadhurst (2008); Umetsu et al. (2010). As discussed in Chapter 1, cluster masses can in turn be used to constrain cosmological parameters such as the matter density parameter Ω_m, the cosmological constant density parameter Ω_Λ, the dark energy equation of state parameter w_x, and the normalization of the matter power spectrum σ_8.

Whilst not directly pertinent to this work, the gravitational lensing effect can also be studied in terms of small masses causing short term transient lensing effects. This so-called “microlensing” regime involves studying the light curves from background sources . Changes in the apparent brightness of the source can occur when a smaller intervening object such as a star or planet comes into relative alignment with the source and observer. In the microlensing regime, suitable background sources are stars in the bulge of the Milky Way or nearby galaxies such as the Large Magellanic Cloud (LMC) or M31, while the lensing objects reside in the halo of the Milky Way. These microlensing events occur on short timescales, and can be caused by lensing objects such as dwarf stars or planets. Microlensing has also proven the existence of baryonic dark matter in the halo of the Milky Way in the form of compact objects, through the success of experiments such as MACHO (MAssive Compact Halo Objects) and OGLE (Optical Gravitational Lensing Experiment).

3

Observations

3.1 Target Selection & Observations

Strong gravitational lensing by galaxy clusters can give a unique perspective on higher redshift galaxies which lie close in projection to the cluster, and whose brightness can be magnified due to the lensing effect. It is the further study of such high-redshift galaxies at high signal-to-noise (S/N) which provides the impetus for the observations described in this work. High S/N observations of individual galaxies at $z > 2$ have only been made for a handful of galaxies over a spread of redshifts. This means that the only view we have on the evolutionary state of the Universe at certain points in its history are dependent on the information available on a very limited number of galaxies, and these galaxies may not be representative of the Universe as a whole at that epoch. Hence, it is ever imperative to expand the reservoir of observational information on distant galaxies. The initial detection of lensed galaxies and redshift determination is generally made at low S/N, and futher observations must be made to determine properties of the galaxy as a whole. As described in Chapter 2, the massive cluster A1689 is a rich hunting ground for strongly lensed distant galaxies, and the observations described in Sections 3.1.1, 3.1.2 and 3.1.3 come from this field. The observations in Section 3.1.5 are examples of galaxy-galaxy lenses.

3.1.1 VLT Observations at $z \sim 5$

The subject of Chapter 5 of this work is a tangentially-stretched lensed galaxy at $z = 4.9$, which was initially reported in Frye et al. (2002), and was detected as part of a ground-based redshift survey. It was detected as a V-band dropout, with the Lyman-break at 1216Å shifted beyond the V band so that the galaxy is not visible in the V or bluer bands, but is detected in the I band (see Section 8.1 for further details on colour-selection, and Figure 8.1 for an image of this galaxy in 3 of the HST ACS filters). A colour-magnitude diagram (CMD) of the cluster and foreground and background objects is shown in Figure 3.1, with the chosen galaxy indicated by a red circle, and the cluster sequence ($z = 0.187 \pm 0.025$) indicated by blue diamonds.

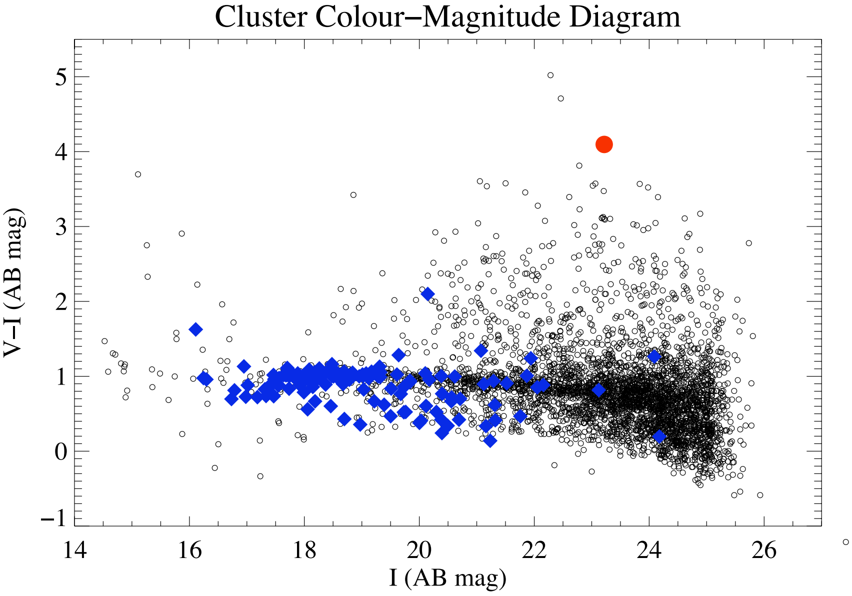

Figure 3.1: *V and I band colour-magnitude diagram for objects observed in the field of A1689, which shows that galaxy A1689-7.1 (larger red circle) has an extremely red colour. The galaxies comprising the cluster sequence ($z = 0.187 \pm$ 0.025) are shown with blue diamonds, while the black open circles represent background and foreground objects in the cluster field.*

This galaxy was designated A1689-7.1 in Broadhurst et al. (2005), who also find a radial counter-image (7.2) and tentatively detect a de-magnified central image (7.3). Figure 3.3 shows a false-colour image of A1689-7.1.

In order to make a detailed follow-up, spectroscopic observations of A1689-7.1 (henceforth 7.1), were made in June and July of 2001 at the Very Large Telescope (VLT) at the European Southern Observatory (ESO), Paranal, Chile. The instrument used was the Focal Reducer and low-dispersion Spectrograph (FORS2)[1]. FORS2 operates at optical and near UV wavelengths, and allows multi-object spectroscopy. The spectrum was acquired with an exposure time

---

[1] Details from `http://www.eso.org/sci/facilities/paranal/instruments/fors/doc/VLT-MAN-ESO-13100-1543_v85.pdf`

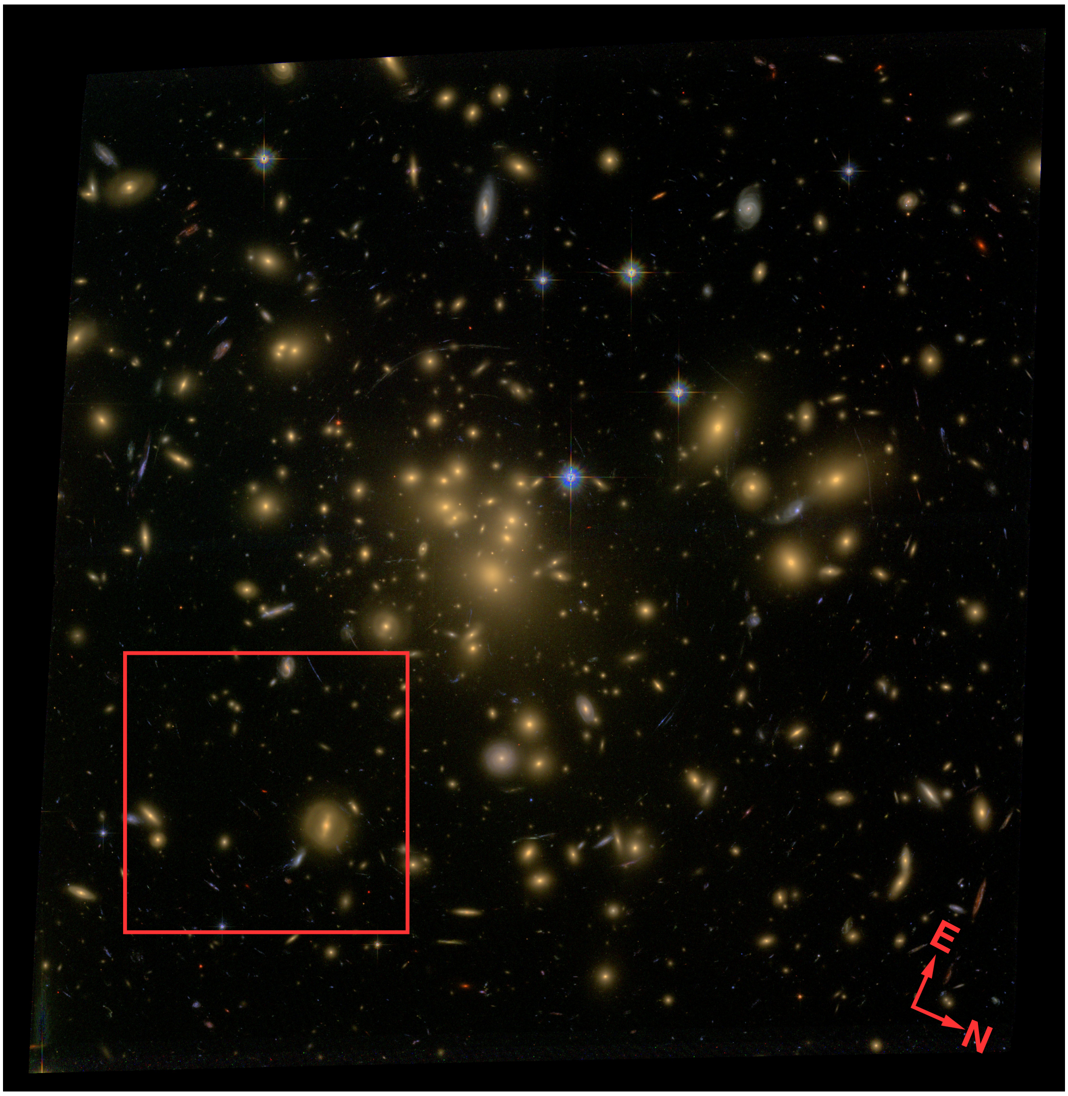

Figure 3.2: *A composite gri-band HST image of the field of galaxy cluster A1689, with the region containing A1689-7.1 highlighted in red. A close up of this region is shown in Figure 3.3. This image also shows the giant stretched tangential arcs which are a rough guide to the position of the Einstein ring for this giant gravitational lens. (Image credit: NASA, N. Benitez & ACS Science Team. (STScI 2003-01))*

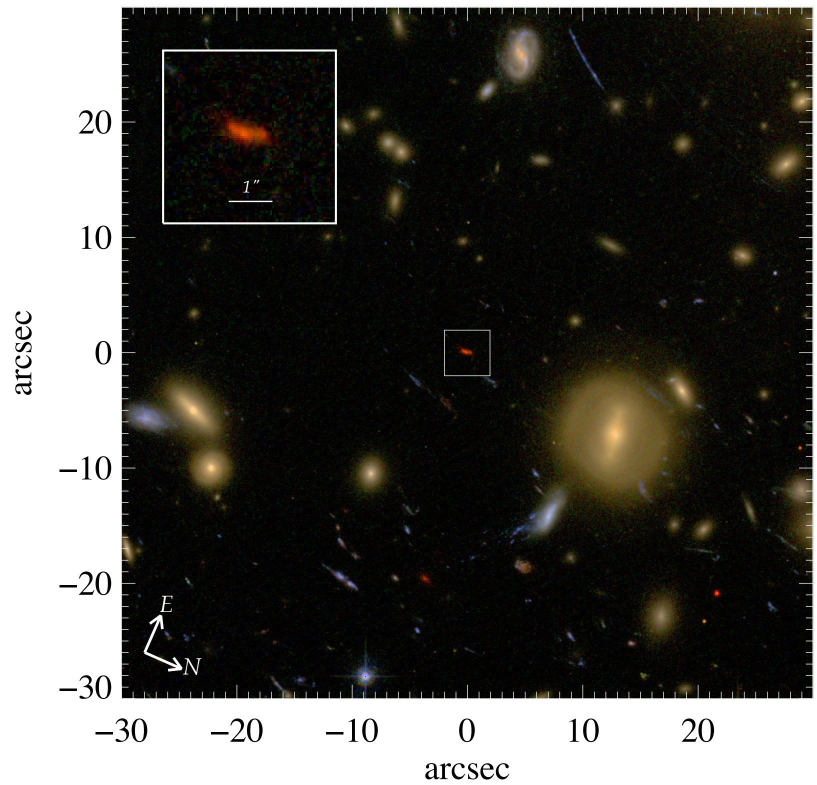

Figure 3.3: *A close up of the region highlighted in red in Figure 3.2, with a further close up of A1689-7.1. The scale bar indicates the tiny size of this galaxy, which has already been enlarged due to gravitational lensing, without which it would not be resolved with HST. The intrinsically red colour of the galaxy is evident. Image from Frye et al. (2008)*

of 14 hours with a spectral resolution of $R = \lambda/\Delta\lambda \approx 530$ measured from unblended skylines. 42 exposures of 1200 seconds each were made through a slit of $1\farcs0$ width, and a dither of $1\farcs0$ was applied between exposures in order to correct for fringing or uneven illumination along the slit. The observations were made with the telescope in service mode, using one multi-slit mask with the 300 line mm^{-1} grism. A series of zero second bias frames were taken. Flat field frames and Helium-Neon-Argon arc lamp exposures were also taken.[2] The reduction of these extremely background-limited spectroscopic data is outlined in Chapter 4, with results shown in Chapter 5.

3.1.2 Grism Observations of A1689

While galaxies at certain redshifts may be preferentially targeted by colour selection, for example Lyman Break Galaxies (LBGs) at z $\sim$ 3 (Steidel et al. (2003), see Section 8.1), grism spectroscopy allows the observer to simultaneously target all objects in a field of view in an unbiased way. A grism is a combination of a grating and a prism, aligned to keep light of a chosen wavelength undeviated as it passes through the dispersing elements. The light from any luminous object in the field of view is dispersed into a spectrum. In this way, multiple spectra are created without the need for a slitmask. The obvious drawback is that spectra from multiple objects can overlap, or higher orders of a spectrum can fall on the spectrum of another object. However, dedicated software has been developed for the optimal extraction and processing of slitless spectroscopy and is able to effectively recognise, and where possible correct for such inherent issues. The use of multiple position angles of the telescope during a given observations also helps to compensate for the field crowding. While grism spectroscopy typically has a very low spectral resolution, it has a high spatial resolution, and hence is extremely useful as a tool to survey large portions of the sky. This technique has been utilized in deep surveys including the “GRism ACS Program for Extragalactic Science (GRAPES)” survey of the Hubble Ultra Deep Field (Pirzkal et al. 2004), and the “Probing Evolution and Reionization Spectroscopically (PEARS)” survey of the GOODS north and south fields, (Malhotra and PEARS collaboration 2007). Chapter 6 describes the analysis of slitless spectra of a number of galaxies in the field of the cluster A1689. The centre of the cluster was observed for 7.1 ks - 3 orbits

---

[2] The standard bias, flat field and arc lamp frames are taken for all spectroscopic data presented in this chapter, and hence will not be mentioned again in forthcoming sections.

of the Hubble Space Telescope (HST) using the Advanced Camera for Surveys (ACS) and the G800L grism. The HST ACS field of view in the F775W filter is shown in Figure 3.4, with the galaxies successfully detected using the G800L grism circled. The observations were made by Dr. Gerhardt Meurer (ICRAR, University of Western Australia), who also carried out initial data reduction using the STScI ACS CCD CALACS reduction pipeline. IDL software which is discussed in detail in Meurer et al. (2007) was used to pick out potential emission lines in the spectra. The ACS G800L mode is sensitive to wavelengths 5700Å - 9800Å, and has a spectral resolution of R = 90. Emission lines from normal and active galaxies can be detected, and multiple emission-line regions can be detected in a single galaxy. It can also detect galaxies to high redshift; the sample described in Chapter 6, Table 6.1 includes a galaxy detected at $z = 5.13$. A number of cluster galaxies are detected which did not have previous spectroscopic detections. As population evolution in clusters is known to be different to that of the field (Dressler 1984; Ellingson 2003), it is useful to compare the properties of the cluster galaxies detected with the grsim with the equivalent properties of the field galaxies observed in a similar grism survey of the Hubble Deep Field North (HDF-N), reported in Meurer et al. (2007). These comparisons are presented in Chapter 6.

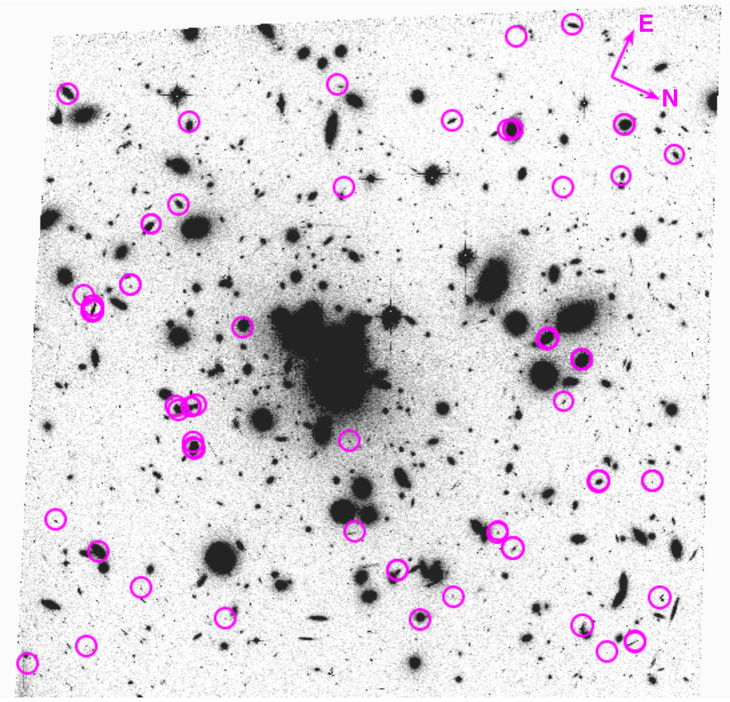

Figure 3.4: *The HST ACS field of view highlighting the galaxies detected in grism mode in 3 orbits. These objects are described in Chapter 6, Table 6.1.*

3.1.3 Magellan Observations at $z \sim 0.8$

In Chapter 6, low spectral resolution HST grism observations of a star-forming galaxy at $z = 0.7900$ (Duc et al. 2002) are presented (as objects #20002, #10640 & #10638, Fig. 6.8). Due to cluster lensing, this extended giant arc has a magnification of $\mu = 4 - 5$. Figure 3.5 shows a close-up of this galaxy from the colour image Figure 3.2 with the magnification contours from the Broadhurst et al. (2005) lensing model overlaid, suggesting a minimum magnification of a factor of 4. The blue colour of the galaxy in Figure 3.5 indicates star formation, and the multiple appearances of [O II] and [O III] in the grism spectra (Fig. 6.8, top panel) indicates that star formation may be occurring in at least 3 discrete locations within the galaxy. In order to investigate the galaxy in more detail, spectroscopic data was acquired at the one of the 6.5

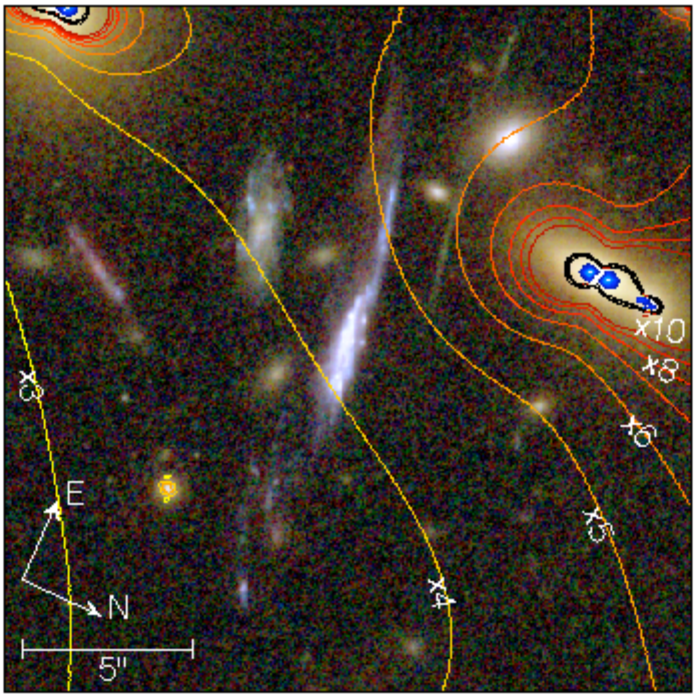

Figure 3.5: *A section of Figure 3.2, showing the* $z = 0.79$ *galaxy. Overlaid are the magnification contours resulting from the application of the lensing model of Broadhurst et al. (2005). The galaxy lies midway between contours, indicating a varying magnification across the galaxy, from less than a factor of 4 to greater than a factor of 5. Image taken from Frye, Meurer, Hurley et al 2010, in prep.*

metre Magellan telescopes at Las Campanas Observatory, Chile in March 2009 using the IMACS instrument (Dressler et al. 2006). IMACS (Inamori Magellan Areal Camera and Spectrograph) is a wide-field imager and multi-object spectrograph located on the Walter Baade telescope, one of the twin Magellan telescopes. The observations were made using a multi-slit mask, which was designed to prioritise this galaxy, but with several other galaxies targeted in the other slits. The other targets consisted of some interesting candidates from the HST grism survey (Chapter 6) and from other studies of A1689. One of these other slits was used to follow up an emission line source detected in the grism survey; the resulting spectrum is shown in Figure 6.5. The mask was designed using Ken Clardy's mask making software[3]. The IMACS instrument offers two cameras, the f/2 or short camera and the f/4 or long camera, which was the one used for these observations. The f/4 camera has a field of view of 236 square arcminutes (0.066 sq. deg.). The slit width chosen was $1''.0$, and the length was $12''.0$. The slit position angle is 100 degrees east of north and at this position angle, the slit covers the major axis of the arc, as shown in Figure 3.6. The mask was submitted to the staff at Las Campanas for milling, and the observations were kindly carried out by Dr. Sangeeta Malhotra and Dr. James Rhoads of Arizona State University (A.S.U.), as part of a strategic alliance between Dublin City University and A.S.U. The data taken on night 1 were taken using a 300 line mm^{-1} grating blazed at a central wavelength of 6650Å , but it was decided for nights 2 and 3 to change to a 600 line mm^{-1} grating, blazed at a central wavelength of 8410Å, and it is the resulting spectra which we will focus on in Chapter 7. The resolution from this grating was measured from the FWHM of the 6300Å skyline, which was found to be 7 pixels. The pixel scale is 0.387Å per pixel, so we get $R = \lambda/\Delta\lambda = 2326$, and we can resolve features greater than 2.71Å apart. As the difference between the observed wavelengths of the two elements of the [O II] $\lambda\lambda$3726, 3729Å doublet is greater than this, we are able to resolve these lines. Eight science frames were taken using the 600 line mm^{-1} grating, each with an 1800 second exposure time, giving a total of 4 hours integration time. The details of the reduction are outlined in Chapter 4, and the results are presented in Chapter 7.

---

[3] http://users.obs.carnegiescience.edu/clardy/imacs/maskmaking.html

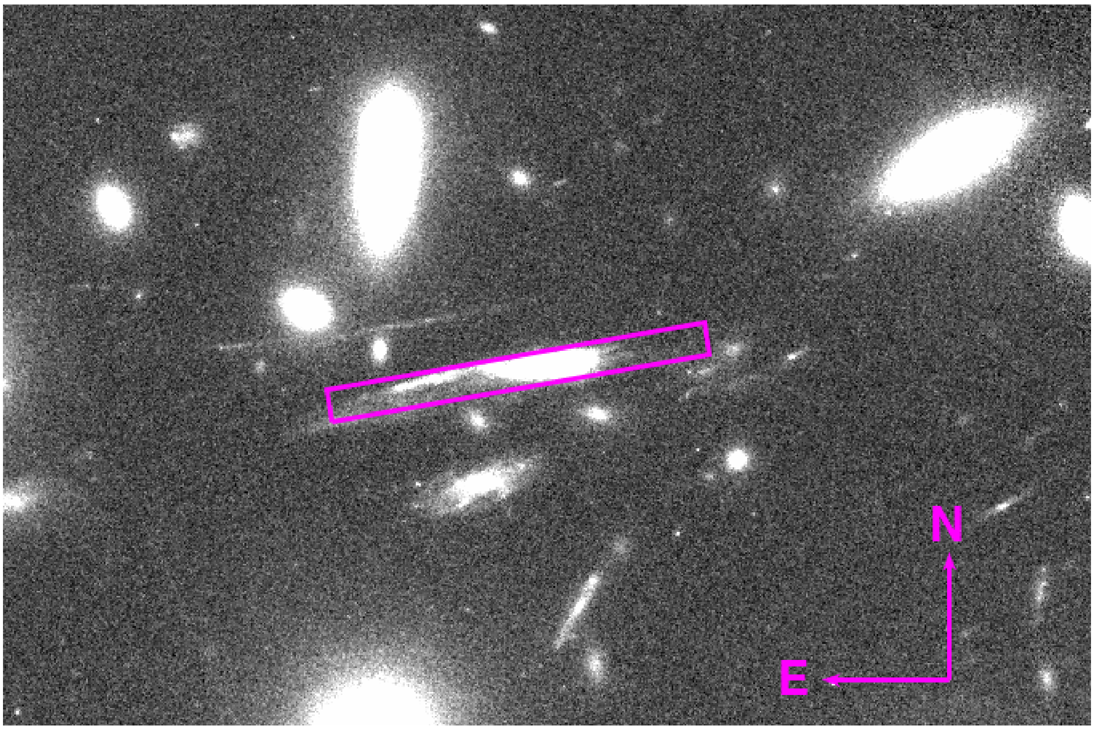

Figure 3.6: *Section of the F775W HST ACS image showing the* $z = 0.79$ *galaxy and the position of the slit used for the Magellan IMACS observations. The entire slit length is* $12\overset{\prime\prime}{.}0$. *When designing the mask, the slit was positioned carefully to align with the major axis of this galaxy, in order to try to detect the emission from the 3 regions found by the grism observations.*

3.1.4 Keck Observations at $z \sim 0.8$

Further observations of the $z = 0.79$ galaxy were made on 2010 May 11th and May 13th with the Keck telescope by Dr. Puragra Guhathakurta (U. C. Santa Cruz) and Dr. Evan Kirby (Caltech). The W.M. Keck observatory comprises two 10 metre telescopes located atop the Mauna Kea volcano in Hawaii, and are the largest of the current generation of ground-based telescopes. The 10 metre reflective surface is made up of 36 individual hexagonal segments. The instrument used was the DEep Imaging Multi-Object Spectrograph (DEIMOS, Faber et al. (2003)), and the observations were made through a $1.''0$ slit with the 1200 line mm^{-1} grating blazed at 10.16 degrees, with a central wavelength of 7800Å. A combination of 12 slitlets are placed together to create the $1.''0$ width longslit mask "Long1.0B". This longslit was placed at a position angle of 105 degrees east of north, as shown in Figure 3.7. Three 300 second exposures were taken during dusk twilight. The seeing was excellent, $0.''5$ FWHM on May 11th and $0.''6$ FWHM on May 13th. Resolution measured from the night skyline at 7571.75Å is $R = 5870$. Although not as deep as the Magellan observations, the combination of good seeing and high spectral resolution of the 1200 line mm^{-1} grating allows us to probe the spatial distribution of the gas in the galaxy and examine the variation of the spectrum across its larger spatial extent. The strong emission lines are obvious in the two-dimensional image and are strongly slanted, indicating gas motion within the galaxy, and/or emission from distinct regions, as was observed in the grism spectra. The results from these observations are presented in Chapter 7.

3.1.5 Einstein Rings: VLT Observations at $z \sim 2.4$ and $z \sim 3.6$

As discussed in Section 2.1, the image of a background object can be completely tangentially stretched into a ring if a serendipitous alignment exists between the background source, intervening lensing object and the observer. If either the mass distribution of the intervening deflector is not perfectly symmetrical, or if the source, lens and observer are not perfectly aligned, a partial Einstein ring will be observed. In 2009, the rest-frame ultraviolet spectra of two such partial Einstein rings were observed with the VLT, and are presented here in Chapter 8. These are both blue, spatially resolved and extremely bright (total magnitude of $\mathrm{i}_{775} \sim 20$). The first of these is a galaxy at $z = 2.38$ imaged as

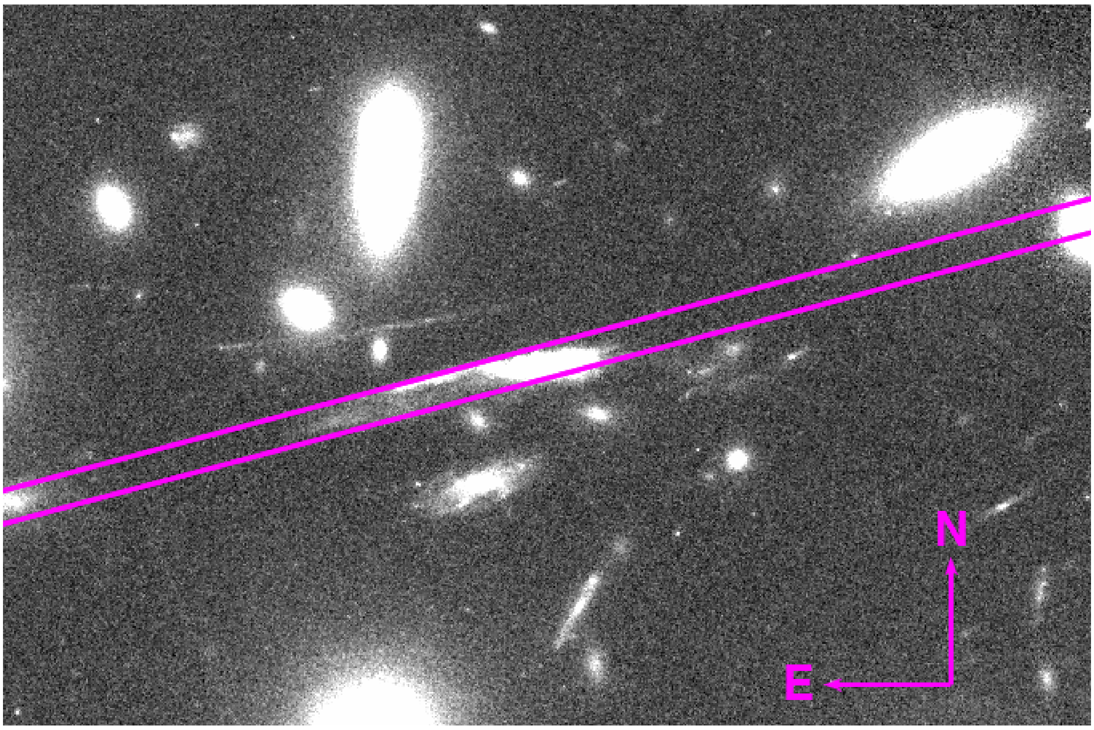

Figure 3.7: *Section of the F775W HST ACS image showing the position of the slit used for the Keck DEIMOS observations of the* $z = 0.79$ *galaxy. The entire slit length is* $82''\!.0$.

an almost-complete ring, with a diameter of $\sim 10''$. It is known as the "Cosmic Horseshoe", and is lensed by a massive luminous red galaxy at $z = 0.444$ (Belokurov et al. 2007). The second galaxy, at $z = 3.595$, is known as "ER 0047 -2808" (Warren et al. 1996, 1998), and is lensed by an intervening galaxy at $z = 0.485$.

The Cosmic Horseshoe at z $\sim$ 2.4

The Cosmic Horseshoe was observed for 2.33 hours in April and May 2009 with the FORS2 instrument on the VLT (see Section 3.1.1), comprising six 1400 second exposures. The observations were made in longslit (LSS) mode. The FORS2 longslits have a common slit length of $6'\!.8$, and the slit used for these observations had a width of $1''\!.0$. The grism used, "GRIS_600B+22" has 600 lines mm^{-1} and is blazed at a central wavelength of 4650Å, with a wavelength range of 3300Å - 6210Å. The slit was placed at a position angle of 6.2 degrees east of north, ensuring slit coverage of a region encompassing the two brightest spots in the Einstein ring, those labelled "A" and "D" in Belokurov et al. (2007). Figure 3.8 shows an SDSS r-band image of the Einstein ring with the slit overlaid. The telescope was dithered between exposures to reduce chip artifacts. The results of these observations are presented in Chapter 8, with the spectrum shown in Figure 8.5. The observations made of the Cosmic Horseshoe with the Echellette Spectrograph and Imager (ESI) on the Keck II telescope, presented in Quider et al. (2009) were made with a similar position angle, 10.8 degrees east of north, and also cover these two bright knots.

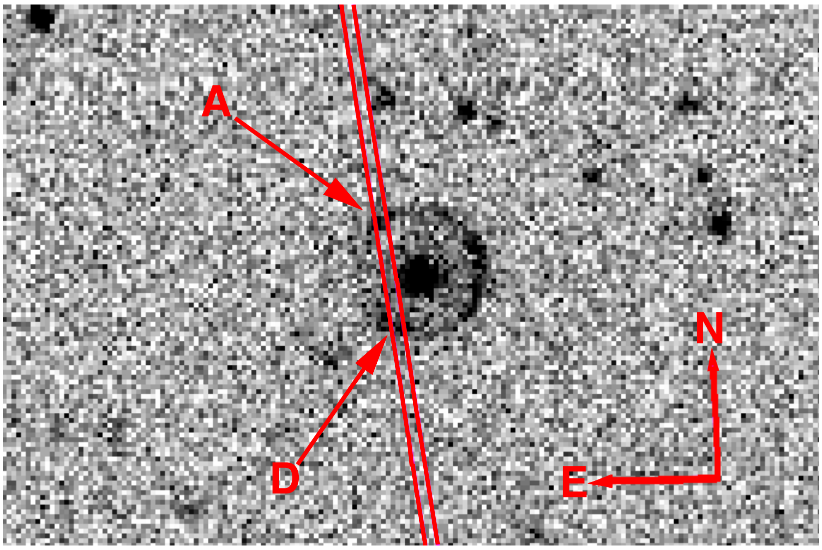

Figure 3.8: *Section of an SDSS r-band image showing the position of the 1.″0 width longslit used for the VLT FORS2 observations of the Cosmic Horseshoe. The slit was carefully aligned so as to cover two of the brightest knots in the Einstein ring, while minimizing contribution from the central lensing galaxy at* $z = 0.444$.

The Einstein Ring ER 0047 -2808 at z ∼ 3.6

The Einstein Ring ER 0047 -2808 was observed for 5.445 hours between May and September 2009, with fourteen 1400 second exposures. The FORS2 instrument on the VLT was also used in longslit mode for these observations. A 600 line mm^{-1} grating "Grism 600RI+19" and filter "GG435+81" were used. The slit was again the 1.″0 width longslit, with dithering again applied between exposures. Its position angle was 11.4 degrees east of north, which unfortunately meant that a large amount of contaminating light from the lensing galaxy came through the slit as well as the light from the lensed galaxy. The contamination makes it difficult to resolve features of the lensed galaxy in the spectrum as can be seen in Chapter 8, Figure 8.9.

4

Reduction of Multislit and Longslit Spectroscopic Data

4.1 Initial Data Reduction

The data reduction and analysis of all the spectroscopic data from the VLT, Magellan and Keck telescopes described in Chapter 3 was carried out entirely using a custom-built code written in the Interactive Data Language (IDL), the basis of which was originally written for use with a ground-based arclet redshift survey (Frye et al. 2002), but with modifications introduced specifically for this project. IDL is a programming language which is particularly suitable for use in astronomical data analysis. It is less opaque than the dedicated astronomical software IRAF (Image Reduction and Analysis Facility) as the user must write their own programs to manipulate the data, thus giving more flexibility and control. IDL also has the added benefit of having an Astronomy User Library hosted by NASA Goddard Space Flight Center, which contains astronomy-specific procedures. These include procedures for working with data in the FITS (Flexible Image Transport System) format, which is a standardized data format widely used in astronomy. The FITS format can be used to store ASCII or binary tabular data, as well as images and spectra. The source data coming from the VLT, Magellan and Keck observations are all initally stored in the FITS format. Spectroscopic data is output from the CCD (charge-coupled device) detector in two-dimensional (2D) arrays, with the two axes described henceforth as the dispersion axis and the spatial axis. The dispersion direction of the spectrum represents the light from the observed object which has been dispersed through the slit out into wavelength intervals. The spatial direction of the spectrum represents the physical size of the emitting part of the object seen through the slit. In the observations described here, the galaxy traces out a spectrum completely along the dispersion direction comprising a few rows of the spatial direction. In this chapter, we will use the index x to refer to dispersion direction, i.e. the columns in the array, and the index y to refer to the spatial direction or rows. The number of spatial rows across which to extract the spectrum is generally estimated from the size of a bright emission line in the 2D spectrum. Figure 4.1 is a coadded image[1] of VLT exposures of the $z = 4.9$ galaxy (Section 3.1.1), showing an example of such an emission line. In reducing astronomical data, there are some standard pre-processing steps which must be performed in order to extract information from the raw frames. All CCDs have an artificially induced electronic offset, or bias level, which must be removed from each image if the data values are to be accurate. An average of many exposures of zero seconds each with the shutter closed is used as a master bias frame, which contains an image of only the bias level. This master bias frame is subtracted from every other image. If bias frames are not available, the bias level may be calculated from the overscan region, which is a region comprising a number of rows or columns not exposed to the light source. These appear as dark rows or columns at one or more edges of the image. Overscan regions, if present must be trimmed off before reduction. Another issue inherent to the CCD electronics is the gain factor, which is the conversion between the number of electrons recorded by the CCD and the number of counts in ADU (Analog-Digital-Units) in the CCD image. These

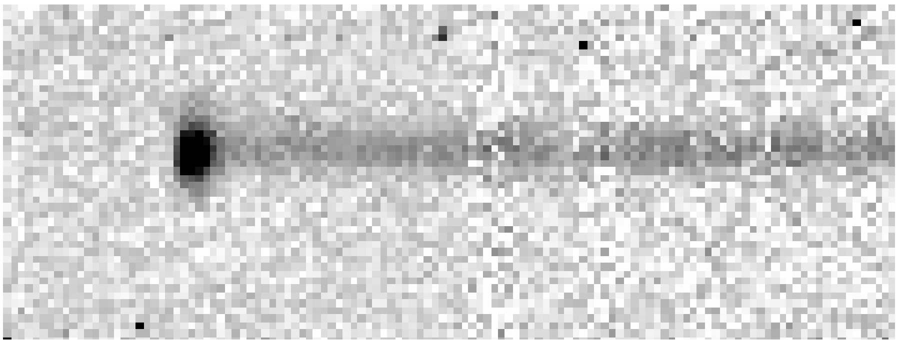

Figure 4.1: *A section of a 2D coadded image of all VLT FORS2 exposures of the* $z = 4.9$ *galaxy showing Lyman-*α *emission and continuum emission longward of the line. Dithered images have been shifted to line up.*

---

[1] For the purposes of this image, co-addition has been carried out using the IRAF task *"imcombine"* with cosmic-ray rejection, however, IRAF tasks are not used in the data reduction process, and cosmic ray rejection is carried out in this data reduction pipeline at the stage of coaddition of 1D spectra.

ADU counts are proportional to the electron charge created by the incident photons on the detector. To correct for this offset, each image is multiplied by the detector gain, in units of e^{-1}/ADU. The gain factor varies from CCD to CCD, and so if the output image is made up of individual “chips”, each with a different CCD detector (as is the case with the Magellan IMACS observations) care must be taken to multiply by the correct gain in each case.

The final standard step is to apply flatfield correction, which aims to remove artifacts caused by variations in pixel-to-pixel sensitivity across the detector, to correct for vignetting of the optical system, and also to correct for dust on the filters or optical windows. In order to correct for this, an image of the pixel responses known as a flatfield is taken by exposing the CCD to a uniform light source. These pixel responses can change with time, and in order to account for this factor, flatfield exposures are taken on the same night as the target is observed. The flatfield images are taken at high signal to noise, and are generally either short exposures taken at dawn or dusk, called twilight flats, or exposures of the illuminated closed dome of the telescope, called dome flats. The flatfields for each individual filter are combined and normalized to one, and this flatfield image is divided into raw images taken with the same filter. This straightforward method is appropriate for imaging of targets, however for spectroscopic data the pixel response is wavelength dependent, and this must be taken into account in flatfielding. An object flatfield may be used for this step, which is a short exposure of a halogen lamp through the same slit and grating used for the target observations, and ideally taken in between every few target exposures. A number of such object flats are combined in order to improve the signal to noise, using a sigma-clipping procedure to reject cosmic rays. If the imprint of the blackbody shape of the light source illuminating the slit is left on the image, this can be propagated onto the data. In order to remove this effect, the combined object flat is divided by a smoothed version of itself. The object flat is also normalized to the median value. Finally, the normalized object flat is divided into the science target frames.

The next step in the data reduction process is the subtraction of the sky background. This is a vitally important step in the data reduction process, in particular for the VLT observations of the galaxy at $z = 4.9$, as the object being observed is extremely faint and distant, and even its brightest features such as Lyα emission do not stand out from the background sky by more than a few counts. For example, Figure 4.1 shows 42 exposures coadded after background subtraction. As a comparison, Figure 4.2 shows one individual exposure before background subtraction, with prominent skylines and a faint emission line. These objects are extremely background-limited - the sky counts are much greater than the object counts. The signal-to-noise equation is given by

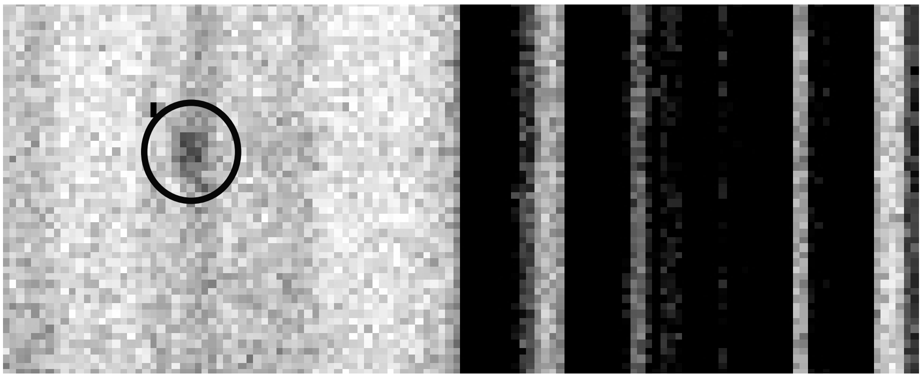

Figure 4.2: *A section of a single VLT FORS2 exposure of the* $z = 4.9$ *galaxy. Lyman-*α *emission is barely visible (circled), while continuum emission longward of the line is not apparent. This is an exposure prior to background subtraction, and the dark line longward of Ly-*α *are skylines.*

$$\frac{S}{N} = \frac{R_* \times t}{\sqrt{(R_* \times t) + n_{pix}[(R_{sky} \times t) + (D \times t) + (RN^2)]}}$$

where R_* is the count rate in electrons per second from the source, R_{sky} is the count rate from the sky background in electrons per second per pixel, t is the exposure time, D is the dark current in electrons per pixel per second, and RN^2 is the total number of electrons per pixel resulting from the read noise. Assuming a negligible dark current for a cooled CCD and minimal contribution to noise from the readout time, giving $R_{sky} \gg RD^2$ and $R_{sky} \gg D$ and assuming $R_{sky} \gg R_*$ for a background limited object, we can rewrite this equation as

$$\frac{S}{N} = \frac{R_* \times t}{\sqrt{n_{pix} \times R_{sky} \times t}} = \frac{R_* \times \sqrt{t}}{\sqrt{n_{pix} \times R_{sky}}}$$

The noise term is dominated by the sky and the signal to noise is inversely proportional to the square root of the noise. The S/N is proportional to the square root of the integration time, so to double the S/N, the exposure time must be increased by four. It is essential to correctly determine the sky background and subtract it from each image, leaving the intrinsic galaxy signal. Using too few background pixels can increase the noise. Background subtraction is carried out individually for each slit on a multislit mask, finding the optimal level of correction. As well as the overall sky background present everywhere, in spectroscopic data the spectrum of the sky will show strong lines known as skylines at certain wavelengths, which fill the entire spatial extent of the slit. The strength of these lines must be estimated and removed as effectively as possible. Most of the sky lines observed in a spectrum in the optical/near-infrared (NIR) regimes come from rotation-vibration molecular bands of OH. O_2 lines are also observed, as well as the well-known atomic night-sky lines of [OI] at $\lambda\lambda$5577, 6300 & 6363 Å (Osterbrock et al. 1996). The code for background subtraction calculates the average sky value at each pixel x, which is calculated from the median of the y pixels in the slit, after masking out the object and any deviant pixels-bad pixels or cosmic rays. In order to remove the skylines, we estimate the average sky value in a blank patch of sky, and then find the columns in which the average sky value is significantly higher than this. Skylines can appear curved or tilted on the images with respect to the CCD grid, and so the line is fit at each position x by a polynomial. Finally, this background array is subtracted from the flatfielded, bias and gain corrected science frame. At this point we have a 2D image which is ready to have the wavelength-dependent spectrum extracted.

Extracting a 1D spectrum involves choosing an extraction range in the spatial direction. For background limited data, we choose the extraction range to be the number of rows covered by a bright emission line. At each x position, the values of the pixels in the extraction rows are summed, resulting in a 1D array of $0 - n_x$ values, where n_x is the number of dispersion pixels x.

$$f_x = \sum_{y_1}^{y_2} (D_{x,y} - S_{x,y}) \tag{4.1}$$

$D_{x,y}$ is the two dimensional object frame prior to background subtraction and $S_{x,y}$ is the two dimensional array of background sky values. The y-pixels chosen as the lower and upper limits of the extraction range are denoted as y_1 and y_2 respectively. An important aspect of the extraction procedure is the inclusion of a method to follow the curvature of the slit. Instrumental flexure can curve the edges of the spectrum box, leaving the signal with a roughly quadratic shape with respect to the fixed CCD grid. This can mean that a spectrum can be shifted in the spatial direction, meaning that the extraction range specified at the centre of the detector may miss part of the spectrum at the outer edges. This situation is depicted in Figure 4.3, which shows the red side of a chip containing the spectrum of a standard star taken with VLT FORS2. The two dark lines in each panel show the continuum extraction range. The top panel shows the case in which the spatial curvature has not been accounted for, and the extraction range shown is that chosen to be a suitable range in the centre of the chip. Here, at the red side of the chip, the pronounced curvature means a large portion of the starlight is missed. The bottom panel shows the case in which a polynomial fit has been made to the source, and this curvature followed. For a bright source such as a standard star, tracing the curvature by following the continuum is acceptable. However, in the case of background limited data such as the VLT observations of the $z = 4.9$ galaxy, there is no bright

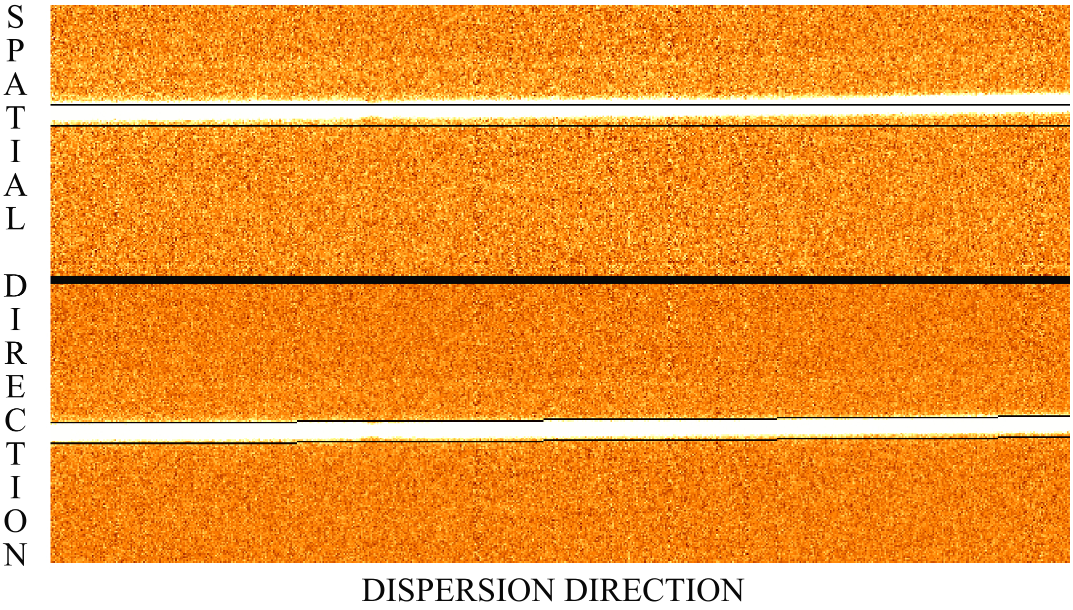

Figure 4.3: *Example of instrumental flexure in a VLT FORS2 spectrum of a standard star. These images show the longest wavelength side of the detector. The dark lines in each panel indicate the extraction range. The top panel shows the extraction range specified at the centre of the chip with no correction for curvature - this clearly causes a loss of signal at the edge of the chip. The bottom panel shows the correction for curvature. In this case, the correction has been carried out by tracing the bright continuum across the slit and making a quadratic fit to the shape. In the case of background-limited data, the edge of the spectrum box is found on a flatfield image and the fit is made to the shape of the edge, which will also be affected by this curvature. The fit is then translated onto the extraction range.*

continuum to trace along to find the shape of the curvature. In this case, we modify our method to take the flatfield created using the same multislit mask, and trace the shape of the intervals between the slit boxes to determine the curvature. We find a variation of 1-2 pixels in each case from centre to edge. The fit to the shape of the box is then translated onto the extraction range. As we are dealing with a background-limited dataset, giving equal weight to every pixel in the extraction range may introduce noise into the spectrum as pixels further from the central position may only carry a small fraction of object signal. For the $z = 4.9$ dataset, an optimal extraction algorithm was developed based on Horne (1986), which is described in Section 4.2. Once a 1D spectrum has been extracted, wavelength calibration is then carried out, using observations of arc lamps as a wavelength reference. The wavelengths of the lines in the lamp spectrum are identified from the reference line lists provided by the telescope. The code calculates a fit based on these emission lines, and applies it to the extracted spectrum, giving a spectrum in units of photon counts per wavelength step. If absolute measurements of flux values from the observed object are desired, a final step must be carried out to convert the photon counts to flux units. This step requires additional observations of a spectrophotometric standard star. This is a star which has been calibrated so that its absolute flux across a range of wavelengths is well determined. A number of catalogues of spectrophotometric standard stars exist, such as those of Hamuy et al. (1994) and Oke (1990). The standard star is observed with the same telescope setup as the science frame observations, and a spectrum extracted and wavelength calibrated in the manner described above. One can then compare the observed counts from the spectrum to the documented flux of the standard star to compute the relative scaling from counts to flux units, and use this solution to convert the observations from counts to flux. An example of the steps involved are shown in Section 4.4, Figures 4.9 and 4.10 in describing the fluxing of Keck observations of the $z = 0.79$ galaxy.

Energetic particles known as cosmic rays are continually passing through the Earth's atmosphere and impinging on the surface. During any observation, cosmic ray particles will arrive at the detector, and due to their energetic nature, leave a large charge on the CCD pixel or pixels that they strike. They generally only affect a few pixels at a time. These false positives must be removed from the final spectrum. After extracting a 1D spectrum from each exposure, these must be coadded to improve S/N. The coaddition code corrects for cosmic rays by flagging deviant pixels and ignoring these. The code is also able to distinguish between cosmic rays and emission lines, as emission lines will fall on the same place in each spectrum, while cosmic ray contamination is random. Removing the contribution from a single pixel when coadding a large number of spectra will not significantly affect the overall resulting spectrum.

4.2 Optimal Extraction of the 1D Spectrum for $z = 4.9$ Galaxy

In determining an extraction range, spectrophotometric accuracy can be improved by selecting a wide range of pixels. However, this approach can introduce noise as pixels containing only a small fraction of the signal are included in the same manner as the central pixels. Optimal extraction is a method of applying weights to the extraction range in order to reduce this noise while retaining photometric accuracy. A weighting profile P_y is defined which assigns lower importance to the spatial pixels further from the peak of the object signal. In spectroscopic data reductions, typically numerous versions of the spatial profile are created in order to follow the object shift in spatial position but in this background-limited data, in which the signal is not well sampled across the whole wavelength range and which has sudden continuum breaks, this approach could introduce noise into the data and render optimal extraction unuseable. To cope with the problem of tracking a moving spatial profile across the dispersion range, a single weighting profile is created which translates spatially with the flexure-induced curvature in the dispersion direction. This profile is constructed to run from y_1 to y_2 by summing up the background-subtracted pixels across a selected x range. As the profile must not be affected by any curvature in the dispersion direction, a range in x is selected running from x_1 to x_2 across which the curvature does not change. In order to ensure that the profile is not affected by any cosmic ray hits or bad pixel effects which would artificially skew its shape, a mask M of flagged pixels is used to reject these pixels. Following an initial extraction with natural weights, a running median boxcar is used as a baseline against which all pixels are compared. A threshold is set at a value much higher than the counts for a typical emission line, and pixels exceeding this threshold are flagged. This mask is a 1D array in x, with all good pixels having a value of 1 and all bad pixels having a value of 0. This method removes the entire column x if any one pixel in any row from $y1 - y2$ in the column is rejected, but as $\sim$ 1000 columns are used in the construction of the profile, and as flagged pixels are comparatively few, rejection of the single column does not make a noticeable difference to the resultant profile. The dashed lines in Figure 4.4 show the spatial profiles prior to this cosmic ray rejection. The profile is then normalized to one and positivity is enforced. The variance image $V_{x,y}$ is created (Equation 4.5), based on the initial spectrum f_x, profile P_y and sky array $\mathrm{S}_{x,y}$. $\sqrt{V_0}$ is the RMS readout noise, which for the $z = 4.9$ VLT data is 5.41e$^-$, and Q is the gain, in this case 0.52e$^-$/ADU. Equation (8) of Horne (1986) is used to calculate the optimal spectrum f_x^{opt}, given in Equation 4.6. Equation 4.5 is then iterated, this time using f_x^{opt} to improve the estimate of the variance, and this improved variance image is used in an iteration of Equation 4.6. The process of extraction is laid out in mathematical form in Equations 4.2 - 4.6.

$$f_x = \sum_{y_1}^{y_2} (D_{x,y} - S_{x,y}) \tag{4.2}$$

$$P_y = \frac{\sum_{x_1}^{x_2} M_x \times (D_{x,y} - S_{x,y})}{\sum_{x_1}^{x_2} M_x} \tag{4.3}$$

$$\text{Normalize profile: } P_y = \frac{P_y}{\sum_{y_1}^{y_2} P_y} \tag{4.4}$$

$$V_{x,y} = V_0 + |f_x P_y + S_{x,y}|/Q \tag{4.5}$$

$$f_x^{opt} = \frac{\sum_{y_1}^{y_2} P_y (D_{x,y} - S_{x,y})/V_{x,y}}{P_y^2/V_{x,y}} \tag{4.6}$$

For severely background limited data, the S/N can be increased by creating an average spatial profile for all exposures of a given dither pointing, as seen in Figure 4.4, which shows the individual and averaged profiles for the central pointing of the VLT run. In comparing regions of the spectrum free of strong spectral features in the optimally extracted spectrum compared to the naturally-weighted spectrum, an small improvement of the root-mean-square noise level in the continuum of $\sim$ 5% is measured in the blue, while an im-

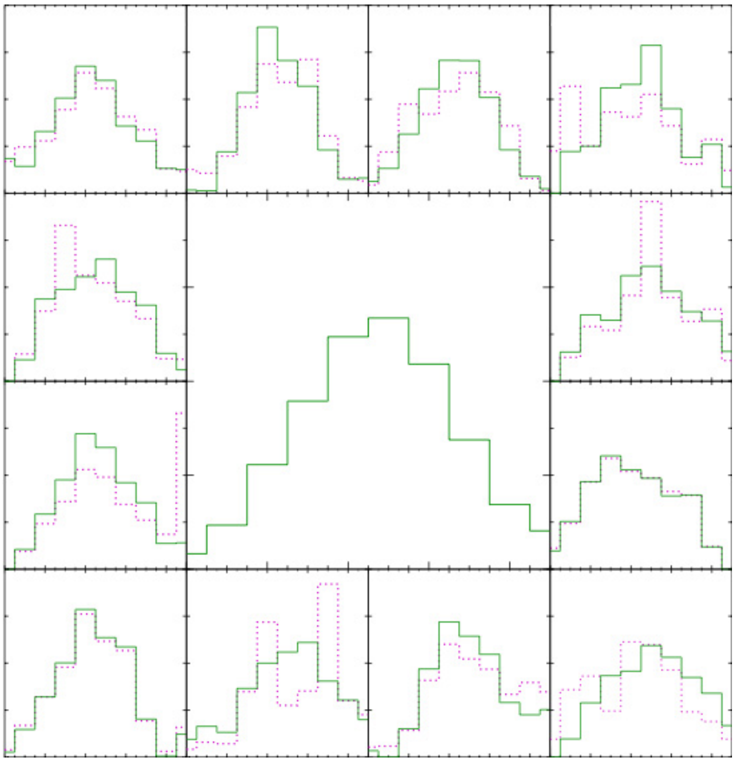

Figure 4.4: *The central panel shows the overall combined spatial weighting profile, constructed from the spatial profiles of 15 individual VLT exposures taken at the central dither position, 12 of which are shown in the smaller outside panels. The dotted lines indicates the shape of the profiles prior to cosmic ray clipping. All profiles are normalized to one.*

provement of $\sim$ 7.5% is seen in the red. This improvement corresponds to an increase in exposure time of $\sim$ 10% and $\sim$ 16% respectively. An example of the improvement gained by optimal extraction in the red is shown in Figure 4.5. The optimally extracted spectrum is shown in thicker black, while the unweighted spectrum is shown in blue. The fluxing of the $z = 4.9$ galaxy data was carried out using observations of the standard star LTT9239 which were taken concurrently with the galaxy spectra. The results of this reduction process for the $z = 4.9$ galaxy are presented in Chapter 5.

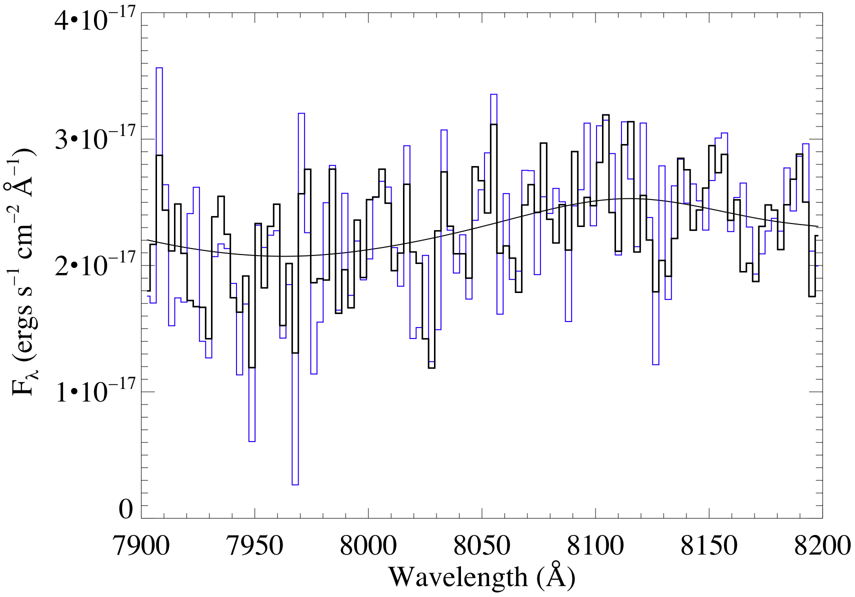

Figure 4.5: *The optimally extracted spectrum (thicker black) and the non-weighted spectrum (blue) shown for a portion of the wavelength coverage towards the red end of the chip. The improvement in S/N in the optimally extracted spectrum compared to the non-weighted spectrum is $\sim$ 7.5% here, corresponding to an increase in exposure time of $\sim$ 16%.*

4.3 Magellan IMACS Data Reduction for $z = 0.79$ Galaxy

The Magellan observations of the galaxy at $z = 0.79$ were reduced in the manner described in Section 4.1. One difference between the VLT FORS2 and the Magellan IMACS systems is the layout of the CCD used on IMACS. The data is output to 8 individual CCD chips (see Fig. 4.6), each of which has a slightly different gain and readout noise, this was accounted for in the early step of correcting for the gain. There is also a “chip gap” at the intersections

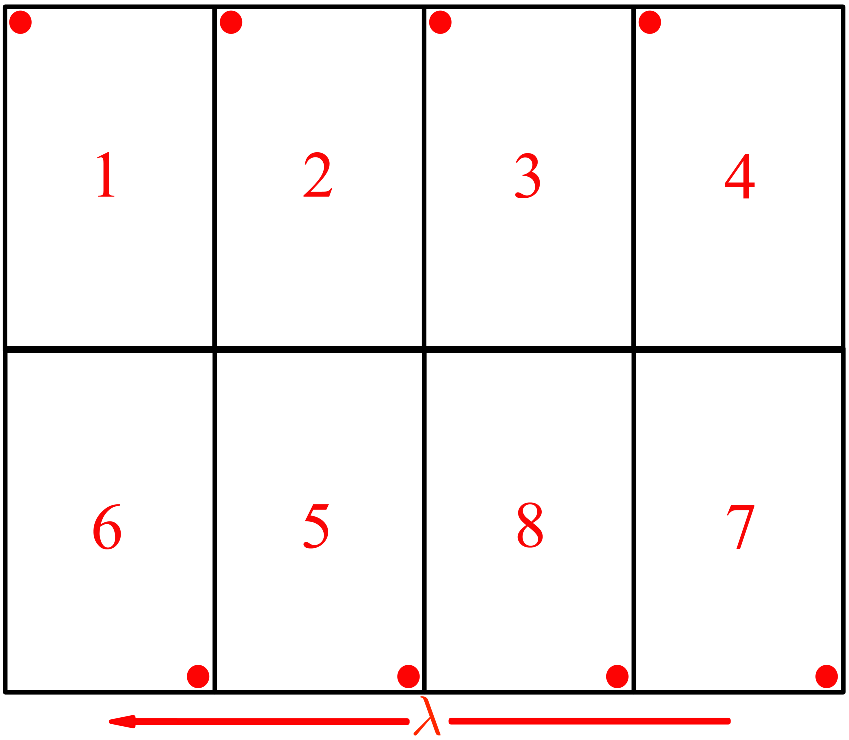

Figure 4.6: *Layout of the chips on the CCD. The red side comprises chips 1 and 6, in which the sensitivity of the CCD is significantly poorer than the blue side. The circle in the corner of each chip represents the position of 0,0 on each output fits file.*

of the CCDs, which results in some small gaps in the final 1D spectra. For the $z = 0.79$ galaxy, the expected position of the spectral line of the H9 hydrogen Balmer transition falls on a chip gap and so the strength of the line cannot be measured. In the 2D combined frames (example shown in Fig. 4.7), it was clear that a CCD defect lies a few pixels away from the continuum for this galaxy, and subsequently, these pixels had to be masked out during the background subtraction process.

The Magellan data have not been fluxed, as the adequate observations of a standard star in the same setup as the galaxy observations were not made. As a step towards correcting for the sensitivity of the detector, we divide the sensitivity curve into the data. The shape of this curve is shown in Figure 4.8. The results are presented in Chapter 7. While absolute line fluxes cannot be reported, diagnostics based on equivalent widths and relative line ratios are still valid for this data set.

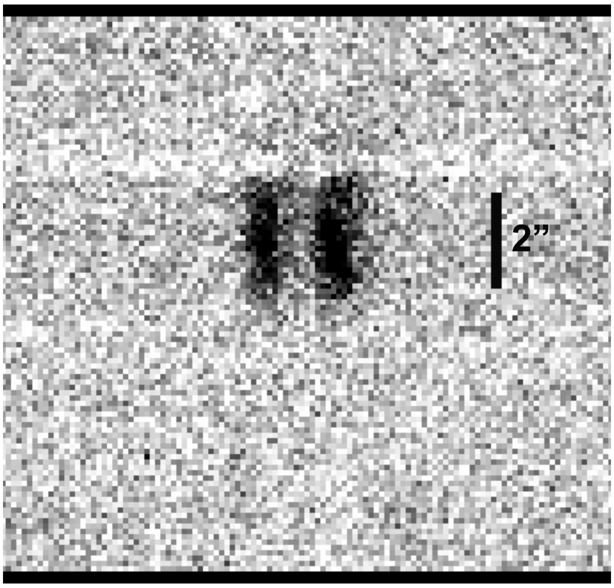

Figure 4.7: *A section of the combined, background-subtracted 2D spectrum, showing the prominent [O II] emission, and the detector defect (horizontal lighter-coloured stripe) directly above the continuum.*

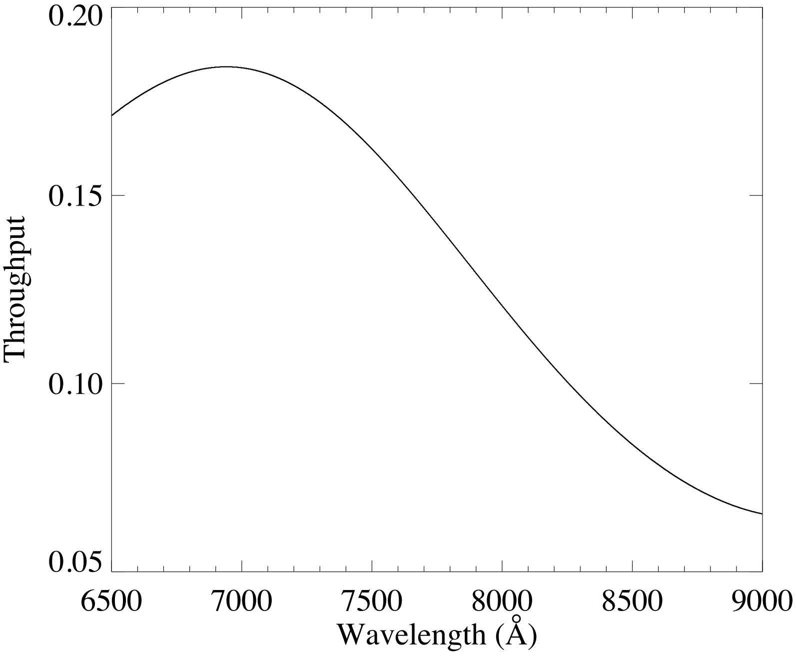

Figure 4.8: *The efficiency curve for IMACS f/4 Camera, 600 l/mm grating with 13 degree blaze angle, the setup which was used for these observations.*

4.4 Keck Data Reduction for $z = 0.79$ Galaxy

The three 300 second exposures made with Keck DEIMOS using the 1200 line mm^{-1} grating were reduced using the DEEP2 DEIMOS data pipeline outlined in Davis et al. (2003) and Wirth et al. (2004) [2]. This pipeline was developed for use with the DEEP2 project, which also used the 1200 line mm^{-1} grating. The masks for DEEP2 consist of a number of slitlets, but the pipeline is also capable of handling long slit data. Part of the pipeline, IDL procedure "extract1d.pro" was used as a stand-alone to extract the 1D spectrum over the entire chosen extraction range of 35 pixels, a spatial extent of $4\farcs148$. Multiple spectra were also extracted over 5-pixel wide extraction ranges, to give 7 unique spectra along the spatial direction of the slit. This allows examination of the spatial variation of the emission lines along the long axis of the galaxy. Figure 7.3 shows a stack plot of these 7 spectra in the region of the Hβ emission line, showing the variation across the spatial direction. The DEIMOS detector is made up of two individual CCD chips. The data was fluxed using observations of spectral standard HD 93521 (Oke 1990), and was carried out separately for the blue and red halves of the chip. Figures 4.9 and 4.10 show the observed spectrum of HD 93521 (smoothed by a factor of 59 to remove strong spectral features, and with the A and B atmospheric bands patched over), the standard spectrum from the Oke (1990) catalogue, and the resulting smoothed fluxing function which was divided into the data to give final units of ergs s^{-1}cm^{2}Å^{-1}. Results of this reduction process are also presented in Chapter 7

---

[2] The analysis pipeline used to reduce the DEIMOS data was developed at UC Berkeley with support from NSF grant AST-0071048.

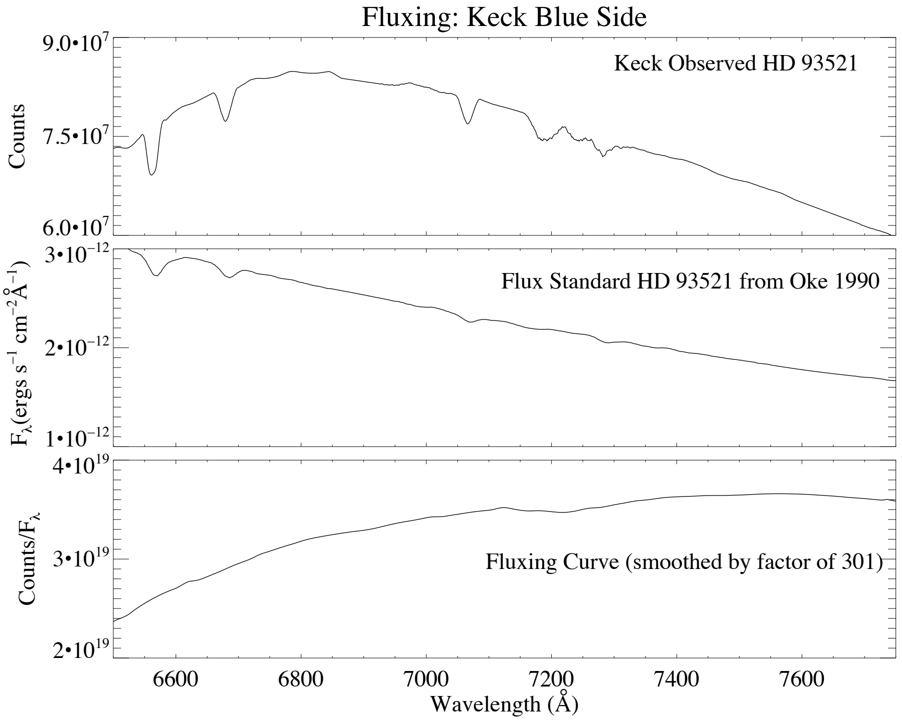

Figure 4.9: *Fluxing data for blue side: top panel: observed spectrum of HD 93521; middle panel: HD 93521 spectrum from Oke (1990); bottom panel: resulting fluxing function which is divided into the galaxy spectrum to convert from counts to ergs* $s^{-1} cm^2 Å^{-1}$.

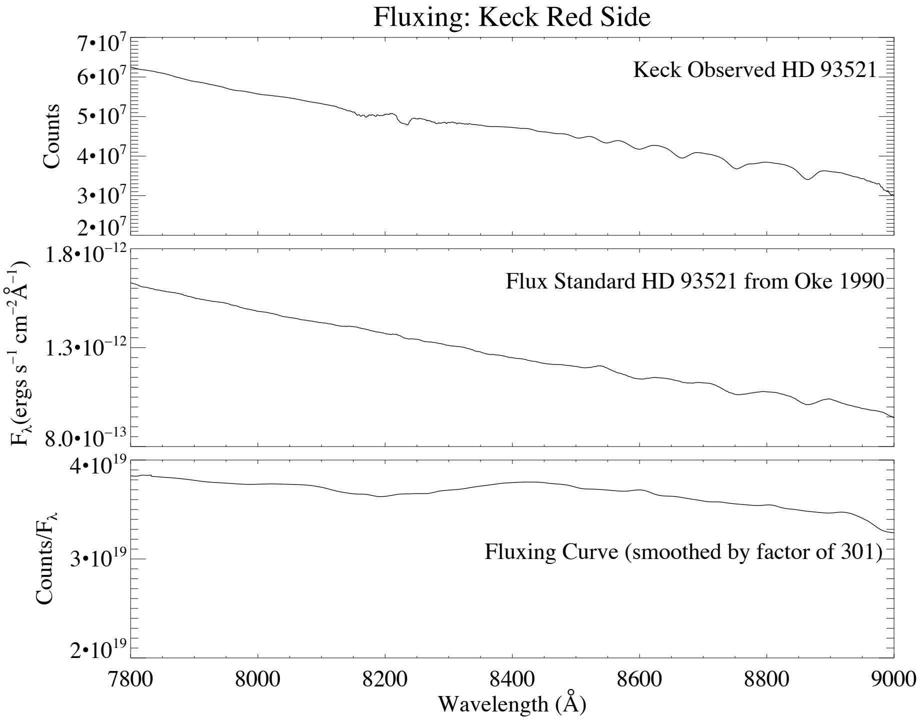

Figure 4.10: *As Figure 4.9, but for the red side of the chip.*

4.5 VLT Longslit Data Reduction for $z = 2.4$ and $z = 3.6$ Einstein Ring Galaxies

The observations of the two Einstein Ring galaxies described in Section 3.1.5 were made in longslit mode. The only variation from the data reduction method outlined above is that unlike a multislit mask, slit edges cannot be used to trace the curvature of the slit in the spatial direction. Luckily, these spectra are adequately bright to trace the curvature along the galaxy continua. For the Einstein Ring ER 0047 -2808 the continuum is visible along the complete chip. For the Cosmic Horseshoe, in the individual exposures, the trace is weak at the blue end of the chip and only becomes strong redward of Lyα emission. As there is no point of reference here, the curvature is undefined for ~600 pixels on the blue side of the chip. In order to account for this, a coadded image of all exposures was used to trace the shape of the continuum, as the faint signal below Lyα is visible in this image. The curvature calculated in this way was then used as the trace for the extraction of the spectrum from each individual exposure. The slit positioning for the Cosmic Horseshoe observations (Figure 3.8) intersects the lensed galaxy at two points, leaving two spectra on the 2D image. These are extracted separately in the normal manner and coadded to give the resulting spectrum presented in Chapter 8. ER 0047 -2808 was fluxed using the standard star LTT4816, and the Cosmic Horseshoe was fluxed using the standard star LTT7379, both from the catalog of Hamuy et al. (1994), with the observations of these standard stars taken contemporaneously with the science frames.

5

A Gravitationally Lensed Galaxy at $z = 4.9$: Results

This chapter deals with the analysis of spectroscopic data of the $z \sim 4.9$ galaxy (henceforth A1689-7.1 as designated in Broadhurst et al. (2005)), which I extracted from the 14 hours of VLT FORS2 observations described in Chapters 3. The galaxy was initially detected by Frye et al. (2002) as part of a ground-based redshift survey. To optimally extract the spectrum I expanded upon the reduction code of Frye et al. (2007), introducing custom-written routines to cope with the large dataset and to perform optimal extraction adapted to this specific set of observations as described in Chapter 4. The resulting spectrum (shown in Figure 5.1) explores stellar and interstellar features within the galaxy, as well as the environment of the galaxy. Section 5.2 describes the measurements I made of the Gunn-Peterson effective optical depth toward the galaxy, which allows us to infer the presence of an excess of neutral hydrogen (H I) in the vicinity of the galaxy. Section 5.3 outlines the spectral energy distribution (SED) modelling which I carried out using the stellar population synthesis code of Bruzual & Charlot (Bruzual and Charlot 2003) and the photometric observations of the galaxy. While the library of evolutionary stellar population synthesis models are from Bruzual and Charlot (2003), I added complementary programs to find the best fitting parameters of the three variables according to a prescription originally applied to X-ray data (Cash 1976). Some of the results presented in this chapter have been published by Frye et al. (2008).

5.1 Spectroscopy Results

The spectra of galaxies with ongoing star formation display strong emission lines which are generated when ionising radiation from newly formed stars interacts with the surrounding gas. Both collisionally excited lines and lines due to recombinations are formed following the absorption of ultraviolet (UV) photons emitted by the hot young stars. The transition of hydrogen to the $n = 1$ ground state results in the emission of photons which are visible in the ultraviolet part of the spectrum. In particular, the transition from the $n = 2$ to $n = 1$ atomic levels results in the emission of a photon with a wavelength of 1216Å which is known as the Lyman-α (henceforth Lyα) line. Galaxies at redshifts of $z \sim 5$ have their rest-frame UV spectrum shifted into the observed frame optical wavebands, which means that the dominant emission line observed in this passband is the Lyα recombination line. The spectrum of A1689-7.1 is presented in Figure 5.1. Dr. Brenda Frye and collaborators have recently used the VLT SINFONI (Spectrograph for INtegral Field Observations in the Near Infrared) instrument to make further observations of this object at infrared wavelengths, and have kindly provided the systemic redshift measured from the [O II]$\lambda\lambda$ 3726.1,3728.8 emission lines, which is $z = 4.8722 \pm 0.0012$. We take this to be the best measurement of the systemic redshift, as this represents the emission from the nebular gas. The most prominent feature in the spectrum shown in Figure 5.1 is indeed strong Lyα emission. The Lyα line displays the typical asymmetric profile common in Lyman Break Galaxies (LBGs, see Chapter 8). Several low and high ionisation interstellar absorption lines are detected, indicated on the spectrum with vertical lines. These are NV $\lambda\lambda$ 1238.8,1242.8, SII λ1260, OI λ1302 + SiII λ 1304 , CII λ1334, and SiIV $\lambda\lambda$ 1393.8,1402.8, and SV λ1501.8 (not shown). NV $\lambda\lambda$ 1238.8,1242.8 shows the typical P Cygni profile which arises due to stellar winds, indicating ongoing star formation in the galaxy. This is because P Cygni profiles are only seen within 10 Myrs of the most recent episode of star formation as they are due to short lived OB stars. A close up of the Lyα line is shown in Figure 5.2. A sharp absorption in the blue wing of the Lyα line and an extended red wing is consistent with that observed in $z \sim 3$ LBGs (Shapley et al. 2003). In general in LBGs, the interstellar absorption lines display a blueshift relative to the systemic redshift, while Lyα is redshifted. The standard model to explain this velocity shift is an almost spherical outflow, in which the blueshifted absorp-

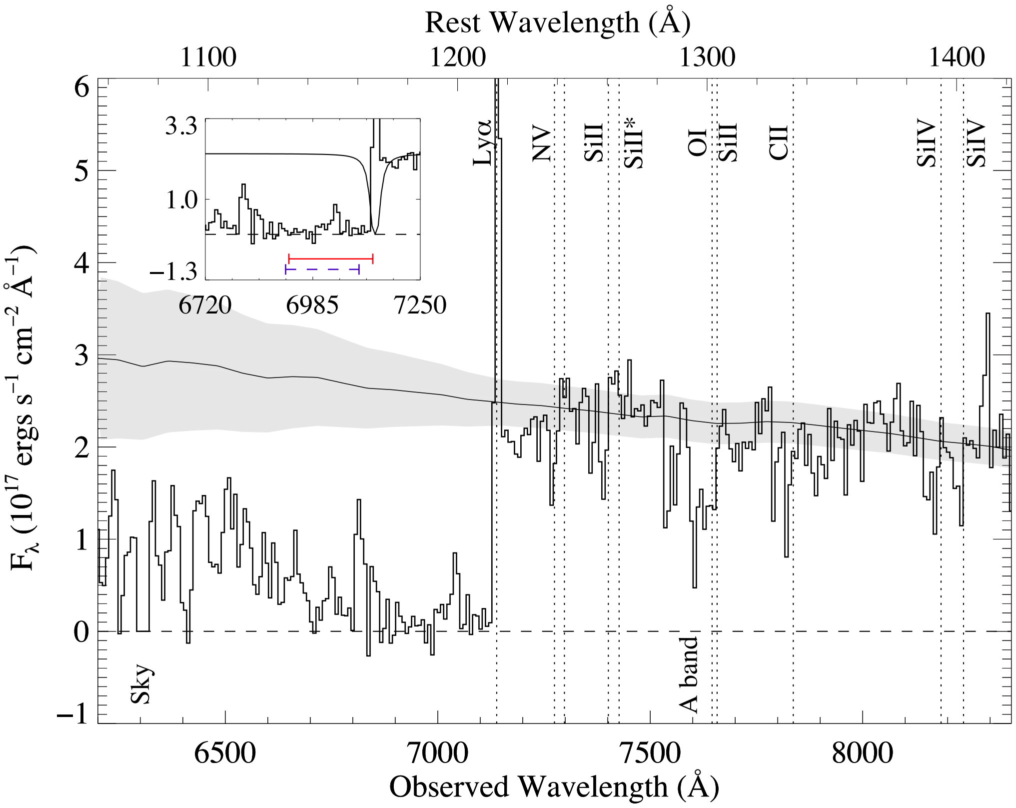

Figure 5.1: *Spectrum of A1689-7.1, with the model continuum and associated errors overlaid. Spectral features are indicated at the systemic redshift of z = 4.8722. The inset plot shows a HI profile fit to the data, as well as the extent of a proximity zone (solid line), and the extent of the first redshift bin used in* τ_{eff}^{GP} *calculations (dashed line). The atmospheric "A band" at 7600Å is marked, and contamination from the O* I *skyline at 6300Å has been removed.*

Table 5.1. Velocities of Blueshifted Interstellar Lines in A1689-7.1

Line	λ_{rest} (Å)	$\lambda_{expected}$ (Å)	$\lambda_{observed}$ (Å)	Velocity (km s^{-1})
N V	1238.82	7274.60	7265.41	378.99
Si II	1260.42	7401.45	7390.03	462.90
C II	1334.53	7836.64	7820.68	610.98
SiIV	1393.76	8184.44	8170.03	528.20
SiIV	1402.77	8237.36	8229.80	275.35

tion lines arise from the outflowing gas on the near side of the galaxy which is approaching the observer. The Lyα emission is suppressed due to resonant scattering, and the only photons which can escape unabsorbed in the direction of the observer are those which are backscattered off the receding gas on the far side of the galaxy, resulting in a redshift. The interstellar absorption lines provide a reasonably straightforward probe of the kinematics of the outflowing gas. Lyα emission also reflects the kinematics of the outflow, but the complexities of Lyα radiative transfer make its interpretation much more difficult (Erb et al. 2010). The average velocity of the blueshifted lines is $\Delta v = 450$km s^{-1}, and the values for five of these lines are shown in Table 5.1. Dust also strongly affects the Lyα line - a low amount of dust in a system will allow photons to escape more efficiently as interactions with dust particles cause scattering and absorption. The amount of dust present will strongly affect the intensity of the Lyα line, but not the shape of the profile or the equivalent width (Mas-Hesse et al. 2003). In the standard LBG picture, the frequently-observed offset in velocity between Lyα and the systemic redshift is interpreted as a gas outflow or "superwind" driven by the central starburst and supernovae. These types of outflows are observed at high redshift (e.g. Pettini et al. (2002); Shapley et al. (2003)), and in local starbursts (e.g. Mas-Hesse et al. (2003); Lehnert and Heckman (1996); Heckman (2002)).

5.2 H I Flux Transmission

On its way to us, the light from a galaxy or QSO (Quasi-Stellar Object, also known as a quasar) passes through intervening intergalactic gas, which leaves

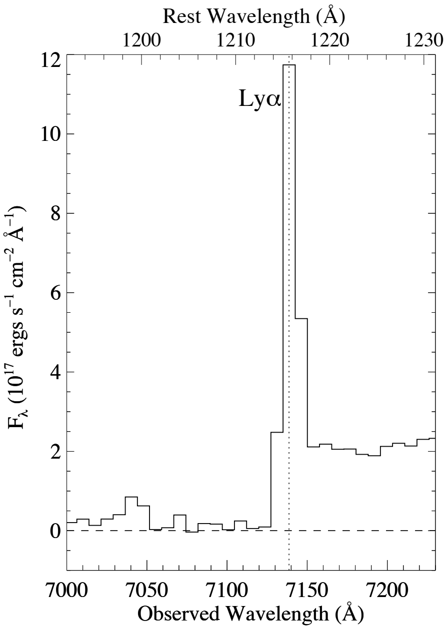

Figure 5.2: *VLT spectrum showing the asymmetrical Lyα emission. The systemic redshift is indicated by the dotted vertical line, which marks the expected position of the 1215.67Å line at $z = 4.8722$.*

an imprint on the spectrum. Neutral hydrogen atoms in the Universe preferentially absorb Lyα photons with a wavelength of 1216Å, and so the portion of the spectrum with rest-frame wavelengths less than 1216Å will be modified by absorption due to intervening intergalactic H I. This is because photons with wavelengths shorter than 1216Å leaving a QSO or galaxy and travelling toward the observer have their wavelength stretched due to the cosmological expansion. If there is a "clump" of neutral hydrogen in the path between the galaxy/QSO and observer, it will absorb any of these photons which have been shifted to 1216Å at the location of the clump. This will result in a dip or absorption trough in the spectrum of the QSO or galaxy at the location of 1216Å $\times$ $(1 + z_{absorber})$, which will depend on the size of the intervening system and its neutral hydrogen column density. This effect produces what is known as the Lyα-forest in the spectra of distant QSOs, which manifests as a "forest" of individual absorption lines, and which can be used to conduct studies of the intergalactic medium (IGM). The neutral fraction in the IGM is estimated to be about 1 part in 10^5 (Rauch 1998). The Lyα forest spectra toward QSOs exhibit regions of enhanced transmission close to their source, which are known as "proximity zones" (Carswell et al. 1982; Bajtlik et al. 1988). This enhanced transmission is due to the effect of the strong central ionising source in the QSO which drives an ionisation front into the nearby IGM and causes increased ionisation in Lyα clouds close to the QSO.

As expected, the stellar continuum of A1689-7.1 is observed redward of the Lyα line in the spectrum shown in Figure 5.1. The region immediately blueward of Lyα emission displays a Lyα-forest decrement as described above, highlighted in the inset plot of Figure 5.1. There is a broad spectral region with almost complete absorption, punctuated by two transmission spikes at $\sim$ 6800 Å and $\sim$ 7040 Å. The spectrum of a galaxy in the region below 1216Å acts as a map of the line of sight to the galaxy, with absorption troughs indicating the location of H I regions. The proximity of the complete absorption to the Lyα line indicates that there is a dense region of H I lying physically close to the A1689-7.1. The transmission spikes are likely to be representative of two separate highly-ionised regions along the line of sight.

In order to quantify the absorption caused by the neutral hydrogen in the line of sight, we examine the Gunn-Peterson (GP) effective optical depth of the IGM. The GP effect was proposed by Gunn and Peterson (1965) as a dark trough in the spectra of distant QSOs shortward of the Lyα line due to absorption by neutral hydrogen. A QSO will exhibit a GP trough in its spectrum if it resides in an environment containing a significant amount of H I. If a QSO could be observed at a redshift prior to the end of reionisation, a GP trough would appear in its spectrum below Lyα, as the IGM was largely neutral at such an epoch. Although proposed in 1965, the GP effect was not observed until Becker et al. (2001) detected a significant dark trough in the spectrum of a QSO at $z = 6.28$. This complete suppression of flux can be caused by relatively low amounts of neutral hydrogen (neutral fraction of $f_{HI} \sim 10^{-3}$, Fan et al. (2002)), and so the presence of a GP trough alone merely indicates the presence of a relatively large amount of H I compared to the post-reionisation IGM, but does not automatically signify the end of reionisation. Also there is increasing evidence that reionisation does not proceed homogeneously, with large line-of-sight variations between different QSOs-while the previously mentioned $z = 6.28$ QSO shows a complete absorption trough, the $z = 6.42$ QSO presented by Fan et al. (2002) shows clear transmission in the Lyα, Lyβ and Lyγ transitions. The $z = 6.28$ QSO from Becker et al. (2001) suffers from the ionising effect of the proximity zone as far from its centre as $z = 6.16$, and the GP trough is detected below this redshift, indicating that the neutral hydrogen is significantly removed from the QSO centre. Studying the gas phase close to a galaxy is not feasible with bright QSOs due to this ionising proximity effect, which can be as large as $\sim$ 16 physical Mpc at $z \sim 5$ (Fan et al. 2006). Normal star forming galaxies do not suffer from this effect, with galaxies at $z \sim 3$ having modest proximity zones of 0.1 - $0.5h^{-1}$ physical Mpc (Adelberger et al. 2003); however the population of star-forming galaxies is intrinsically faint, especially at the significantly earlier cosmic time of $z \sim 5$. Composite spectra of galaxies such as that of Shapley et al. (2003) cannot be used in this case, as the varying lines of sight toward different galaxies means that any structure in the IGM in a particular direction would be wiped out in combining spectra. The boost in brightness afforded by the magnification due to gravitational lensing and the long integration time acquired means that the spectrum of this ordinary galaxy is suitable for measurement of the transmitted flux ratio $\mathcal{T}$ in the Lyα forest. The Gunn-Peterson effective optical depth to Lyα photons is given by $\tau_{eff}^{GP} = -\ln(\mathcal{T})$ (Fan et al. 2006; Songaila 2004), where $\mathcal{T}$ is the ratio of the average observed flux to the average unabsorbed continuum:

$$\mathcal{T} =< f_{\lambda}/f_{cont} >$$

Fan et al. (2006) find a rapid evolution in the effective optical depth at $z > 5.5$ indicating an increase in the volume-averaged neutral fraction by a factor of at least 7 from $z = 5.5 - 6.2$, consistent with the IGM transition at the end stages of reionisation. In order to compare the τ_{eff}^{GP} averages for A1689-7.1 to the values computed by Fan et al. (2006), we used the same bin size as these authors, $\Delta z = 0.15$ in the rest frame of the source. τ_{eff}^{GP} was computed in 5 bins, extending shortward from the blue edge of Lyα at 1210Å to the wavelength cleared of the red wing of Lyβ + O VI, 1055Å. The redshift, central wavelengths and τ_{eff}^{GP} values for each bin are given in Table 5.2. The blue dashed line in the inset plot of Figure 5.1 shows the extent of the highest redshift bin. For comparison, the red (solid) line indicates the extent of a proximity zone that would exist if this object were a QSO. The continuum used to estimate f_{cont} is taken from the best-fit synthesised stellar spectrum from population modelling, which is outlined in Section 5.3. In creating this model to compare with observed points, we include a term to account for the attenuation in the Lyα forest (Madau 1995), so this term is removed to estimate the unattenuated continuum used here. This continuum is shown in

Table 5.2. Values of τ_{eff}^{GP} for the Lyα Forest in A1689-7.1

$z_{central}$	$\lambda_{central}$(Å)	τ_{eff}^{GP}
4.7654	7009	$3.667\ ^{+1.06}_{-0.50}$
4.6157	6827	$2.452\ ^{+0.49}_{-0.33}$
4.4660	6645	$2.078\ ^{+0.41}_{-0.29}$
4.3163	6463	$1.175\ ^{+0.21}_{-0.18}$
4.1666	6282	$1.461\ ^{+0.31}_{-0.23}$

Figure 5.1. The shaded region represents the errors on the continuum which we estimate to vary from 10% in the red to 30% in the blue. The errors on the τ_{eff}^{GP} values are dominated by sample variance-the intrinsic scatter in the continuum flux levels due to the stochastic nature of the IGM (Tepper-García and Fritze 2008). A continuum placement error is also folded into the reported error on τ_{eff}^{GP}, as well as a contribution from shot noise.

Figure 5.3 shows the results of these τ_{eff}^{GP} measurements. For comparison, measurements of τ_{eff}^{GP} towards QSOs from Songaila (2004), and from Fan et al. (2006) are also plotted. These authors carried out measurements of effective optical depths toward these quasars after first excluding the proximity zone, thus yielding information pertaining only to the pervasive IGM outside of the ionising influence of the source. The following power law fit to the effective optical depths of the plotted QSOs with $z < 5.5$ was calculated by Fan et al. (2006):

$$\tau_{eff}^{GP} = (0.85 \pm 0.06)\left(\frac{1+z}{5}\right)^{4.3\pm0.3}$$

which is displayed as a dashed line in Figure 5.3. The dotted line is a log-normal effective optical depth distribution given by Becker et al. (2007). For a lognormal distribution $E[X] = e^{\mu+\sigma^2/2}$, the lognormal parameters given for this curve are: $\mu(z) = (-9.35 \pm 0.17) + (1.79 \pm 0.04)(1+z)$ and $\sigma(z) = (4.19 \pm 0.16) - (0.46 \pm 0.03)(1+z)$. The shaded region represents the combined errors from the two curves. As the effective optical depth is a function of redshift, it would be reasonable to assume that toward A1689-7.1, τ_{eff}^{GP} would rise steadily with increasing redshift bin in line with the evolution in these two fits. The values of τ_{eff}^{GP} for A1689-7.1 are in good agreement at $z < 4.5$, while

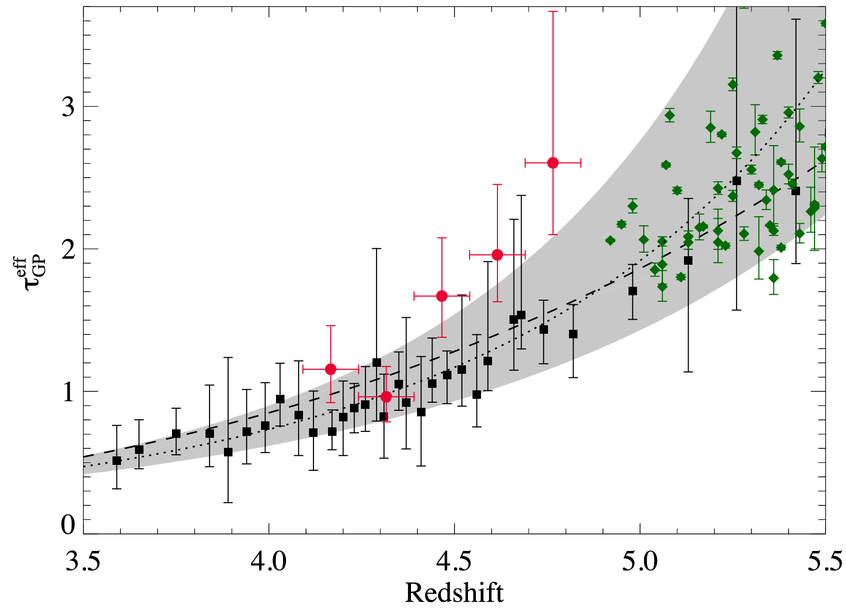

Figure 5.3: *Measurements of the Gunn-Peterson effective optical depth,* τ_{eff}^{GP} *towards A1689-7.1 (red circles), and towards QSOs from Songaila (2004) (black squares) and Fan et al. (2006) (green diamonds). The dashed line represents the power-law fit from Fan et al. (2006), while the dotted line represents the lognormal effective optical depth distribution given by Becker et al. (2007). The associated errors on the two curves are combined and shown as the grey shaded region.*

at $z > 4.5$ the points become increasingly deviant from both fits as a significant excess in τ_{eff}^{GP} becomes apparent. The highest redshift bin represents a physical size of 14 Mpc (indicated by a dashed line in the inset of Figure 5.1), and this point is the most deviant from the fit, suggesting an excess of neutral hydrogen in close proximity to the galaxy compared to the IGM at the same redshift.

LBGs at $z \sim 3$ have been shown to contain modest proximity regions of 0.1-0.5 h^{-1} comoving Mpc, but on scales of $\sim 1 - 5h^{-1}$ comoving Mpc they are associated with an excess of neutral hydrogen Adelberger et al. (2003). Guimarães et al. (2007) compare the theoretically-expected decrease in optical depth toward $z > 4$ QSOs due to the proximity effect with the observed decrease and find evidence for gaseous overdensities with sizes of $15h^{-1}$Mpc. At $z \sim 5$, in order to examine the A1689-7.1 spectrum in the context of other galaxies, we can only compare with a limited sample of high quality spectra. Swinbank et al. (2007), Franx et al. (1997) and Dow-Hygelund et al. (2005) all present spectra of lensed star-forming galaxies at $z = 4.88$, 4.92, and 5.5 respectively, while Kawai et al. (2006) and Price et al. (2007) examine the spectra of gamma-ray burst (GRB) host galaxies at $z = 6.295$ and 4.941 respectively. Kawai et al. (2006) report that their spectrum of a GRB host galaxy at $z = 6.295$ has a flux consistent with zero in the range 8500-8900Å, shortward of the Lyα emission. These authors note however the possibility of the absorption being due to a damped Lyα (DLA) system associated with the host galaxy which is a phenomenon observed in several lower-redshift GRB afterglows (e.g. Vreeswijk et al. (2004); Berger et al. (2006)). Price et al. (2007) also identify a possible DLA at the position of the galaxy in the spectrum of GRB 060510B at $z = 4.941$, but find a further strong absorption feature not associated with the DLA, indicating the presence of an amount of neutral IGM not associated with the galaxy. While these GRB spectra are good indicators of H I overdensities, they are not suited to deep integration times as they fade rapidly after the initial burst. Neither Kawai et al. (2006) or Price et al. (2007) present a quantitative analysis of the transmission fraction in the absorbed regions in their GRB spectra. A reanalysis of these, and future high-quality GRB spectra in terms of τ_{eff}^{GP} could provide an interesting sample to compare with high-redshift star-forming galaxies. The only one of the star-forming galaxy spectra listed above which shows a similar absorption trough to A1689-7.1 is that of the galaxy at $z = 4.88$ shown in Swinbank et al. (2007). These authors use a fitting procedure to model the Lyα line and the underlying IGM, and find that the best fit to the absorption in the line is based on an individual cloud (or clouds) of neutral hydrogen lying between -85 and +10 comoving kpc from the galaxy. These results are in keeping with A1689-7.1 but cannot be directly compared here as τ_{eff}^{GP} measurements for the $z = 4.88$ galaxy are not computed by Swinbank et al. (2007). These two similar objects are both detected behind lensing clusters and are likely to be representative of young, actively star-forming galaxies which have not yet significantly ionised their surrounding IGM or completed accumulating their mass. Further targeted studies of such objects in lensing clusters with powerful telescopes such as the forthcoming James Webb Space Telescope (JWST) and the next generation of large ground-based telescopes such as the European Extremely Large Telescope (E-ELT), the Giant Magellan Telescope (GMT) and the Thirty Meter Telescope (TMT) will add to the sample of these types of galaxies and allow studies of the IGM in their vicinity to become a significant subfield in astronomy at $z \sim 5$.

The studies of absorption toward QSOs (e.g. Fan et al. (2006); Becker et al. (2007)), and the discovery of a population of Lyα emitters at $5.7 < z < 6.5$ (e.g. Stern et al. (2005); Malhotra and Rhoads (2006)) indicate that reionisation proceeded inhomogeneously, and was most likely reaching the overlapping stage prior to completion close to $z \sim 6$. Results from the WMAP 5-year data indicate a significantly higher reionisation redshift of $z = 10.4 \pm 1.4$ (Komatsu et al. 2009).[1] Hence it is important to stress that these results should not be interpreted as a signpost to a later completion of reionisation. Instead, the more likely scenario would be a galaxy residing in a large-scale overdensity of neutral gas. General cosmological hydrodynamical and N-body simulations (such as the Millennium Simulation Springel et al. (2005)) sees the densest structures forming at the nodes of a filamentary network. According to the smoothed particle hydrodynamical simulations of Kereš et al. (2005) and Birnboim and Dekel (2003), a consistent picture of galaxy formation is emerging in which at high redshifts and for low-mass galaxies, a cold-mode of accretion is the dominant way that galaxies acquire their gas. Kereš et al. (2005) find that this cold-mode accretion can be directed along the large-scale filaments, allowing galaxies to draw their gas from a large distance. A1689-7.1 is likely to be located close to one of these dense neutral filaments or nodes and to

---

[1] See McQuinn (2010) for a review on promising observational methods for detecting the epoch of reionisation.

be funnelling its gas to fuel its ongoing star formation from the surrounding neutral IGM.

Following the publication of this work (Frye et al. 2008), a study of the extended neighbourhood of this galaxy was carried out by Matsuda et al. (2010) in order to search for an overdensity of galaxies within this gas-rich environment. The past decade has seen a number of detections of high-redshift protoclusters, e.g. Matsuda et al. (2005); Steidel et al. (2000); Pentericci et al. (2000). These overdensities of galaxies are likely to be early incarnations of the massive clusters which exist at low redshift. The survey by Matsuda et al. (2010) in the vicinity of A1689-7.1 finds another candidate protocluster, with a large-scale galaxy overdensity in a region of ∼20 × 60 comoving Mpc at a redshift of $z = 4.86 \pm 0.03$. This is the earliest indication of a protocluster, and suggests that by $z \sim 5$ these regions in the IGM with high neutral fractions are already beginning to host the building blocks of what will become the largest gravitationally bound structures in the Universe.

5.3 Stellar Population Synthesis Models & SED Fitting

The ultraviolet-to-infrared spectra of any (non-AGN) galaxy arises from its stellar light, either light which is directly emitted, or that which has been reprocessed by gas and dust in the interstellar medium (ISM) and re-emitted at longer wavelengths. Hence the spectral energy distribution (SED) in the UV-IR wavelength regime encodes a wealth of information about the stellar population. In order to recover such information, it is useful to take observations of the galaxy in these wavebands and compare with SEDs of model galaxies. In this manner, one can investigate constraints on important galaxy properties such as age, star formation history, stellar content and dust extinction. To generate model spectra, I utilised the stellar population synthesis code of Bruzual and Charlot (2003, hereafter BC03), and compared this model to photometric observations of A1689-7.1 in various bandpasses.

Table 5.3. Photometry of A1689-7.1

Telescope	Instrument	Filter	Apparent Magnitude (AB)
HST	ACS/WFC	i_{775}	23.10 ± 0.01
HST	NICMOS	J_{110}	23.10 ± 0.02
ESO NTT	SOFI	H Johnson	23.45±0.38
ESO NTT	SOFI	K_s SOFI	23.45±0.35
Spitzer	IRAC	3.6μ m	23.30 ± 0.02
Spitzer	IRAC	4.5μ m	23.34 ± 0.03

5.3.1 Photometric Observations

Collaborators Dr. Dan Coe and Dr. Eiichi Egami have kindly shared photometric results on A1689-7.1 to use in this work. The central region of the rich cluster A1689 was imaged by HST Advanced Camera for Surveys (ACS) as part of a GTO (Guaranteed Time Observer) redshift survey program. The filters used were g_{475}, r_{625}, i_{775} and z_{850} filters, reaching limiting magnitudes of 27.5, 27.2, 27.2 and 26.7 respectively; details of these observations are outlined in Broadhurst et al. (2005). The NICMOS instrument on HST was used for the J_{110} image. Ground-based observations in the H and K_s bands were made using the SOFI instrument on the ESO New Technology Telescope (Coe et al. 2003). Deep imaging was obtained using the Spitzer telescope with the IRAC instrument (Egami et al. 2006) in the 3.6μm and 4.5μm bands. Details of the photometric results for A1689-7.1 are given in Table 5.3. As outlined in Section 8.1 and shown in Figure 8.1, this galaxy is a V-band dropout, and so the shortest wavelength filter with a reliable photometric detection is the i_{775} band.

5.3.2 SED Models

In order to generate the SED of a galaxy, the BC03 code combines integrated stellar populations. The user must specify a metallicity, an initial mass function (IMF), and a population age. The "age" (t) is defined as the time since the onset of the formation of the dominant stellar population. One must also specify a particular star formation history (SFH) as a function of this population age. The code combines a series of isochrones as a function of time based on this SFH, and theoretical evolutionary tracks are used to predict the luminosities and effective temperatures for stars as a function of mass and age. In order to finally generate the spectrum, stellar libraries are used, and the code sums over the distribution of stars present at each time step. The stellar libraries utilised by the BC03 models are based on two types of IMF, the Chabrier IMF (Chabrier 2003) or the Salpeter IMF (Salpeter 1955). We chose to use the Chabrier IMF, and the recommended Padova 1994 stellar evolutionary track. There are both high and low resolution models available, which span a wide wavelength range. For this work, we chose to use the low-resolution version, which provides 1221 wavelength points over the range 91Å to 160μm. The code outputs a synthetic spectrum with luminosity, l_λ in units of solar luminosity $L_\odot$ per unit wavelength Å as a function of wavelength. This is converted to flux density at redshift z, given by:

$$F_\lambda = \frac{l_\lambda \, L_\odot \, M_*}{(1+z)\, 4\, \pi \, D_L^2(z)\, m^*(t)} \, 10^{-0.4 A_{\lambda_0}} \; e^{-\tau_{IGM(z,\lambda)}} \tag{5.1}$$

The terms in this equation are explained below.

- The output synthetic spectra are normalised so that the total mass of gas and stars is $1M_\odot$, and the total stellar mass $m^*(t)$ is given for each time step. The mass can hence be scaled to any chosen mass M_*
- The term $10^{-0.4A_{\lambda_0}}$ is the contribution by dust. The dust attenuation $A_{\lambda_0} = E(B-V)k(\lambda)$ where E(B-V) represents the colour excess. It is the value of E(B-V) which we vary in our models, as the starburst extinction law $k(\lambda)$ is a function of wavelength outlined in Calzetti et al. (2000):

  $$\begin{aligned} k(\lambda) &= 2.659(-1.857 + 1.040/\lambda) + R_V, \\ &\qquad 0.63\mu m \leq \lambda \leq 2.20\mu m; \\ &= 2.659(-2.156 + 1.509/\lambda - 0.198/\lambda^2 + 0.011/\lambda^3) + R_V, \\ &\qquad 0.12\mu m \leq \lambda \leq 0.63\mu m \end{aligned} \tag{5.2}$$

  where R_V is the ratio of total to selective extinction. For starburst galaxies Calzetti et al. (2000) give $R_V = 4.05 \pm 0.80$.
- $e^{-\tau_{IGM(z,\lambda)}}$ is a term which accounts for the effect of attenuation due to Lyman-forest absorption at wavelengths shortward of 1216Å, as given by Madau (1995). The model for attenuation from Madau (1995) is based on

the underlying assumption that the observed flux of a source at redshift z is given by the product of the intrinsic flux and a transmission factor that accounts for the mean absorption as a function of wavelength.

- D_L is the luminosity distance in centimetres. The $(1+z)$ term accounts for the frequency stretching between the rest frame and the observed frame at redshift z.

This model spectrum is then convolved with the transmission response of the filter that each observation was taken with:

$$F_{\lambda,filter} = \frac{\sum T\, F_{\lambda}\, \lambda}{\sum F_{\lambda}\, \lambda} \tag{5.3}$$

where T is the transmission function of the filter. We can then convert this filter-corrected flux density into the corresponding AB magnitudes in each pass band with the conversion:

$$M_{AB} = -2.5\ log_{10}(F_{\lambda,filter}\ \lambda_c^2/c) - 48.57 \tag{5.4}$$

where 48.57 is a constant for the AB magnitude system given by Oke and Gunn (1983), and λ_c is the central wavelength of the passband. These synthetic photometric points are compared with the observed photometric points in order to find the SED most closely matching the true galaxy properties. The best fitting model is that which gives the lowest value for the reduced χ^2 statistic:

$$\chi_p^2 = \frac{\sum_N (D_i - F_i)^2/\sigma_i^2}{n_{dof}} \tag{5.5}$$

where D_i is the set of N observed points with associated errors σ_i, and F_i is the set of N synthetic points. The degrees of freedom, $n_{dof} = N - p$ where p is the number of free parameters in the model fit. These are:

- Metallicity: The BC03 model suite provides a range of metallicities. The metallicity is set while generating the initial model, and this was chosen to be solar metallicity.

- Star Formation History: The options we examined for the star formation history are those which have an instantaneous burst burst of star formation at t=0, or those which have a star formation rate which declines exponentially with time, such that $SFR(t) \propto exp(t/\tau)$. After finding the instantaneous bursts were producing unsatisfactory results in all cases, a range of values 100 Myr$< \tau <$1 Gyr were explored, and the best fits were found to be those with $\tau = 300$ Myr.

- Dust: The amount of dust in the galaxy is given by the colour excess E(B-V). It was observed that large amounts of dust significantly alters the slope in the bluest part of our SED, and find that any model with $E(B-V) > 0.1$ was a poor fit to the slope of data points in this region, and so we restricted our search to models with $E(B-V) \leq 0.1$.
- Age: As the age of the model cannot exceed the age of the Universe at $z \sim 4.8$, the upper limit on the age is 1.2 Gyrs. The BC03 models allow ages in discrete time steps, and a subset of these ages from 5 Myrs up to 1.2 Gyrs were explored. Shapley et al. (2003) show median star-forming lifetimes for Lyman-break galaxies of $\approx$ 300 Myr, and so it would be reasonable to expect the age at $z \sim 5$ to be similar or shorter than this value.
- Mass M_*: No prior constraints are available on the mass. As a guideline, Pirzkal et al. (2007) examine a sample of 9 Lyα-emitting galaxies in the range $4.0 < z < 5.7$ and find masses of $10^6 - 10^8 M_\odot$. We explore the mass range $10^6 M_\odot < M_* < 10^{10} M_\odot$.

The minimum value achieved for χ^2 was 0.647, and the parameters used to generate this model were: Age (t) $= 114 \pm 50$ Myr, mass $M^* = 7.3 \pm 0.7 \times 10^8 M_\odot$, and dust $E(B-V) = 0.0^{+0.02}_{-0.00}$; hence we have a small galaxy with little to no obscuration by dust, which is viewed at an early stage in its star formation timescale. Figure 5.4 shows the best fitting SED model, with the observed photometric points shown as red filled circles, and the synthetic points used for comparison are shown as open circles. The rest-frame 4000Å break (discussed in more depth in Section 7.2) is caused by the buildup of a large number of absorption lines due to mainly ionised metals, and is strongest in old, metal-rich galaxies. The photometric passbands covered in this spectrum bracket this feature, and the and the resultant SED recovers well the slope of the points on either side of this break.

Formal confidence intervals were also generated based on a prescription from Cash (1976), which was originally developed for use with X-ray spectral data. In this case, we consider a set of p parameters, which for our model is 5: age, mass, E(B-V), metallicity and star formation decay rate τ. The number of

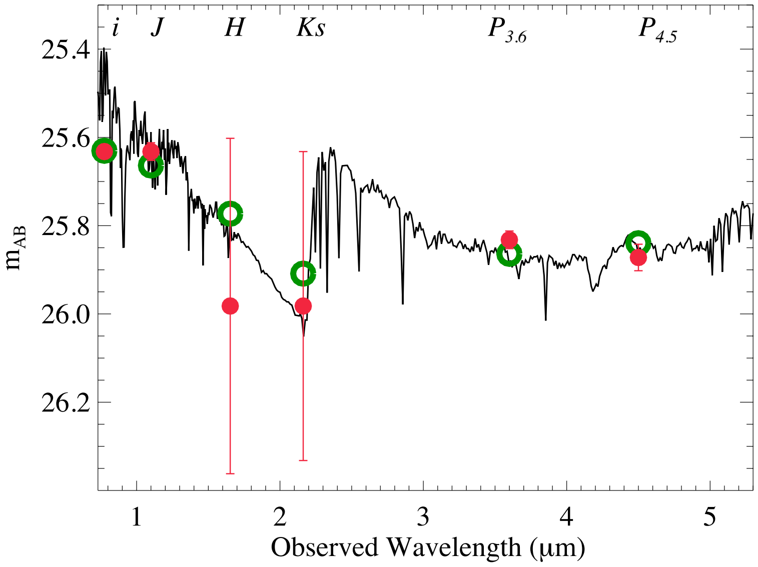

Figure 5.4: *Result for best-fit SED model, with real photometric points (filled circles) and synthetic photometric points (open circles). The larger error bars on the H and K_s points reflect the fact that these are ground-based observations, while the rest are space-based.*

degrees of freedom is given by $N - p = 1$. If we now freeze q of the model parameters, where $q < p$, and consider their values to be the true values, then we are free only to vary the remaining $p - q$ parameters. A fit to this $p - q$ subset will yield some value which is the minimum in the parameter subset, which we take to be the true minimum, χ^2_{p-q}. Cash (1976) states that $\chi^2_{p-q} - \chi^2_p$ will have a lower limit of χ^2_q with q degrees of freedom for large N. From this, Cash (1976) determine that $\chi^2_{p-q} - \chi^2_q > \chi^2_p$ with a probability α. In the limit of large N, the true value of a q-parameter subset with probability $1 - \alpha$, will be enclosed by the locus of points in the q-dimensional parameter space where the subset deviation is equal to $\chi^2_q(\alpha)$. As we have chosen to fix the values for metallicity and τ in our models, there are 3 parameters remaining which we can vary. We vary one parameter at a time, fixing the $q = 4$ other parameters, such that $p - q = 1$. For q =4 and $\alpha = 68\%$, $\chi^2_q(\alpha) = 4.7$. We consider our best-fit model to be the true minimum, hence $\chi^2_{p-q} = 0.647$. We then raise the variable parameter until χ^2_{p-q} increases by 4.7, and likewise lower the variable until χ^2_{p-q} again increases by 4.7, thus yielding the 68% formal confidence intervals for our fitting process. The results of this process can be seen in Figure 5.5. Although we only have a small value for N, we are confident that this approach is still reliable, as our data covers both sides of the prominent

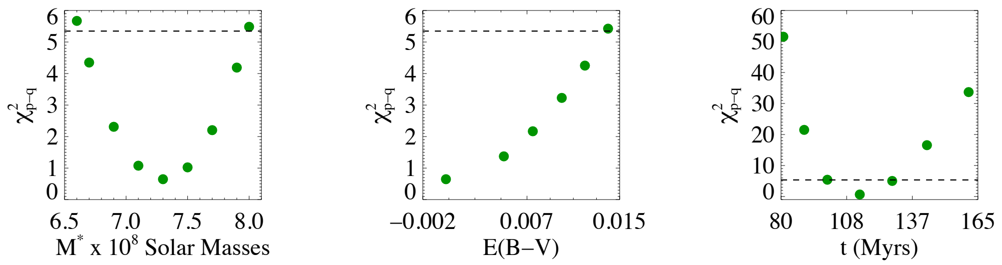

Figure 5.5: *Generation of formal confidence intervals for the SED models. The minimum point in each plot is the best fit value, and is varied until the value of* χ^2_{p-q} *increases by* $\chi^2_q(\alpha)$*. The dashed line indicates this value, 0.647+4.7.*

4000Å break, and we find that adding further noisy ground-based data does not significantly alter the result.

5.3.3 Star Formation Rate Estimates

Star formation is the key driver of the buildup of structure as galaxies form, and the rate of star formation strongly influences galaxy evolution. In order to make an estimate of the star formation rate (SFR) in this galaxy, we use the ultraviolet flux of the galaxy model at rest frame 1400Å, $\mathrm{F}_\nu(1400\ \text{Å})$. Using the UV region of the spectrum means that we are looking at wavelengths where light from young stars dominates the spectrum, and so the SFR scales linearly with luminosity. $\mathrm{F}_\nu(1400\ \text{Å})$ of the best-fit SED was measured within a synthetic top-hat filter of rest-frame width 300Å centred on rest-frame 1400Å. To convert the observed flux F_ν given in the model SED to emitted rest-frame luminosity, we use Equation 6 from Hogg et al. (2002):

$$\mathrm{L}_\nu(\nu_e) = \frac{4\ \pi\ D_L^2}{1+z}\ \mathrm{F}_\nu(\nu_o) \tag{5.6}$$

where the subscripts 'e' and 'o' refer to emitted and observed respectively, and D_L is the luminosity distance in centimetres. In the observed SED, the top-hat filter runs from $1250 \times (1+z) - 1550\ \times (1+z)$, and the flux $\mathrm{F}_\nu(\nu_o)$ is averaged over this box. For the best-fit SED, this gives $\mathrm{L}_\nu(\nu_e) = 9.4 \times 10^{28}$ ergs s^{-1}. The conversion to star formation rate (SFR) is given by Frye et al. (2007) :

$$\mathrm{SFR}_{UV}(M_\odot\ \mathrm{yr}^{-1}) = \frac{L_\nu(\nu_e, 1400\text{Å})}{7.14 \times 10^{27}} \tag{5.7}$$

resulting in an SFR of 13.13±1 $M_\odot$ yr^{-1}. The equation used to convert to star formation rate is based on a Salpeter IMF, and as our models are calculated using a Chabrier IMF, one must divide this result by a factor of 1.8 to convert, giving a final best estimate for SFR$_{UV}$ of 7.29±0.56 $M_\odot$ yr^{-1}.

Atek et al. (2008) report the use of the Lyα line as an indicator of star formation rate which reflects the population of massive young stars with ages of less than 20 Myr. These authors give the star formation rate for Lyα (based on Case B recombination) as:

$$\mathrm{SFR}_{Ly\alpha}(M_\odot\ \mathrm{yr}^{-1}) = 9.1 \times 10^{-43} L(\mathrm{Ly}\alpha)\ (\mathrm{ergs\ s}^{-1}) \tag{5.8}$$

The line flux of Lyα measured from the spectrum is F(Lyα) = 4.95×10^{-16} ergs s^{-1} cm^{-2} before correction for magnification. This results in a final value of SFR$_{Ly\alpha}$ = 11.05 ± 0.86 $M_\odot$ yr^{-1} after correction by a factor of 10 to account for the magnification. Swinbank et al. (2007) report a star formation rate of 12±2 $M_\odot$ yr^{-1} for the galaxy at $z = 4.88$ based on the [O II] line flux. The [O II]$\lambda\lambda$3726.1,3728.8 fluxes from the SINFONI observations of our galaxy have kindly been made available for comparison by Dr. Brenda Frye and collaborators, and are as follows (before correction for magnification): F([O II])λ3726.1 = 2.1±0.1 $\times10^{-17}$ ergs s^{-1} cm^{-2}, F([O II])λ3728.8 = 1.7±0.1 $\times10^{-17}$ ergs s^{-1} cm^{-2}. Using [O II] as an SFR indicator is covered in greater detail in Chapter 7, and we use Equation 7.18 taken from Kewley et al. (2004), resulting in a value of SFR$_{[OII]}$ = 6.2 ± 1.2 $M_\odot$ yr^{-1} for this galaxy. Given the well-documented discrepancies between SFR indicators, the three values presented here are in reasonably good agreement with one another. Pirzkal et al. (2007) examine a sample of 9 Lyα-emitting galaxies in the range $4.0 < z < 5.7$ and find similarly small masses ($10^6 - 10^8 M_\odot$), ages ($\sim$ 100 Myrs) and SFRs (8 $M_\odot$ yr^{-1}), compounding the conclusion that this galaxy is a good example of a typical member of the population at this epoch.

Table 5.4. Star Formation Rates for A1689-7.1

SFR Indicator	SFR ($M_{\odot}\mathrm{yr}^{-1}$)
UV (SED model)	7.29 ± 0.56
Lyα	11.05 ± 0.86
[O II]	6.2 ± 1.2

6

Hubble Space Telescope Grism Survey of Galaxy Cluster Abell 1689

6.1 Grism Spectroscopy

As outlined in Chapter 3, the field of the cluster Abell 1689 was observed using the HST G800L grism for three orbits. This chapter presents the grism spectroscopy obtained for 42 galaxies in a flux-limited sample with $i_{775} < 27.3$. The spectra selected from the sample to be of interest are those displaying emission lines above the continuum. We define an "emission line galaxy" (ELG) to be a galaxy having emission detected in the grism image. ELGs tend to host active galactic nuclei, intense star formation or both. The line emitting region of the galaxy is often confined to a small region or knot, and the term "emission line source" defines line emission which is distinct in position and wavelength. In some cases multiple ELSs, typically star-forming knots or a galaxy nucleus, were detected within a single ELG. In turn, the spectrum of each ELS will exhibit one or more emission lines (ELs). There are in total 42 ELGs containing 50 ELSs, and these 50 spectra display a total of 65 ELs. The emission lines were then examined and identified independently by both myself and Dr. Brenda Frye, and redshifts were determined. In the case of galaxies with multiple ELs, redshift determination is relatively straightforward, as the wavelength separation of the two lines will usually correspond to a combination of common strong emission lines. In many cases we detect the blended doublets [O III]$\lambda\lambda$4959,5007 and [O II]$\lambda\lambda$3726,3729 (eg Fig. 6.8). The resolution of the grism spectra is poor (R $\sim$ 90) so Hβ is often also blended with [O III]. Another combination of ELs detected was Hα and [O III]. Many of the ELGs had been detected in previous studies of A1689, and a number of galaxies had previously known spectroscopic redshifts from the catalogs of Duc et al. (2002), Balogh et al. (2002), Frye et al. (2007), and a small number had a spectroscopic redshift acquired from Dr. Johan Richard (private communication). For a galaxy with a previously known spectroscopic redshift it was relatively easy to identify a single emission line. For the remaining galaxies with single ELs, identifying lines became somewhat more difficult. The photometric redshifts from collaborator Dr. Dan Coe (Coe et al. 2003) were used as a guideline but other checks were also implemented-for example if a line was suspected to be [O II], one would check for the expected appearance of [O III] at the corresponding wavelength, or similarly, for other lines. This is not always possible due to the limited wavelength range (5700 - 9800 Å) of the spectra. Strong features such as the 4000 Å break and the Lyman-series break were also used as a guideline. Some spectra were removed from the original sample after the emission lines were deemed to be spurious detections. One example of this was a line which initially appeared to be an emission line, but was actually a continuum feature sandwiched between two strong absorption fields. In other cases, the lines flagged by the code as emission lines were barely detected above the continuum noise level. The Table 6.1 gives galaxy RA and DEC, i_{775} AB magnitude, emission line observed wavelength, line flux, rest-frame equivalent width, line species, redshift and spectroscopic reference in the literature. Over half of the galaxies detected in this survey are new detections, despite the multiple previous spectroscopic studies of this large lensing cluster field.

Table 6.1. Emission Line Galaxies in the Field of A1689

ID	RA (∘)	DEC (∘)	i_{775} (AB)	Line Center (Å)	$\log(F_l)$ ($erg\ s^{-1}\ cm^{-2}$)	REW (Å)	Line ID	z_{grism}	Ref
6621	13.189628	-1.3506333	26.69 ± 0.04	6712.4	-16.63	429.2 ± 276.5	[OII]	0.800	
11260	13.190046	-1.348567	24.21 ± 0.01	9010.5	-15.74	2034.8 ± 483.0	[OIII]	0.810	
6381	13.190094	-1.341133	24.17 ± 0.01	8740.6	-16.06	97.2 ± 19.5	[OIII]	0.758	
11186	13.190131	-1.353053	18.33 ± 0.01	8126.7	-15.86	6.1 ± 1.4	Hα	0.235	b
11136	13.190185	-1.357363	23.32 ± 0.01	8045.1	-16.35	65.8 ± 15.2	[OIII]	0.615	
11322	13.190542	-1.326375	19.82 ± 0.01	9505.6	-16.18	67.5 ± 16.1	Hα	0.449	b
6182	13.190737	-1.324731	24.66 ± 0.01	8383.4	-16.54	59.4 ± 20.0	Hα	0.277	
11226	13.190740	-1.3298028	21.61 ± 0.01	7783.1	-16.61	13.3 ± 5.0	Hα	0.186	
11040	13.190872	-1.349414	18.97 ± 0.01	7983.6	-16.09	10.7 ± 2.7	Hα	0.215	a, b
4752	13.190875	-1.3495417	18.97 ± 0.01	7956.9	-16.06	10.8 ± 1.3	Hα	0.212	a, b
6680	13.190824	-1.311189	25.83 ± 0.03	7332.8	-16.59	< 87	[OIII]	0.470	
5582	13.190834	-1.334439	26.32 ± 0.04	7531.3	-16.42	66.3 ± 17.9	[OIII]	0.510	
11324	13.190896	-1.313931	21.70 ± 0.01	6913.5	-16.55	54.6 ± 15.1	[OIII]	0.384	e
4971	13.190906	-1.349731	18.97 ± 0.01	7972.9	-15.89	64.1 ± 8.7	Hα	0.202	a, b
6583	13.190941	-1.309417	″	7932.0	-16.69	< 50	[OIII]	0.590	
6578	13.190947	-1.309414	23.84 ± 0.01	7917.2	-16.19	< 137	[OIII]	0.590	
4277	13.191041	-1.352267	20.70 ± 0.01	9571.7	-15.62	18.3 ± 1.7	Hα	0.462	
4298	13.191076	-1.351167	21.74 ± 0.01	7933.4	-15.74	70.4 ± 5.5	Hα	0.209	
″	″	″	″	6012.6	-15.77	17.5 ± 2.2	[OIII]	″	
″	″	″	″	8128.4	-16.20	18.1 ± 2.6	[SII]	″	
4251	13.191098	-1.350869	21.74 ± 0.01	7978.2	-16.21	57.8 ± 12.1	Hα	0.210	
5700	13.191123	-1.321883	22.04 ± 0.01	7966.7	-15.57	107.3 ± 6.0	[OII]	1.139	e
″	″	″	″	8235.6	-16.41	24.3 ± 3.6	[NeIII]	″	″
5570	13.191162	-1.323636	23.57 ± 0.01	8155.7	-16.19	73.4 ± 16.4	[OIII]	0.637	

Table 6.1 (cont'd)

ID	RA (∘)	DEC (∘)	i_{775} (AB)	Line Center (Å)	$\log(F_l)$ ($erg\ s^{-1}\ cm^{-2}$)	REW (Å)	Line ID	z_{grism}	Ref
11149	13.191176	-1.323664	22.34 ± 0.03	8115.4	-16.23	144.2 ± 42.4	[OIII]	0.629	
6154	13.191220	-1.309083	23.24 ± 0.01	7344.0	-16.31	127.2 ± 21.9	[OIII]	0.473	b
4744	13.191277	-1.338045	24.73 ± 0.02	8826.7	-15.74	149.3 ± 11.6	[OII]	1.368	
10640	13.191326	-1.361966	″	8928.1	-16.24	74.48 ± 19.29	[OIII]	0.785	
″	″	″	″	6656.1	-16.05	41.22 ± 6.63	[OII]	″	
10638	13.191334	-1.362022	″	6753.2	-16.16	26.12 ± 4.97	[OII]	0.811	
″	″	″	″	9020.8	-16.27	77.45 ± 7.7	[OIII]	″	
20002	13.191347	-1.362072	20.56 ± 0.01	8935.5	-15.98	77.82 ± 9.84	[OIII]	0.790	b
″	″	″	″	6673.2	-16.31	24.09 ± 4.16	[OII]	″	″
2630	13.191381	-1.363211	24.97 ± 0.02	6658.2	-16.44	104.3 ± 26.8	[OIII]	0.335	
2494	13.191546	-1.360030	24.21 ± 0.01	6071.8	-15.86	407.9 ± 66.3	[OIII]	0.215	
″	″	″	″	7970.2	-16.35	176.3 ± 45.9	Hα	″	
10746	13.191596	-1.350106	19.08 ± 0.01	8069.4	-16.09	21.2 ± 3.2	Hα	0.230	
11085	13.191659	-1.317806	20.43 ± 0.01	7652.2	-15.68	61.4 ± 4.2	Hα	0.165	
20004	13.191663	-1.317805	20.43 ± 0.01	7790.0	-16.15	28.4 ± 1.7	Hα	0.145	
″	″	″	″	7560.1	-15.86	29.3 ± 2.3	Hα	0.185	
5158	13.191787	-1.313802	24.62 ± 0.01	8332.8	-15.67	< 296	[OIII]	0.671	
″	″	″	″	8123.4	-16.80	$\cdots$	Hβ	0.671	
1946	13.191900	-1.360658	20.57 ± 0.01	8419.0	-15.71	78.5 ± 12.1	[OIII]	0.700	b, c
″	″	″	″	6352.2	-16.05	20.7 ± 4.7	[OII]	″	″
4194	13.191980	-1.323292	22.40 ± 0.01	8001.5	-16.31	29.1 ± 7.1	[OII]	1.145	e
10412	13.192066	-1.359247	20.65 ± 0.01	7736.1	-15.87	34.5 ± 8.0	Hα	0.179	
10782	13.192252	-1.326700	19.22 ± 0.01	7566.0	-15.88	27.6 ± 2.4	Hα	0.153	a
3203	13.192258	-1.326697	19.22 ± 0.01	7678.8	-15.26	72.4 ± 3.3	Hα	0.170	a

Table 6.1 (cont'd)

ID	RA (∘)	DEC (∘)	i_{775} (AB)	Line Center (Å)	log(F_l) ($erg\ s^{-1}\ cm^{-2}$)	REW (Å)	Line ID	z_{grism}	Ref
″	″	″	″	7866.8	-16.21	7.1 ± 1.0	[SII]	″	
10154	13.192360	-1.371497	20.26 ± 0.01	6715.2	-16.00	59.5 ± 9.2	[OIII]	0.115	b
10226	13.192504	-1.361381	20.02 ± 0.01	7479.4	-16.60	19.7 ± 7.1	Hα	0.140	
1651	13.192538	-1.3473694	25.51±0.02	8850.5	-15.94	434.2 ± 114.0	[OII]	1.38	
804	13.193044	-1.351555	26.91 ± 0.07	6588.0	-16.56	106.1 ± 33.6	[OIII]	0.320	
10399	13.193055	-1.330869	25.85 ± 0.02	7445.9	-16.63	< 100	Lyα	5.13	c, d
1077	13.193131	-1.341633	21.25 ± 0.01	7967.6	-16.17	23.2 ± 2.8	[OIII]	0.595	b, c
1184	13.193212	-1.337078	18.37± 0.01	6917.1	-15.42	61.3 ± 5.5	Hα	0.054	a, b
1157	13.193232	-1.336661	18.37± 0.01	7852.0	-14.82	133.6 ± 6.0	Hα	0.195	a, b
″	″	″	″	5970.9	-15.78	5.5 ± 1.1	[OIII]	″	″
″	″	″	″	5795.5	-15.53	3.5 ± 1.3	Hβ	″	″
″	″	″	″	7040.1	-15.94	8.6 ± 2.1	HeI	″	″
1507	13.193252	-1.326861	20.22 ± 0.01	7833.0	-16.37	15.7 ± 3.3	Hα	0.194	
1094	13.193518	-1.328469	19.44 ± 0.01	7848.0	-15.89	23.7 ± 2.2	Hα	0.195	a
″	″	″	″	8035.6	-16.38	6.7 ± 1.2	[SII]	″	
486	13.193702	-1.335958	26.08 ± 0.03	8057.7	-16.57	< 92	[OIII]	0.615	
20001	13.193894	-1.335958	20.28± 0.01	7901.7	-16.11	20.2 ± 2.2	Hα	0.205	a

[a] Spectroscopic redshift from the catalog of Balogh et al. (2002)

[b] Spectroscopic redshift from the catalog of Duc et al. (2002)

[c] Spectroscopic redshift from the catalog of Frye et al. (2007)

[d] Spectroscopic redshift from the catalog of Frye et al. (2002)

[e] Spectroscopic redshift from Richard et al. 2008, private communication.

6.2 Results

This galaxy sample covers a wide range of i_{775} magnitudes, $18 < i_{775} < 27$. The $(g - i)$ colour-magnitude diagram (CMD) is shown in Figure 6.1. Survey objects are plotted as red star symbols, while the green diamonds are objects with photometric redshifts which places them within the cluster (z = 0.187 ± 0.08). This cluster sequence populates the region with $(g-i) < 2$. The remaining black triangles are objects in the background or foreground. The red arrow represents the highest redshift object in the grism sample, a Lyα-emitter with $z = 5.13$, for which we only have an upper limit on the colour. The second highest outlier in the grism sample is an [O III] emitter at $z = 0.595$, with $(g - i) = 2.26$. Figure 6.2 shows the redshift distribution of the grism sample compared with the previously-known secure spectroscopic redshifts around the cluster redshift.

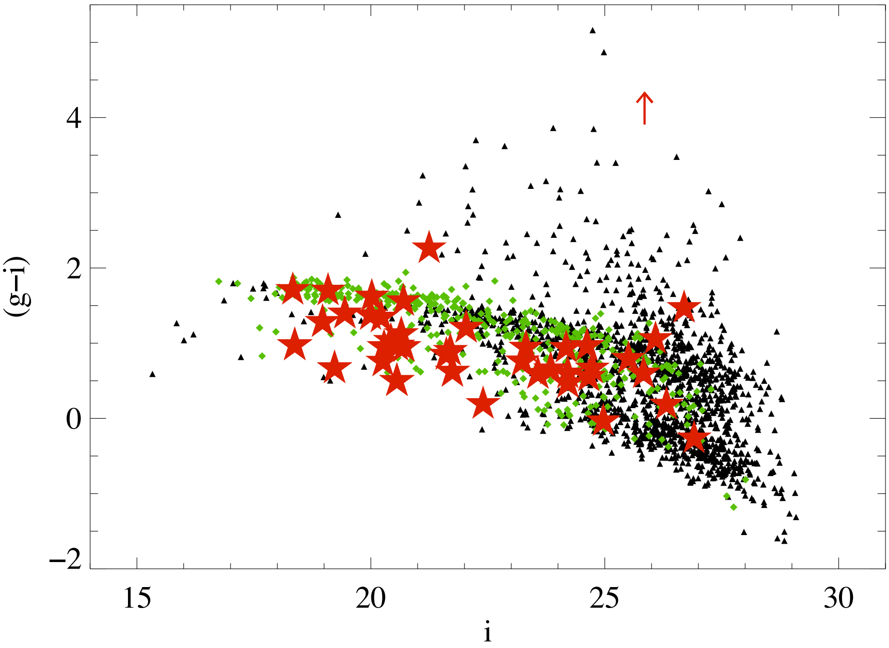

Figure 6.1: *Colour-magnitude diagram for HST ACS* g_{475} *and* i_{775} *AB magnitudes. Objects from this grism survey are shown as red stars. Green diamond-shaped symbols represent galaxies with photometric redshifts within the cluster (z = 0.187 ± 0.08), and black triangles represent galaxies with photometric redshifts which place them in the background or foreground. The red arrow represents the lower limit in* $(g - i)$ *for the g-band dropout galaxy at* $z = 5.13$ *(object #10399).*

Eight different line species are detected in our sample: Hα, [O III] $\lambda\lambda$4959,5007, Hβ, [Ne III] λ3869, He I λ4472, [O II] $\lambda\lambda$3726,3729 and Lyα. The most frequently observed line species is Hα, with the majority of Hα-emitting ELGs being cluster member galaxies owing to their brightness and high number density towards the centre of the cluster. The median redshift for the 24 Hα ELGs found by the grism is $z = 0.202$, close to the cluster redshift. The locations of the Hα-emitters detected in this survey are not significantly deviant from the samples presented in the surveys of Duc et al. (2002) and Balogh et al. (2002). The position of all known Hα-emitters within the cluster redshift range are presented in Figure 6.3, which also shows the location of the cluster centre and the Einstein radius. Typically, star formation rates in the high-density environments of galaxy clusters are found to be much lower than in the field. The Hα luminosity function found by Balogh et al. (2002) confirms this for

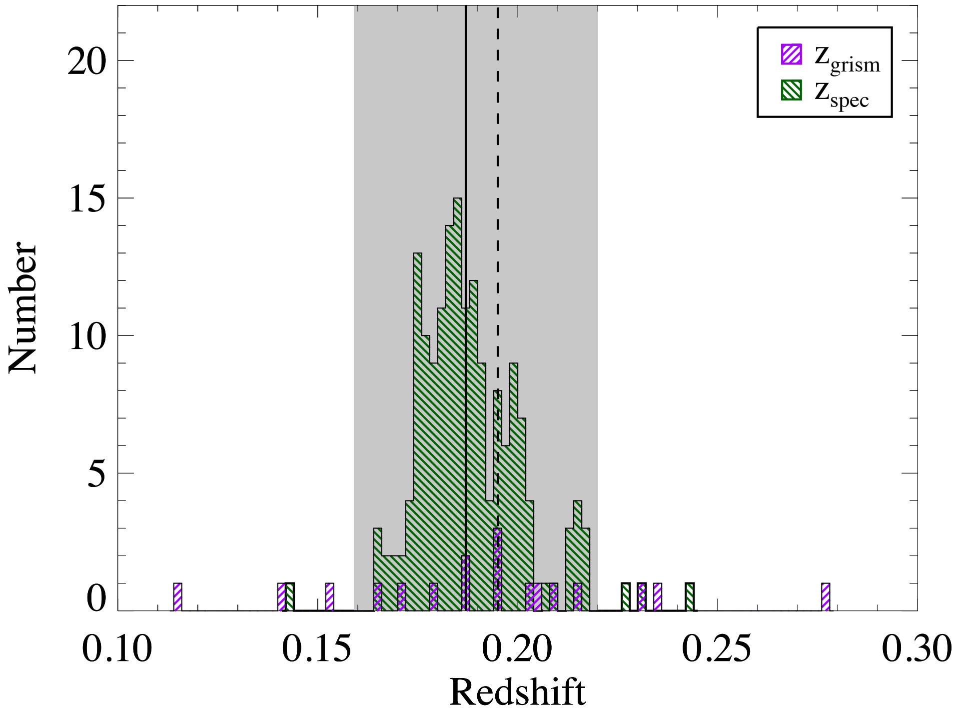

Figure 6.2: *Histogram showing the redshift distribution in the range* $0.1 < z < 0.3$ *for grism-detected objects and objects previously detected in spectroscopic studies of A1689. The shaded region indicates the redshift range of the cluster,* $0.159 < z < 0.22$*. The solid vertical line at* $z = 0.187$ *indicates the mean cluster redshift, and the dashed vertical line indicates the mean of the grism sample at* $z = 0.195$*.*

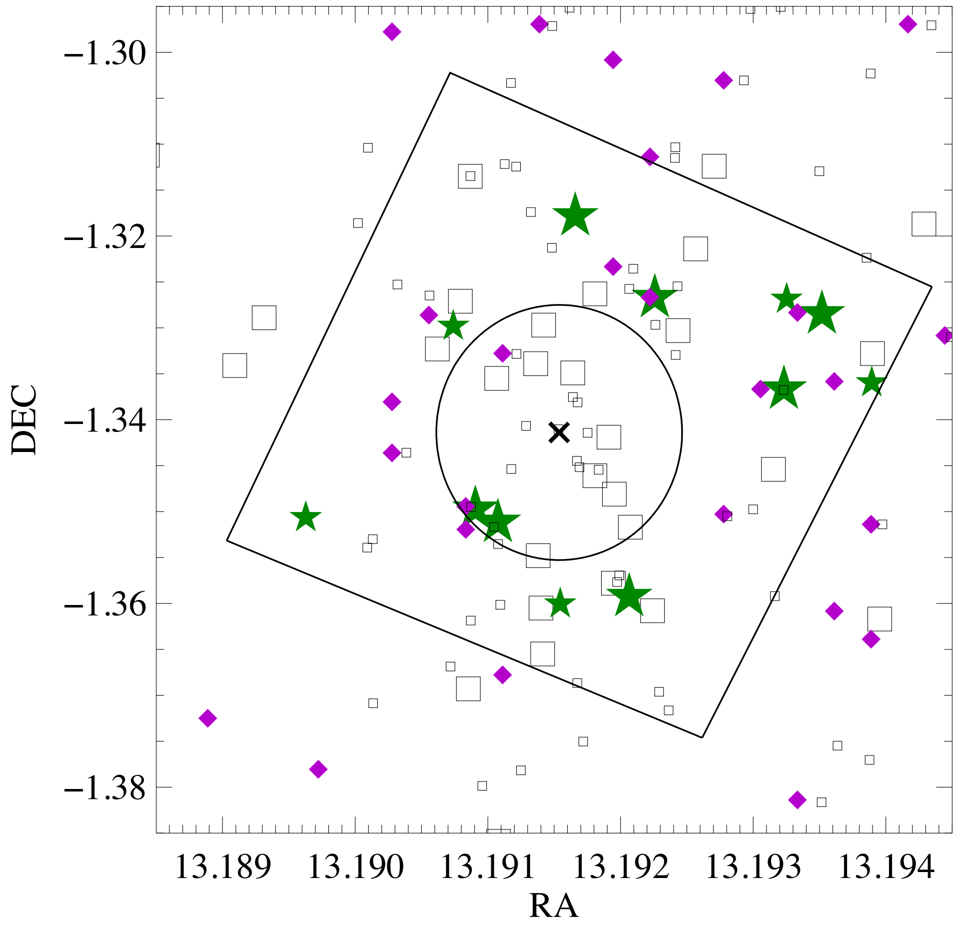

Figure 6.3: *Scatter plot showing the cluster field and the location of Hα-emitters in the redshift range 0.159 < z <0.22. The box shows the HST ACS field of view. "×" marks the cluster centre at RA, Dec = -13.1915, -01.3414. The circle indicates the location of a 50″Einstein ring relative to the centre. The larger open squares are all galaxies in this redshift range with spectroscopic detections from the catalogues of Frye et al. (2007), Mieske et al. (2005) and Teague et al. (1990). The smaller open squares are objects from the catalog of Duc et al. (2002) and the filled purple diamonds are Hα-emitters listed in Balogh et al. (2002). The green stars show Hα-emitters detected in the grism sample. The smaller stars are objects with log(F(Hα)) < -16.0, and the larger stars are those with log(F(Hα)) ≥ -16.0.*

A1689, finding it to be lower than that of the field by a factor of ~ 5. We estimate the SFR of the cluster members in this sample using the relationship between Hα luminosity and star formation rate given by Kennicutt (1998) including 1 mag of dust extinction: $\mathrm{SFR}_{H\alpha}(M_\odot \mathrm{yr}^{-1}) = 2.0 \times 10^{-41} \mathrm{L(H}\alpha\mathrm{)(ergs\ s}^{-1})$. One of the H$\alpha$-emitting ELGs is a bright spiral galaxy (#1157 in the table, seen at the top left of the colour image in Figure 6.6)[1] which has a high $\mathrm{SFR}_{H\alpha}$ of 3.29 $M_\odot \mathrm{yr}^{-1}$, placing it at the bright end of the luminosity function shown in Figure 11 of Balogh et al. (2002), while the rest of the ELGs have $0.05 < \mathrm{SFR}\ (M_\odot \mathrm{yr}^{-1}) < 0.46$, populating the faint end of the LF.

Rest frame absolute B-band magnitudes M_B (AB magnitudes) were obtained by fitting a Bruzual-Charlot model to the observed photometric points, and computing the conversion to the rest frame Johnson *B*-band including a *k*-correction term. Figure 6.4 shows values for rest frame M_B as histograms for each of the three most common emission line species-Hα, [O III] and [O II]. In order to study the effect of cluster lensing on a grism survey, we compare this sample with a grism survey of a similar depth carried out in the Hubble Deep Field North (HDF-N) by Meurer et al. (2007, henceforth M07). The black continuous histogram in the bottom row of each panel represents the A1689 sample, while the upper grey continuous histogram represents this HDF-N sample (offset by 14 for clarity). The most striking point here is the fainter median value for M_B for the [O III] emitters, indicating that for the A1689 sample, one can see further down the luminosity function due to the gravitational lensing effect. This is not seen in Hα as this sample is dominated by cluster member galaxies. The same effect is not seen for [O II]; the reason is not clear but may be due to the small size of the sample, 20 galaxies are [O III] emitters, while only 7 show [O II] emission. The median rest equivalent widths for the sample are as follows: $\mathrm{REW}_{H\alpha} = 29.3$Å, $\mathrm{REW}_{[OIII]} = 67.2$Å and [O II] = 29.6Å. These values are high, but typical of grism surveys. For all species, the REW values are lower than the median values in the HDF-N. This is consistent with a lensing effect, in that fainter objects from the lower end of the luminosity function which are only visible due to lensing will have lower REWs, resulting in a net downward shift in the median REWs.

---

[1] Object #1157 shows He I λ4472, which is a strong indicator of AGN activity

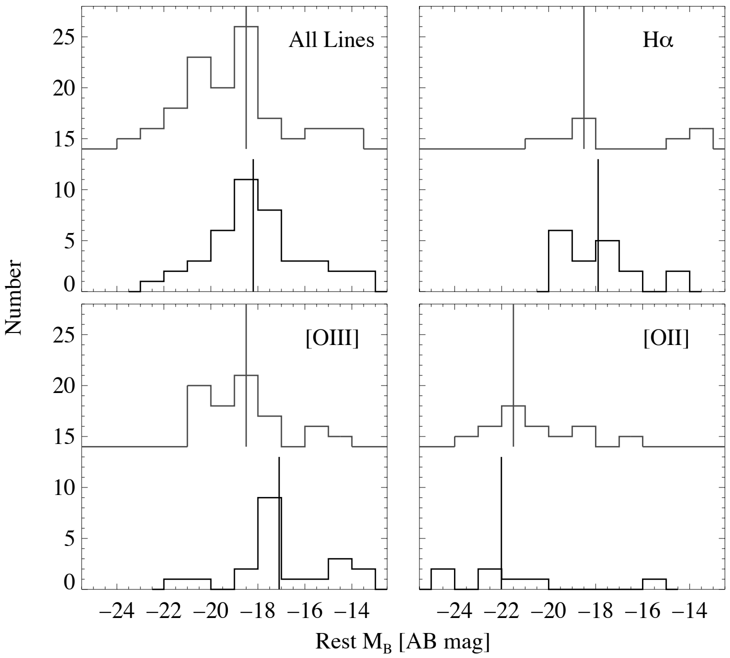

Figure 6.4: *Histograms showing absolute magnitude distribution for grism-detected objects in A1689 and HDF-N. The HDF-N sample has been offset by 14 for clarity*

One of the objects in Table 6.1, #6621, has a single emission line at 6712Å. This object lay in a favourable location to be observed simultaneously in a multi-slit mask during the Magellan observations described in Section 3.1.3. The resulting spectrum is shown in Figure 6.5. The emission line detected at 6712Å in the grism observations is not evident in these data, which reveal the object to be a cluster member with a redshift of $z = 0.1868$. The redshift is based on the detection of the Hα line, the [N II] $\lambda\lambda$6548,6583 and [Si II] $\lambda\lambda$6716,6730 doublets, and NaD absorption (not shown). This region of the sky from the HST image is also shown in Figure 6.5, with the position of the $1''.0$ wide Magellan slit overlaid, and the location of the 6712Å emission line circled. We designate this object 6621*a*, and while it is not included in Table 6.1, it is included in the scatter plot of Hα-emitting cluster members, Figure 6.3. The source of the emission line detected by the grism is unclear, but cautiously take it to be the projection on the sky of an arclet with $z = 0.800$, with the emission line being due to [O II] λ3727.

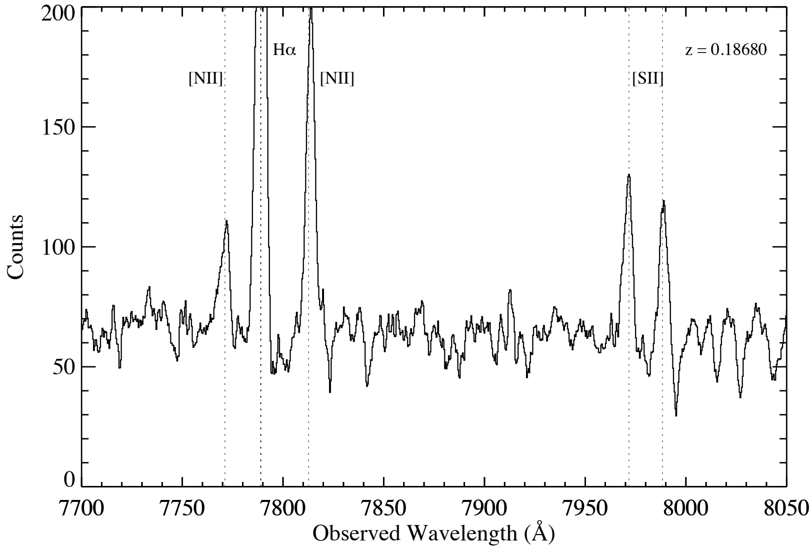

(a) Magellan spectrum of 6621a at $z = 0.1868$

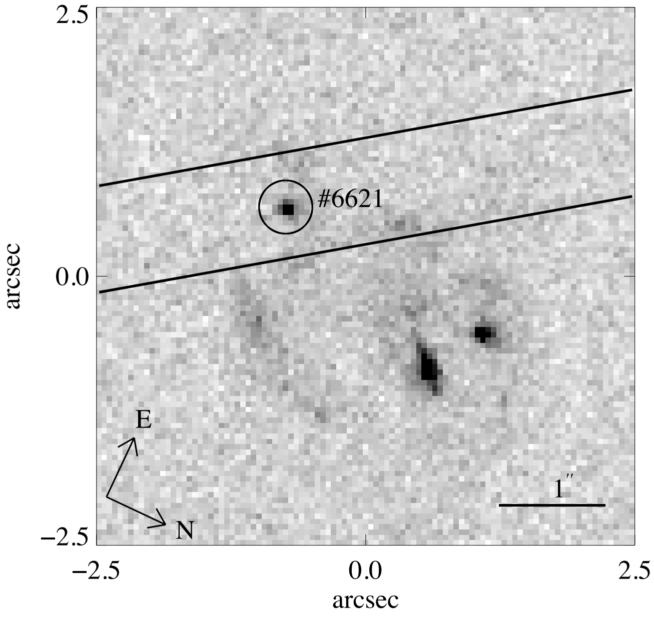

(b) Section of HST i_{775} image around 6621a

Figure 6.5: *Magellan spectrum and HST image of serendipitously-discovered cluster member #6621a at* $z = 0.1868$. *The circle in the HST image represents the location of the line emission in the grism data.*

6.3 Arclet at $z = 5.13$

The highest redshift object in the sample is the extremely small red arclet shown in the inset of Figure 6.6, with other known objects in the near-field marked. The grism spectrum is shown as the upper spectrum in the lower panel. The lone emission line can be securely identified as Lyα, as this galaxy has a previously known redshift of $z = 5.13$ from Frye et al. (2002). The Keck Low Resolution Imaging Spectrometer (LRIS) spectrum from Frye et al. (2002) is shown as the bottom spectrum in the lower panel of Figure 6.6, with the Lyα line observed at the same wavelength as in the grism spectrum. The small angular size of distant galaxies in slitless spectroscopy is beneficial, because a larger spatial extent tends to give a wide line-spread function, resulting in a blurred line width. The GRAPES survey (Pirzkal et al. 2004) and the PEARS survey (Malhotra and PEARS collaboration 2007) are grism slitless studies in the Hubble Ultra Deep Field (HUDF) using the same G800L grism on the HST ACS as the present sample. The GRAPES and PEARS surveys are able to target high-redshift Lyα-emitting galaxies such as this one without preselection for a Lyman break. From these two surveys, Rhoads et al. (2009) find that of their sample of photometrically pre-selected Lyman-break galaxy (LBGs, see Chapter 8) candidates, $\sim 25\%$ are Lyα-emitters. The $z = 5.13$ galaxy detected in this sample would satisfy the criterion of Rhoads et al. (2009) for photometric pre-selection with $(V - i) = 3.23$ and $(i - z) = 0.1$, which in the absence of the previous Keck LRIS spectrum would help to identify the lone emission line as Lyα. The estimated lensing for this galaxy is a factor of ~ 4.5.

Further grism studies in the fields of lensing clusters in combination with photometric studies in two or more filters could be an observationally-efficient method of searching for objects at $z \sim 5$. This method has proven effective in the Hubble Ultra Deep Field, with Pirzkal et al. (2007) presenting the grism spectra of nine Lyα-emitting galaxies with $4.0 < z < 5.7$. These Lyα lines are differentiated from [O II]λ3727 and a 4000Å-break with the photometry-these authors require the break amplitude to be at least a factor of 15, which is much greater than can be observed in a 4000Å-break. This method could in theory be utilised in other clusters as a relatively quick method to search for multiple images of high-redshift objects which could be used in cluster-mass modelling, as well as high S/N follow up spectroscopic studies to increase the sample of

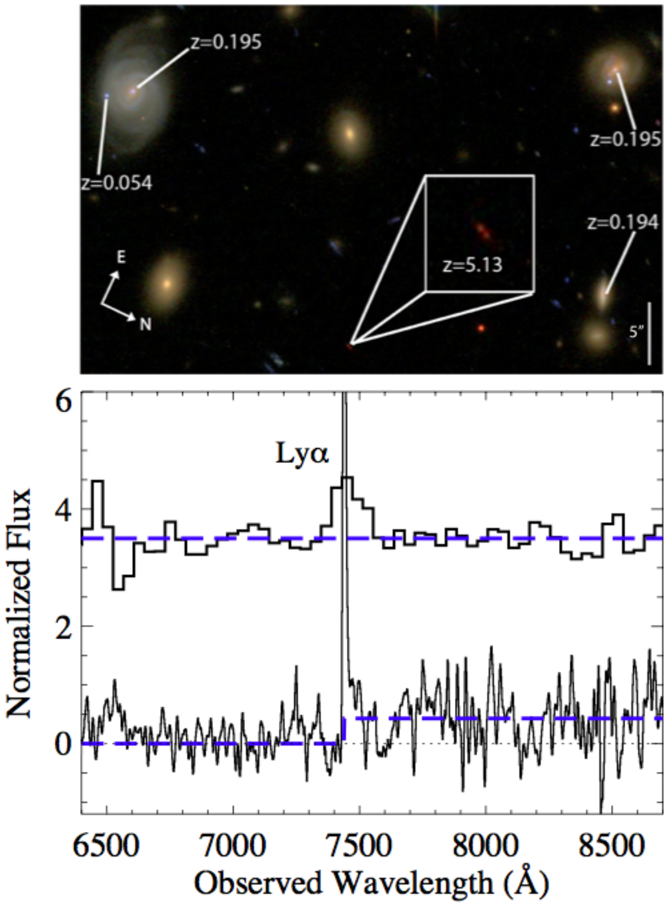

Figure 6.6: *Colour image and spectra of* $z = 5.13$ *galaxy. The upper spectrum is from this grism survey, while the lower is the Keck LRIS spectrum from Frye et al. (2002)*

objects similar to A1689-7.1 described in Chapter 5.

6.4 Spatially Resolved Nebular Emission

One of the prime advantages of grism spectroscopy over other observing techniques is the high spatial resolution of $\sim 0\farcs21$ in one dimension, enabling spectroscopy of separate sources of nebular line emission within the same galaxy to be resolved. Galaxies with multiple emission are outlined in Table 6.2. Within the galaxy cluster, we find 4 galaxies with multiple emission. The most interesting case is a cluster member at $z = 0.165$ with two emission line sources labelled #20004 and #11085. The image and spectra of the two emitting line regions are shown in Figure 6.7. The spectrum of ELS #11085 (B in Figure 6.7) shows a single emission line with a red tail, which we identify as Hα at a redshift of $z = 0.165$, while ELS #20004 (A) shows two emission lines, consistent with both being due to Hα at a mean redshift of $z = 0.165$, connected to the same source as B. The double peaked profile of A does not have a wavelength separation that could be explained by any other line combination (e.g. [O III] /Hβ). The inset of Figure 6.7 (a) from the HST i_{775} image shows a nucleus which is the source of the emission in B, while ELS A appears to be at a distinct location to the east of B. Based on the combination of the image and spectral profiles, we infer that this system likely comprises two Hα-emitting nuclei closely separated in space. The sources have a separation of $0\farcs21$ which corresponds to 0.65 kpc in the source.

As well as spatially resolved emission in cluster members, multiple nebular emission sources are also detected in three background galaxies. One notable case is an extended arc which has a previous spectroscopic redshift of $z = 0.7900$ (Duc et al. 2002), which contains three emission line sources: #20002 (A), #10638 (B) and #10640 (C). Each of these ELSs contains two emission lines, [O II] and [O III], while Hβ is resolved in one of the sources (B), indicating three distinct locations of star formation. A cutout of the HST i_{775} image showing the arc, and the 3 grism spectra are shown in Figure 6.8. Multiple bright knots are resolved in the i_{775} image. The three ELSs are closely separated in space, with an angular separation of $0\farcs927$ between knots A and B, while B and C are separated by $0\farcs27$. The magnification of this system is estimated to be varying between 4 and 5 across the arc (see Figure 3.5),

Table 6.2. Emission Line Galaxies with Multiple Emission Line Sources

Group	ID	z$_{ELS}$	θ^{a}
1	10782	0.153	
	3203	0.170	
2	20004	0.165	0
	11085	0.165	0.177
3	4971	0.205	0
	4752	0.210	
	11040	0.210	
4[b]	4298	0.209	0
	4251	0.210	
5	6583	0.590	0
	6578	0.590	
6	11149	0.629	
	5570	0.637	
7	10638 “B”	0.815	0
	20002 “A”	0.790	0.93
	10640 “C”	0.785	0.27

[a] Angular Separation in arcsec with respect to the first ELS in its group.

[b] This set of ELSs has an additional ELS projected near to the line of sight but with different colours. It is: #4277 at z$_{grism}$ = 0.46.

so these projected separations result in values of 1.5 kpc between A and B, and 0.5 kpc between B and C in the source plane after correction for magnification. The FWHM values are measured from the fits to the lines shown in Figure 6.8 (b), and these values are given in Table 6.3. The multiple locations of star formation with large velocity separations between the sources and varying line profiles indicate large scale gas motions and variation across the extent of the galaxy. The magnification due to lensing makes this galaxy an ideal target for further in-depth study of the properties of a single star-forming galaxy at $z \sim 1$. Companion higher resolution spectroscopy was obtained (see Chapter 3) and this galaxy is studied in detail in Chapter 7.

Table 6.3. FWHM of Emission Lines in Extended Arc at $z = 0.79$

Source ID	FWHM [O III] Å	FWHM [O II] Å	FWHM Hβ Å
20002 (A)	192.4	146.6	···
10638 (B)	159.3	187.1	199.9
10640 (C)	90.0	178.1	···

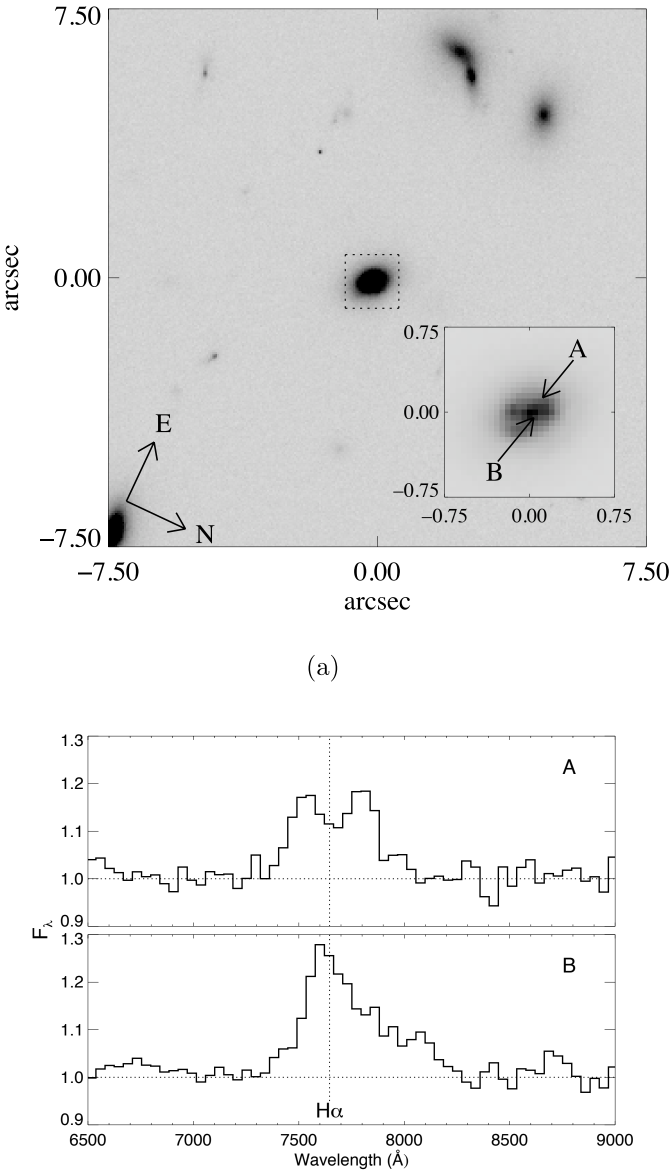

(a)

(b)

Figure 6.7: *Portion of the HST* i_{775} *image around the galaxy which host emission line sources #20004 (A) and #11085 (B), with the inset showing a close-up of the galaxy. The emission comes from two distinct regions within the galaxy. Panel (b) shows the resulting spectrum from the grism data. Source (A) displays two distinct emission peaks, with the central wavelength of the two consistent with the location of Hα at a redshift of* $z = 0.165$*, as is seen in Source (B). This would indicate some motion in the galaxy between the two sources, which are separated by only 0.65 physical kiloparsecs.*

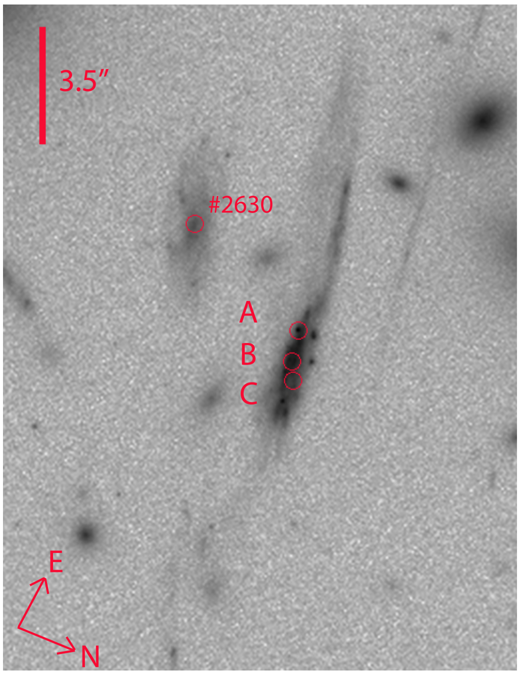

(a) HST ACS i_{775} image

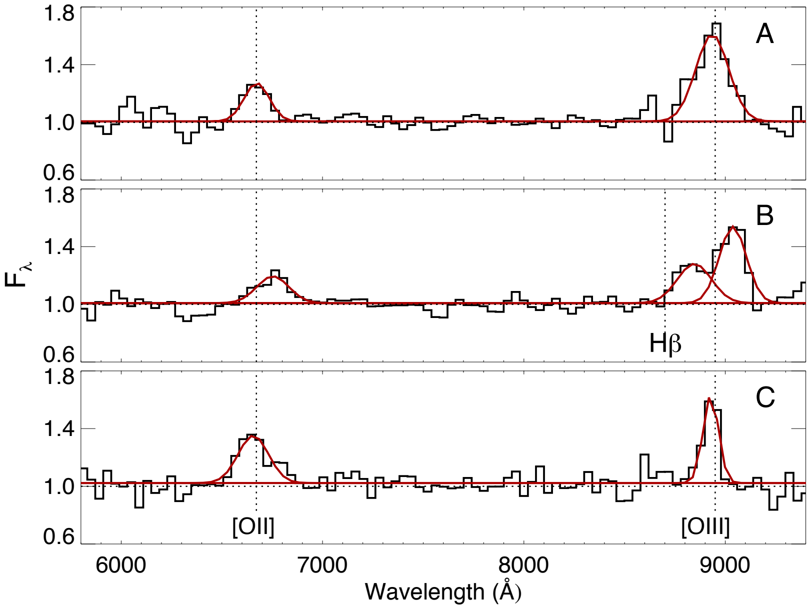

(b) Grism spectra with fits to the emission lines overlaid

Figure 6.8: *The upper panel shows a HST ACS Wide Field Camera i_{775} image of the bright arc at z=0.7900, with corresponding spectra from the HST G800L grism in the lower panel. This galaxy contains three individual emission line sources, #20002 (A), #10640 (B), and #10638(C). Each of the sources displays the [O II]λ3727 line and the [O III]λλ 4959, 5007 doublet (blended at this resolution). Hβ can also be resolved in source B. The vertical dotted lines indicate the location of the [O II], [O III], and Hβ emission lines at the systematic redshift of z=0.7900 from Duc et al. (2002). A large relative gas motion is apparent between component B and components A and C. This motion is measured to be $\Delta v = 3600 \pm 1700$ Km s^{-1}. This galaxy is discussed further in Chapter 7.*

7

Detailed Spectroscopic Analysis of a Strongly Lensed Galaxy at $z = 0.79$

In this Chapter I focus on the analysis of the spectrum of a bright (M$_B$ = -21.3) strongly lensed galaxy at $z = 0.79$. While many samples of galaxies at $z \sim 1$ are available, few studies probe the individual characteristics of single galaxies at this important epoch in galaxy evolution. With the magnification afforded by gravitational lensing by the massive cluster A1689, I have carried out a detailed study of such an object. The galaxy was initially identified in the grism survey of A1689 to have 3 spatially resolved emission-line regions, each showing strong [O II]λ3727 and [O III]$\lambda\lambda$4959,5007 spectral lines. Imaging data reveals a compact central region with an arc-like extention. The HST image of the galaxy along the with the grism spectra and their relative locations are shown in Figure 6.8. The observations made with the Keck and Magellan telescopes are outlined in Chapter 3 and the data reduction is outlined in Chapter 4. This galaxy was previously observed by Duc et al. (2002), who report a redshift of $z = 0.790$. As shown in Figure 3.5, the estimated magnification due to lensing is a factor of 4 to 5, varying along the arc. The lower limit of 4 is adopted in this work.

7.1 Galaxy Properties

The spectrum shows the recombination lines of the hydrogen Balmer series detected down to H9 as shown in Figure 7.1. Collisionally excited lines of oxygen and neon are detected: [O III] at rest wavelength $\lambda\lambda$4959,5007; resolved [O II] at rest wavelength $\lambda\lambda$3726.1,3728.8 (Figure 7.4), as well as [Ne III] λ3869. The systemic redshift is determined by simultaneous Gaussian fits to both components of the doublets of both the [O II] and [O III] lines, and is determined to be $z = 0.7895$. The line width is estimated from the fit to the [O III] λ5007 line, and is found to be $\Delta v = 500$ km s^{-1}. After subtraction of the instrumental resolution of $\Delta v = 51$ km s^{-1} in quadrature, this value is reduced to $\Delta v = 497.4$ km s^{-1}. This redshift and line width is imposed on all other lines, including the individual lines of the [O II]λ3727 doublet. There is low-level skyline contamination of the [O III] λ5007 line, and in order to avoid any reduction in the flux caused by this, the flux value is taken from the Gaussian fit rather than the data values. The λ4959 line suffers more significant contamination from nearby skylines. The ratio of [O III] λ5007 to [O III]λ4959 is well defined as 3:1 (see e.g. Storey and Zeippen (2000)), and so for any calculations involving the sum of the fluxes or equivalent widths of these two lines, this ratio is used in combination with the value of the [O III] λ5007 line. For the other lines, the values are taken from the data.

The one-dimensional velocity dispersion σ is a measure of the dynamics of gas which is bound by gravity to the galaxy. The line width of the Hβ line was used to estimate σ, as it is not affected by skylines and is a single line rather than a blend. σ was estimated from the FWHM of the line after subtraction of the instrumental resolution in quadrature, and is found to be 55 km s^{-1}. For a sample of 19 $z \sim 3$ LBGs, Pettini et al. (2001) use the velocity dispersion in combination with the half-light radius to determine the virial mass using the following equation for an idealised case of a uniform density sphere:

$$M_{vir} = 1.2 \times 10^{10} M_{\odot} \frac{\sigma^2}{100\text{km s}^{-1}} \frac{r_{1/2}}{kpc} \tag{7.1}$$

In order to make an estimate of the half-light radius $r_{1/2}$, it is necessary to make an estimate of the intrinsic size of the galaxy. Figure 7.2 is an image of the galaxy after inversion back to the source plane using the same lensing model for which magnification contours are shown in Figure 3.5, courtesy of collaborator Dr. Keren Sharon. A rough estimate of the half light radius from this image would give a value of $0''.5$, if the full diameter is contained only in the bright central portion and does not include the extending "tail". The area of the galaxy can be estimated from the HST ACS images such as the one shown in Figure 6.8. In order to do this, I wrote an IDL code to estimate the number of pixels contained within the galaxy, and converted to area using the ACS pixel scale of 0.05 arcseconds per pixel. This gives an observed area

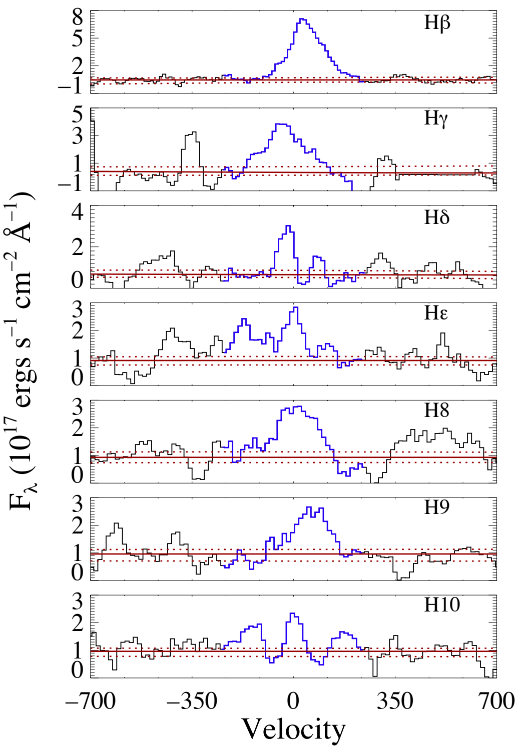

Figure 7.1: *Balmer series emission as observed in the Keck spectrum. The best fit SED model has been subtracted to correct for underlying stellar absorption. The best fit continuum and upper and lower levels are also shown. The velocity width of the line shown in blue is -250 km s*$^{-1}$$<$ *v* $<$ *+250 km s*$^{-1}$ *at the systemic redshift for these observations of* $z = 0.7895$. *The highest order line for which a reliable detection is made is H9, however, H10 is included to show the end of the sequence.*

of 4.0 arcsec^2, resulting in a half-light radius of $0\farcs4$ - $0\farcs5$ in the source plane. Using these values for $r_{1/2}$ in Equation 7.1 along with σ = 55 km s^{-1} gives $M_{vir} = 1.22 \pm 0.14 \times 10^{10}$ $M_\odot$. This mass will reflect the mass of the gas in the ISM as well as stellar mass, and naturally is somewhat higher than the result found for the stellar mass by SED fitting in Section 7.2.3. The velocity dispersion and virial masses are very similar to the sample of LBGs shown by Pettini et al. (2001), which have an average velocity dispersion of $\sigma = 70$ km s^{-1} and an average virial mass of $M_{vir} = 1.3 \times 10^{10}$ $M_\odot$.

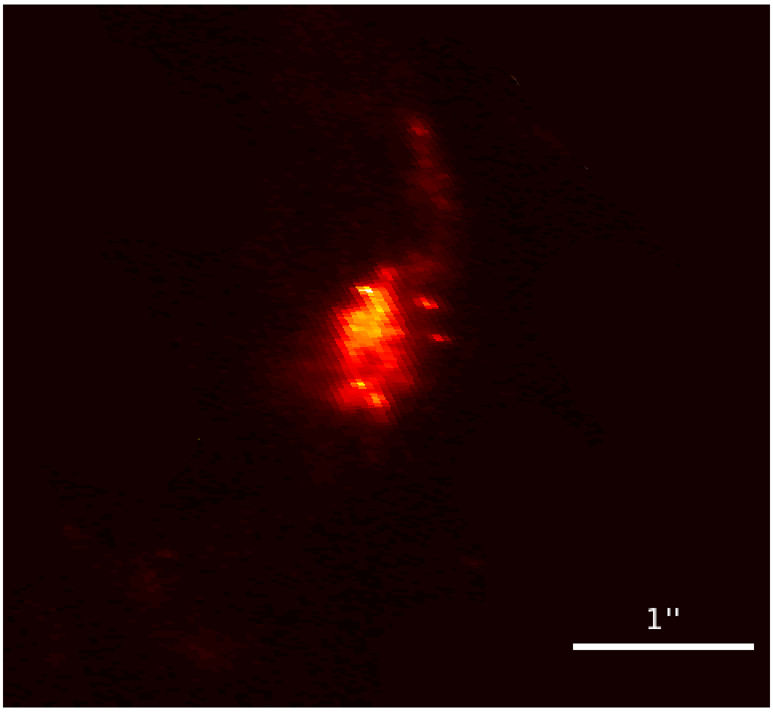

Figure 7.2: *Source plane image of* $z = 0.79$ *arc. The scale bar indicates* $1\farcs0$. *This image is courtesy of Dr. Keren Sharon.*

As described in Section 4.4, it was possible to extract 7 individual spectra across the spatial extent of the emitting region of the galaxy (the position of the individual slits is illustrated in Figure 7.11). Figure 7.3 shows the variation of the Hβ line across the extent of the emitting region, from the 7 individually extracted spectra. From bottom to top the spectra correspond to the slits in Figure 7.11, from the lowest point of the emitting region at -$2\farcs074$ to the highest at $2\farcs074$. The rest equivalent width (REW) of each line is given on the left hand side.[1]. The REW is measured relative to the true line centre, i.e. -250

---

[1] The individual spectra shown have not been corrected for underlying stellar absorption

km $\mathrm{s}^{-1}$to $+250$ km s^{-1}, with the zero velocity equivalent to the Hβ wavelength 4861Å$\times(1+z)$. There is a shift in the velocities of the line centroids, with a maximum velocity of $\Delta v = 38$ km s^{-1}, and a variation in the one-dimensional velocity dispersion of $\Delta\sigma = 44$ km s^{-1}. The location of the highest REW tells us where stars are building up the quickest with respect to the existing stellar populations. It is clear from the plot that the lowest REW is at the centre of the galaxy, which is an indicator of inside-out galaxy formation

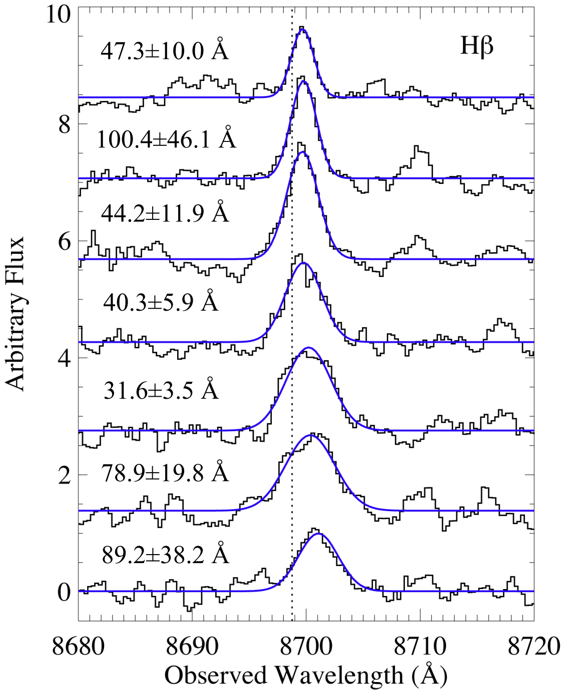

Figure 7.3: *The spectrum of the region around the Hβ emission line is plotted for each of the spectral slices shown in Figure 7.11, with the position in this plot matching the location on the galaxy within the slit. The fits to the lines were used to determine the central wavelengths. The dotted line represents the systemic redshift of the Hβ line, 4861Å$\times(1+z)$. The rest equivalent widths for each are given on the left hand side, which are seen to decrease toward the centre.*

Figure 7.4 shows the resolved [O II]$\lambda\lambda$ 3726.1,3728.8 doublet. Overlaid are the Gaussian fits to the lines which I carried out using the IDL library of least squares curve fitting, MPFIT (Markwardt 2009). At the temperatures which characterize star-forming regions, 10000-20000K, the ratio of the $\lambda\lambda$3726.1, 3728.8 lines is sensitive to collisional excitations and de-excitations, and hence

---

as explained in Section 7.3; however, we find in this section that the correction increases the REW of the Hβ line by 4.45Å and this value has been added to give the REWs reported in the plot

Table 7.1. Emission-Line Properties of $z = 0.79$ Galaxy

Line	Rest EW Å	Line Flux ergs s^{-1} cm^2
[O II]	128.58 ± 24.53	$2.87\pm 0.17\times10^{-15}$
[O III] $\lambda5007$[a]	77[b]	$2.38 \pm 0.21 \times10^{-15}$
[Ne III]	2.60 ± 1.1	$1.44 \pm 0.71\times10^{-16}$
Hβ	32.68 ± 2.63	$7.03 \pm 0.93 \times10^{-16}$
Hγ	18.58 ± 4.81	$2.88 \pm 1.15 \times10^{-16}$
Hδ	2.55 ± 1.29	$7.83 \pm 6.53 \times10^{-17}$
Hϵ	4.74 ± 1.13	$2.43 \pm 0.56 \times10^{-16}$

[a] As [O III]$\lambda4959$ is strongly affected by night sky lines, we adopt the standard assumption that [O III] $\lambda\lambda4959$, $5007 = 1.3 \times$ [O III]$\lambda5007$ when using ratios based on the flux or equivalent width of [O III] $\lambda\lambda4959$, 5007. The value for the flux is taken from the Gaussian fit to the [O III] $\lambda5007$ line.

[b] This value should be taken as a lower limit, as this is the value measured from the data including the skyline contamination

Table 7.2. Emission-Line Ratios of $z = 0.79$ Galaxy For Use in Diagnostic Diagrams

Diagnostic	Value	Reference
R_{23}	8.84 ± 1.82	Pagel et al. (1979); Nagao et al. (2006)
O_{32}	1.11 ± 0.16	Kobulnicky and Kewley (2004), McGaugh (1991)
[O III]$\lambda5007$/[O II]	0.84 ± 0.12	Nagao et al. (2006), Kewley and Dopita (2002)
[Ne III]/[O II]	0.05 ± 0.03	Nagao et al. (2006)
[O III]$\lambda5007$/Hβ	3.49 ± 0.77	Lamareille et al. (2009)
[O II]/Hβ	4.19 ± 0.8	Lamareille et al. (2009), Pérez-Montero et al. (2009)
[Ne III]/Hβ	0.22 ± 0.13	Pérez-Montero et al. (2009)

to the electron density N$_e$. The intensity of the two lines found by the fitting procedure was converted from intensity ratio $I_{\lambda3728.8}/I_{\lambda3726.1} = 1.435$ to $N_e = 983$ cm^{-3} using the IRAF/STSDAS task NEBULAR.TEMDEN (Shaw and Dufour 1995), assuming a nebular temperature of 10000K, reaching $N_e = 1279$ cm^{-3} if a temperature of 20000K is assumed. The value of $I_{\lambda3728.8}/I_{\lambda3726.1} = 1.435$ is close to the theoretical low-density limit of 1.5.

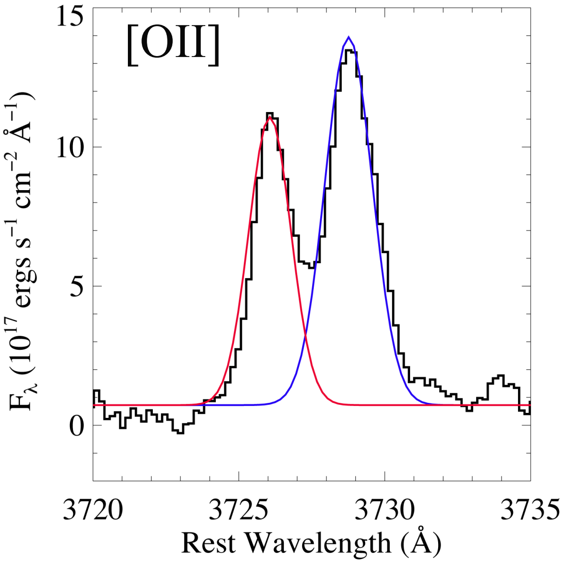

Figure 7.4: *Rest frame resolved [O II] λλ3726,3729 emission line from Keck observations with Gaussian fits to the lines overlaid. The ratio of the relative strengths of the two lines allow the calculation of the electron density* $N_e = 1131 \pm 148$ *cm*$^{-3}$.

Table 7.3. Photometry of $z = 0.79$ Galaxy

Telescope/Instrument	Filter	Apparent Magnitude (AB)
HST / ACS WFC	g'	21.0552 ± 0.08
HST / ACS WFC	r'	20.8697 ± 0.01
HST / ACSWFC	i'	20.5565 ± 0.01
HST /ACS WFC	z'	20.4370 ± 0.01
DuPont Telescope @ LasCampanas	U Johnson	21.0455 ± 0.16
Nordic Optical Telescope @ LaPalma	B NOT	21.2157 ± 0.17
Keck II / LRIS	V LRIS	21.0789 ± 0.15
Keck II / LRIS	I LRIS	20.4635 ± 0.12
Spitzer / IRAC	3.6μm	20.11 ± 0.07
Spitzer / IRAC	4.5μm	20.46 ± 0.08

7.2 Photometry and SED Fitting

SED fitting was carried out in the manner described in Section 5.3 using the population synthesis models of Bruzual and Charlot (2003, hereafter BC03), in conjunction with the photometric points presented in Table 7.3. As in Chapter 5, the observed values are corrected for the magnification due to lensing in order to find the intrinsic SED. The correction factor of 4 was applied, which results in a dimming of the observed photometric points by 1.5051 magnitudes. Due to the fact that $z = 0.79$ is a much later epoch than $z \sim 5$, many more complicated star formation histories are possible than just a single population and the results of the fitting procedure are less well constrained (Papovich et al. 2001). Thus the parameters derived from this type of modelling are subject to substantial systematic uncertainties. A number of these uncertainties can be reduced by observables from the complementary spectroscopic data.

7.2.1 Constraining the Age of the Dominant Stellar Population

In order to constrain the age range and minimize the parameter space which must be explored in the fitting procedure, the 4000Å break strength measured from the Keck spectrum can be utilised. The 4000Å break is a useful spectral indicator of the age of a galaxy. A strong 4000Å break occurs in older galaxies due to the buildup of a large number of absorption lines due to mainly ionised metals. The opacity in these high-ionised metal lines increases with decreasing temperature, and so the break amplitude is smallest for spectra dominated by young, hot stars, and reaches a maximum for old, metal-rich stellar populations. Bruzual (1983) defined a break index D(4000) as the ratio of the average flux density in the band 4050-4250Å to that in the 3750-3950Å band. In order to decrease the sensitivity to reddening effects, a break index $\mathrm{D}_n(4000)$ based on narrower continuum bands was defined by Balogh et al. (1999) using the bands 4000-4100Å and 3850-3950Å. This $\mathrm{D}_n(4000)$ is preferred by Kauffmann et al. (2003b) in their comprehensive study of 10^5 SDSS galaxies, in which they use the 4000Å break as a key component to study star formation histories. The measurement of the 4000Å break strength is somewhat complicated by the presence of the [Ne III]λ3869 and H8 λ3889 lines in the Keck spectrum of the $z = 0.79$ galaxy, but after masking out the contribution from these, the break strength is measured as: $\mathrm{D}_n(4000) \sim 0.996$. The BC03 code provides the model value of $\mathrm{D}_n(4000)$ at every age for a given star formation history. The values of $\mathrm{D}_n(4000)$ are plotted against the age in the upper panel of Figure 7.5 for a solar metallicity ($Z_\odot$) model based on an instaneous burst (SSP), and for $Z_\odot$ models with τ =1 and 5 Gyrs. The variation between $Z_\odot$ and for $Z = 0.4Z_\odot$ for the best-fitting value of $\tau = 5$ Gyrs is shown in the lower panel. Given the potential errors due to incorrect removal of the contaminating [Ne III]λ3869 and H8 λ3889 lines, and the slow variation of $\mathrm{D}_n(4000)$ with age as seen in Figure 7.5, a conservative estimate of 6 Myrs $\lesssim$ t $\lesssim$ 100 Myrs is made for the age range of the galaxy. It is important to note however that any contribution from AGN continuum light would cause the amplitude of the 4000Å break to decrease, and hence cause an underestimate in the age of the galaxy (Kauffmann et al. 2003a). As outlined in Section 7.5, there is a distinct possibility that this galaxy may harbour some AGN activity.

7.2.2 Constraining the Metallicity

The BC03 suite provides models with metallicities of $0.005Z_\odot$, $0.02Z_\odot$, $0.2Z_\odot$, $0.4Z_\odot$, $Z_\odot$ and $2.5Z_\odot$. The oxygen abundance of the galaxy can be estimated from strong emission lines in the spectrum as outlined in Section 7.6, resulting in a value of $12 + \log(\mathrm{O/H}) \approx 8.5$. Kobulnicky and Kewley (2004) give the relationship between metal mass fraction and oxygen abundance $12 + \log(\mathrm{O/H})$

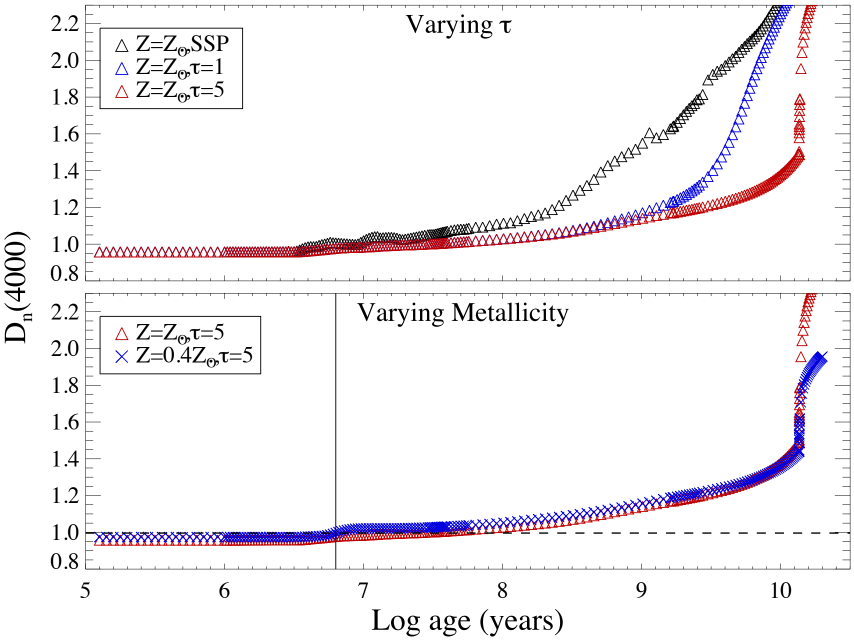

Figure 7.5: *Plot of D_n(4000) vs age from Bruzual-Charlot stellar population models. The upper panel shows the variation with τ for a fixed metallicity ($Z = Z_\odot$). The bottom panel shows the variation between solar metallicity $Z_\odot$ and the next lowest metallicity available in the BC03 models, $Z = 0.4Z_\odot$, which was found to provide the best fit to the observed photometry. The vertical bar corresponds to age = 6.3 Myrs, the age at which the theoretical models for $Z = 0.4Z_\odot$ reach the measured value of D_n(4000) = 0.996.*

as

$$Z \simeq 29 \times 10^{[12+log(o/h)]-12} \tag{7.2}$$

For 12 + log(O/H)≈ 8.5, we have $Z \simeq 0.6Z_\odot$. This estimate allows us to rule out the two lowest extremely metal-poor models, and also the highest-metallicity model.

7.2.3 SED Fitting: Results

In order to find the best-fitting SED model, an IDL code was written to take a fixed e-folding time τ, age t, and metallicity Z, and to cycle through a large array of values for the mass and dust and to return the best-fitting parameters. The E(B-V) values explored were 0 - 0.7 in steps of 0.05. The mass range explored was 10^8 - $10^{10}M_\odot$in steps of 0.5 $\times 10^8 M_\odot$. This mass range was tested in each run to ensure that the best-fitting model was never at the upper or lower end of the range, but in all cases, the best fit mass was always around the middle of this range at a few times$10^9 M_\odot$. For this fitting procedure, a Chabrier (2003) initial mass function (IMF) was again used. A population resulting from a single initial burst (simple stellar population; SSP) was ruled out due to a poor fit to the observed photometry. A scenario of exponentially declining star formation gives formally the best fit. A large e-folding time τ of 5 Gyrs was required here, and there is very little difference between exponentially-decaying star formation with this large value of τ and a constant rate of star formation. The fixed parameters are those which are limited by the models to have discrete values and so can only be varied in fixed steps. Mass and dust are the two parameters which affect the resulting fit most strongly and due to degeneracy between the two, a wide range of combinations of these values must be explored. The fixed values were varied systematically and for each set of τ, t and Z, the minimum χ^2, mass and dust values were recorded for each combination until an overall minimum value of χ^2 was converged upon. Given more computing power, this code could be extended to be fully automated, looping through all the options. Further work would include introducing the Salpeter (1955) IMF to explore whether varying IMF can strongly affect the result. Another aspect of the fitting procedure which must be implemented for future work is to introduce a method to build a multi-component model, which will allow for an underlying continuous population in combination with short duration bursts of star formation, as described in Salim et al. (2007). Lamareille et al. (2009) state that models without secondary bursts fail to reproduce the underlying old stellar population which affects the colours of the redder bands, and can lead to an underestimate of the stellar mass by a factor ~ 1.4, and so the mass determined for the galaxy from this fitting procedure should be considered representative of a lower limit.

The best fit model gives a value for the dust of $E(B\text{-}V)_* = 0.45$, a stellar mass of M_*=1.95 $\times 10^9 M_\odot$. An extremely young age of 8 Myrs is found, which is consistent with the range of ages inferred from $D_n(4000)$. The best fitting metallicity is found to be $Z = 0.4Z_\odot$, which is in keeping with the sub-solar metallicity found from the spectrum in Section 7.6. The best fit model is shown in Figure 7.6.

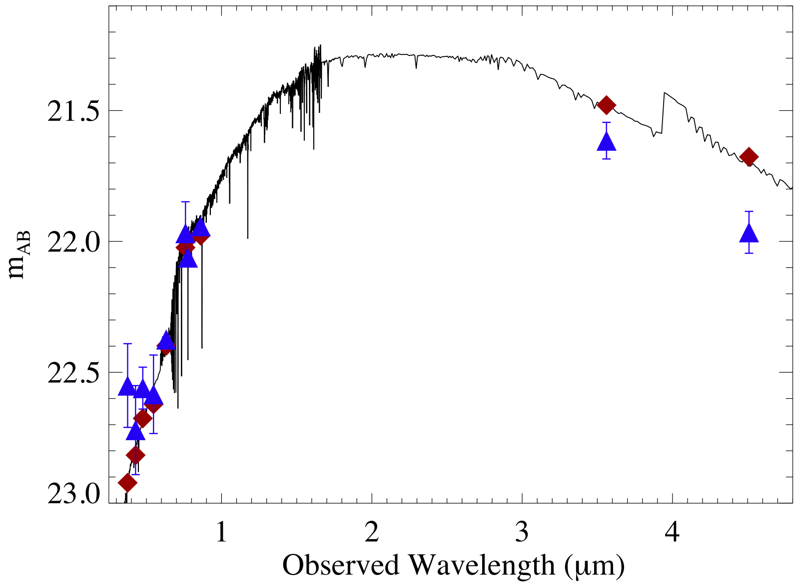

Figure 7.6: *Best fit SED model for* $z = 0.79$ *galaxy. The wavebands are (from left to right) U, B, g′, V, r′, I, i′, z′, 3.6μm and 4.5 μm. The red diamonds are the magnitudes generated from the SED, while the blue triangles with error bars are the observed photometric points, corrected for a magnification factor of 4. This model has* $E(B\text{-}V)_* = 0.45$, $M_* = 1.95 \times 10^9 M_\odot$, $Z = 0.4 Z_\odot$, $\tau = 5$ *Gyr and* $t = 8$ *Myr.*

7.3 Correction for Underlying Stellar Absorption

Spectra of the massive O, B and A stars which dominate starburst and star-forming galaxies are characterised by strong hydrogen Balmer and neutral helium absorption lines. These absorption lines are coincident with the nebular emission lines from interstellar gas which has been ionised due to the absorption of ionising photons from these stars. In many cases, the higher order Balmer series stellar absorption lines and some of the HeI absorption lines can be detected as absorption wings superposed on the emission line spectra of starburst galaxies. The fact that the absorption begins to dominate at higher orders is due to the fact that Balmer emission decreases rapidly with decreasing wavelength, while the equivalent width of the stellar absorption lines is constant or increases with wavelength. The effect of the underlying absorption is a reduction in the equivalent width of the emission line. Numerous authors have addressed this issue in studies which require accurate Balmer emission line measurements. Some authors apply a correction to the rest frame equivalent width of Hβ independently of galaxy properties: Kennicutt (1992) add 5Å, while Kobulnicky and Phillips (2003) add a more modest 2Å. This blind approach warrants caution, as the extent of the effect of stellar absorption varies greatly with the age of the dominant stellar population. Tremonti et al. (2004, hereafter T04) use a more robust approach, which is to find the best-fitting stellar population model template to the galaxy spectrum. The SED models are based on stellar populations and so display stellar absorption features at the Balmer wavelength but no emission. This model can then be subtracted from the observed spectrum to leave the intrinsic Balmer emission. As we detect emission at the location of the Balmer lines all the way down to H9, it is clear that underlying stellar absorption is not a major problem for this galaxy. Given the low age implied by the 4000Å break and the SED model fitting, this is in keeping with the results of González Delgado et al. (1999) who show that the strength of the Balmer absorption lines increase with evolution up to 500Myr. Using our best-fit model, we transform the best fit SED to the appropriate redshift and velocity dispersion and follow the T04 approach, finding that the correction increases the rest equivalent width of the Hβ line by 4.45Å. All values for Balmer lines given in this chapter include this correction for underlying absorption.

7.4 Reddening Correction

The amount of dust particles present in the interstellar medium is non-uniform, varying from galaxy to galaxy. Observational data from any galaxy must be corrected for the estimated effect of dust on the intrinsic light emitted from the galaxy. Interstellar extinction reduces the amount of light according to the equation: $I_{\lambda,int} = I_{\lambda,obs} e^{-\tau_\lambda}$ (Osterbrock 1989), where $I_{\lambda,int}$ is the intrinsic intensity of the source, $I_{\lambda,obs}$ is the intensity observed, and τ_λ is the optical depth at the wavelength observed. The optical depth is a function of wavelength, and so the intensity ratio of two lines λ_1 and λ_2 must be corrected for the variation in optical depth at the wavelength of each line as well as for the amount of dust present. The optical depth at each wavelength is calculated from a standard attenuation curve. The attenuation curve $k(\lambda)$ is related to $A(\lambda)$, the attenuation in magnitudes at wavelength λ, and E(B-V)$_*$, the colour excess of the stellar continuum by:

$$k(\lambda) = A(\lambda)/E(B-V)_*$$

For the Milky Way galaxy, the calculated ratio of total to selective extinction R_V ($R_V = A(V)/E(B-V)_*$) is given by Savage and Mathis (1979) as $R_V \approx 3.1$. For starburst galaxies and high redshift galaxies which we deal with in this work, the most suitable value of R_V is that of Calzetti et al. (2000): $R_V = 4.05 \pm 0.80$. As outlined in Section 5.3.2, the starburst extinction reddening curve $k(\lambda)$ of Calzetti et al. (2000) is given as:

$$\begin{aligned} k(\lambda) &= 2.659(-1.857 + 1.040/\lambda) + R_V, \\ &\qquad 0.63\mu m \leq \lambda \leq 2.20\mu m; \\ &= 2.659(-2.156 + 1.509/\lambda - 0.198/\lambda^2 + 0.011/\lambda^3) + R_V, \\ &\qquad 0.12\mu m \leq \lambda \leq 0.63\mu m \end{aligned} \tag{7.3}$$

The extinction caused by dust is strongly wavelength dependent, and can cause line flux ratios to deviate from their intrinsic values. This allows the amount of dust present to be calculated from a pair of optical emission lines with a well-defined intrinsic ratio from atomic theory. The relative ratios of Balmer lines can be used in this manner. As Hα is not available in this spectrum, we must use Hβ and one of the lower order Balmer lines-in this case Hγ is chosen. Any deviation in this ratio from the intrinsic value is attributed to dust extinction. The lines are first corrected for underlying stellar Balmer absorption (Section 7.3), and the observed flux ratio of Hβ/Hγ is $R_{obs} = 0.410$. Calzetti et al. (2000) gives the relationship between intrinsic flux $F_i(\lambda)$ and observed flux $F_o(\lambda)$ as:

$$F_i(\lambda) = F_o(\lambda)\ 10^{-0.4E(B-V)k(\lambda)} \tag{7.4}$$

Assuming Case B recombination, a nebular temperature of 10000K, electron density N$_e$ = 10^4 cm^{-3}, and the intrinsic value of Hγ/Hβ $R_{int} = 0.469$ given by Osterbrock (1989), we can calculate E(B-V)$_{gas}$ as:

$$E(B-V)_{gas} = \left[\frac{\log 10\,(R_{obs}/R_{int})}{-0.4\ (k(\lambda_{H\gamma}) - k(\lambda_{H\beta}))}\right] = 0.277 \tag{7.5}$$

Calzetti (2001) show that for local galaxies, the HII regions are more strongly attenuated than the stellar continuum by a factor of 2.272 (E(B-V)$_*$ = 0.44 E(B-V)$_{gas}$), most likely due to the fact that these are associated with sites of ongoing star formation. This would indicate that the value for the E(B-V)$_*$ = 0.45 found in the SED fitting process is an overestimate. As the dust value will be used to correct the emission lines from the HII regions in the forthcoming sections, we adopt the E(B-V)$_{gas}$ calculated from the Balmer decrement method as the most reliable estimate of the dust.

7.5 Spectral Classification

In order to classify this galaxy, one must distinguish the nature of the source responsible for the nebular emission lines, and determine whether the ionisation is purely caused by the massive stars powering star formation, or whether there is any contribution from an active galactic nucleus (AGN). A galaxy which hosts an AGN contains gas which is ionised by a hard source, and has the shape of a power law. The ionising photons in an AGN come from an accretion disk around a central massive black hole. The class of AGN which show narrow emission lines may further be broken down into Seyfert 2 galaxies and Low-ionisation Nuclear Emission Region galaxies (henceforth LINER galaxies, Heckman (1980)).[2] Seyfert 2 and LINERS can be distinguished on the basis of their [O III]/Hβ ratio: AGN with [O III]/H$\beta > 3.0$ are classified as Seyfert 2 (Ho et al. 1997). In a star-forming galaxy, the ionisation is due to ultraviolet photons from hot OB stars in HII regions, which ionise the surrounding gas, and give rise to emission lines in the spectrum of the galaxy. Composite galaxies also exist, which contain both star-forming regions and an AGN. In order to investigate the possibility of this galaxy harbouring an AGN, a number of emission-line diagnostic diagrams were used to compare the ratios of emission-line intensities. Spectral classification of emission line galaxies at low redshift can be determined from the position on emission-line diagnostic diagrams such as the well-known Baldwin-Philips-Terlevich (BPT) diagrams (Baldwin et al. 1981). These diagnostic diagrams are based on the idea that in a star-forming galaxy, emission lines result from photons emitted by massive stars, and atomic theory gives a well-defined upper limit on the intensities of the collisionally excited lines (e.g. [O II] or [O III]) relative to the recombination lines (e.g. Hydrogen Balmer lines). AGNs are powered by a source of far more energetic photons, making the collisionally excited lines more intense relative to the recombination lines. This allows values for such line ratios which would not be achievable in star-forming galaxies. The BPT diagrams are based on longer-wavelength emission-lines such as Hα or [N II], which are shifted out of

---

[2] Seyfert 1 galaxies are ignored in this case as they have broad Balmer lines with $\Delta v >$ 1000 km s^{-1}.

the optical passbands at redshifts $z \geq 0.4$. Classification systems based only on lines from the blue part of the spectrum have been proposed by numerous authors including Rola et al. (1997), Kewley et al. (2006) and Lamareille et al. (2004). Lamareille et al. (2009) presents results from the Vimos VLT Deep Survey (VVDS), which has a mean redshift of ~ 0.7. Their spectral classification is based on the equivalent width ratios [O II]/Hβ and [O III]λ5007/Hβ, and their Figure 4 is reproduced here in Figure 7.7. Using equivalent widths as a proxy for flux ratios is ideal when accurate dust extinction information is not available, or when fluxing cannot be carried out accurately as is the case for many large surveys. As we have reddening-corrected flux ratios available, we overplot these values for our galaxy on this plot. The solid line in Figure 7.7 is based on an empirical calibration of the boundary between AGN and star-forming galaxies from Lamareille et al. (2004). Galaxies above the curve are typically AGN, while star-forming galaxies are below it. The points within the dashed lines bounding the uncertainty region are classified as either star-forming candidates or AGN candidates depending on which side of the line they lie. Some authors refer to galaxies in this region as “SF/Sy2 composites”. It can be seen that while our galaxy may reside within the region populated solely by star-forming galaxies, it is also overlapping with the uncertainty region comprising galaxies that may be star-forming or may contain some contribution from a Seyfert 2 AGN, and so the possibility that this galaxy is a pure Seyfert 2 or is a SF/Sy2 composite containing some AGN component cannot be ruled out using this diagnostic tool. Pérez-Montero et al. (2009) use the ratios of [O II]λ3727/Hβ and [Ne III]λ3869/Hβ to separate star-forming galaxies from AGN. The galaxy again resides in a similar location in this diagnostic diagram; below the curve separating the AGN and star-forming galaxies but still within the uncertainty “composite” region. An argument against this galaxy hosting an AGN is the fact that there is no evidence in either the Keck or Magellan spectra for the presence of the HeIIλ4686 line or any other expected HeI or HeII lines which are often present in an AGN spectrum. Also, the stellar mass inferred from the SED fitting in Section 7.2 is $\mathrm{M}_* \simeq 1.95 \times 10^9 M_\odot$. While this mass is subject to uncertainties in the fitting procedure, it should be noted that Kauffmann et al. (2003a) find that very few AGN are found in galaxies with $\mathrm{M}_* < 10^{10} M_\odot$. Also, the Gaussian fit to the rest-frame [O III]λ5007 line gives a FWHM = 145 km s^{-1}. A recent study of a large sample of bright Type 2 AGN in the SDSS by Reyes et al. (2008) use FWHM

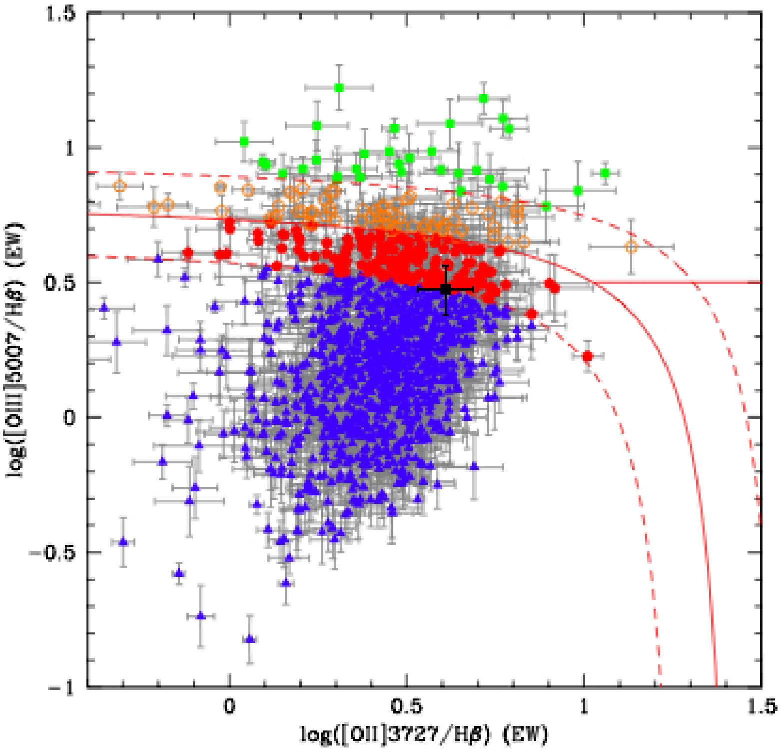

Figure 7.7: *Spectral classification diagnostic diagram reproduced from Lamareille et al. (2009). The galaxy at z= 0.79 is overplotted as a black square with associated error bars. The red curve is the empirical separation between star-forming and AGN galaxies taken from Lamareille et al. (2004), with the uncertainty regions marked with the dashed lines-in these regions star-forming and AGN galaxies are mixed as they show similar line ratios. The blue triangles indicate star-forming galaxies, candidate star-forming galaxies are shown as red pentagons, candidate AGN are open orange pentagons, and green squares are Seyfert 2 galaxies. Due to the location of the z= 0.79 galaxy on the border of the uncertainty region, the galaxy may be a star-forming galaxy, but could also have some contribution from an AGN.*

([O III]λ5007) $>$ 400 km s^{-1} as a criterion to define AGN activity where the diagnostic diagrams are inconclusive. In terms of this criterion, this galaxy would not be classified as an AGN; however it must be cautioned that theirs is a sample based on extremely luminous AGN and this criterion may not be applicable for a galaxy with considerably lower [O III]λ5007 flux such as this one. In conclusion, until further measurements in the near-infrared are made which can provide measurements for Hα, [N II] and [S II] allowing the use of the BPT diagram, the possibility of a Seyfert 2 AGN in this galaxy remains open.

7.6 Metallicity

The metallicity of a HII region is an important probe of the formation and evolution of a galaxy, and represents the integrated products of the star formation history. Stellar mass-loss processes disperse the metals formed in massive stars into the ISM. Oxygen makes a useful proxy for metallicity in studies of the ISM - it makes up about half of the metal content of the ISM, exists in multiple ionisation states giving rise to strong lines in the rest frame optical, and is only weakly depleted onto dust grains. Oxygen abundance is generally measured in units of 12 + log(O/H), where the ratio O/H is the abundance by number of oxygen relative to hydrogen. In this work, we take solar metallicity to be the value published in Allende Prieto et al. (2001), 12 + log(O/H) = 8.69. Ideally, the preferred method of oxygen abundance determination would be to use the “direct” T$_e$ method, wherein the abundance is measured directly from the ionic abundances obtained from a determination of the electron temperature of the galaxy. In local galaxies, this method can be applied using the strength of the [O III] λ4363Å line, which is sensitive to electron temperature. The electron temperature can be measured from the ratio of this line to to a lower excitation line such as [O III] λ5007. After correcting for unseen stages of ionisation, the metallicity can be estimated from the temperature. Using this T$_e$ method, however, is problematic, as [O III] λ4363Å is weak in very low metallicity galaxies, and is not visible in metal rich galaxies. At high redshift also this line generally becomes very weak. However, Yuan and Kewley (2009) have recently made a detection of the line in an extremely low-metallicity lensed galaxy at $z = 1.7$, which is promising for direct metallicity measurements at high redshift with the future generation of powerful large ground-based telescopes, and the James Webb Space Telescope (JWST). Problems can also arise with the T_e method if a temperature gradient exists in the HII region-this can lead to an overestimate of the true electron temperature, and hence an underestimate of the metallicity by up to as much as ~0.4 dex. In lieu of a direct measurement of the electron temperature, other methods have been described to estimate the metallicity. These are known as "strong-line" methods, as they rely on ratios of strong emission lines. A number of these ratios are used such as [N II]λ6584/Hα, [N II]λ6584/[O II], ([O II]/Hβ)/([N II]/Hα), ([N II]$\lambda\lambda$6717, 6731 + [SIII]$\lambda\lambda$9069, 9532) / Hβ, and the "R_{23}" ratio, ([O II]λ3727 + [O III]$\lambda\lambda$4959, 5007)/Hβ, introduced by Pagel et al. (1979). In order to use the strong-line ratio to determine the abundance, the relationship between the ratio and the abundance must be calibrated, and this has been carried out by a number of authors in the past three decades, leading to a large range of calibrations, none of which have proven as yet to be the absolute correct calibration. There are two distinct types of calibration, generally described as "empirical" or "theoretical". Empirical calibrations have been developed by fitting relationships between metallicities derived using the T_e method and the observed strong-line ratios in HII regions. This has been carried out for the [N II]λ6584/Hα and ([O II]/Hβ)/([N II]/Hα) ratios by Pettini and Pagel (2004), and for the R_{23} ratio by Pilyugin (2001) and improved upon by Pilyugin and Thuan (2005). As they are based on observations of the [O III]λ4363 line, these calibrations suffer the same potential problems as the direct method. Empirical calibrations suffer from a shortage of electron temperatures measured from metal-rich HII regions and hence the calibrations are only extrapolated to this regime, meaning they may be unsuitable. It is important to remember also that any empirical abundance method is limited by the fact that it is only directly applicable to star-forming galaxies or HII which span the same range of excitation and metallicity as the sample used to create the calibration, and as such may not be suitable at high redshift due to the lack of [O III] λ4363Å measurements. Looking to the future, the forthcoming NIRSpec (Near InfraRed Spectrograph) on the JWST will probe a full set of strong-lines from higher redshift galaxies, and hopefully detect the faint [O III] λ4363Å line in a significant sample, allowing a valid comparison between these ratios and the abundance calibrations made locally.

The other type of calibrations of strong-line ratios are "theoretical"; these are based on stellar population synthesis models combined with photoionisation models. The combination of the predicted SED with the photoionisation models allows one to predict the theoretical line ratios arising from different metallicities, and these predicted values are compared with observed line ratios. Calibrations carried out in this manner are numerous, and include those of McGaugh (1991, hereafter M91), Zaritsky et al. (1994), Charlot and Longhetti (2001), Kewley and Dopita (2002, hereafter KD02), T04 and Kobulnicky and Kewley (2004, hereafter KK04). While photoionisation model calibrations do not incur the problems associated with T_e measurement, they do have problems relating to the model handling of geometry, density distribution of dust and gas, and metal depletion. Differences of up to ~0.2 dex exists among the various theoretical calibrations because of these issues. There also exist large, poorly understood discrepancies between the theoretical and empirical calibrations, with the theoretical calibrations yielding metallicities which are up to a factor of 1.5 higher than the empirical (Kewley and Ellison 2008, hereafter KE08). A discussion on the topic by Moustakas et al. (2010) concludes that while in general empirical methods underestimate the true metallicity, there are hints that theoretical methods may overestimate the abundance somewhat, and that a compromise between the two may be the best approach.

As [O III] $\lambda4363$ Å is not detected in the $z = 0.79$ galaxy, direct temperature measurement is not feasible. For galaxies with redshifts greater than ~ 0.4, Hα and [N II] are redshifted beyond the optical passband, and of all the strong-line ratios, only R_{23} and O_{32} are available. Caution must be taken with reported calibrations made with O_{32}, as some authors define O_{32} = F([O III]λ4959) + F([O III]λ5007)) / F([O II]) , while others use O_{32} = F([O III])λ5007 / F([O II]). In this work O_{32} will henceforth refer to O_{32} defined as F([O III]λ4959) + F([O III]λ5007)) / F([O II]) unless otherwise stated. The abundance-sensitive R_{23} parameter is defined as:

$$\mathrm{R}_{23} = \frac{\mathrm{F}([\mathrm{O\,II}])\lambda3727 + \mathrm{F}([\mathrm{O\,III}])\lambda\lambda4959, 5007}{\mathrm{F}(H\beta)}$$

R_{23} uses emission lines with rest wavelengths in the blue part of the spectrum, and hence is a useful indicator of abundance in star-forming galaxies across a large range of cosmic time (Moustakas et al. (2010); KK04). It also has limitations, as it must be adequately corrected for stellar absorption (Section 7.3) and dust attenuation (Section 7.4), and is also sensitive to AGN contamination

(KE08). Calculation of abundance from the R$_{23}$ parameter is also complicated by the fact that the relationship between R$_{23}$ and abundance displays a double-valued behaviour, with a given value either representing the metal-poor lower branch, or the metal-rich upper branch, with the transition at 12 + log(O/H) $\approx$ 8.4 referred to as the turn-around region. In the metal-poor regime, R$_{23}$ increases monotonically with metallicity since the intensity of collisionally excited [O II] and [O III] lines scales with abundance. The decreasing behaviour in the upper branch of the R$_{23}$ sequence reflects the dominance of oxygen cooling over abundance in metal-rich regions. The nebular cooling is caused by collisional excitation followed by photon emission, and this process reduces the electron temperature in the nebula, leading to a decrease in the rate of collisional excitation of the oxygen lines (Kennicutt et al. 2003; Jabran Zahid et al. 2010).

R$_{23}$ is sensitive to the ionisation state of the nebula, in particular in the low-metallicity regime, where R$_{23}$ is not a strong function of metallicity. The ionisation parameter characterises the ionisation state of the gas, and can be defined as the ratio of the number of hydrogen-ionising photons passing through a unit area per second to the hydrogen density of the gas. The ionisation parameter q has units of cm s^{-1} and can be considered to be the maximum velocity ionisation front that a radiation field is able to drive through the nebula (KE08). A dimensionless form of the ionisation parameter can be defined as:

$$\mathrm{U} \equiv \frac{q}{c} \equiv \frac{Q(H)}{4\pi r_o^2 n(H) c} \tag{7.6}$$

KD02 give curves for log([O III]5007/[O II]) vs q for a range of metallicities- their Figure 1 is reproduced in our Figure 7.8. Any good calibration of R$_{23}$ will include some term to account for the dependence on ionisation parameter. The O$_{32}$ parameter is generally used as a probe of the ionisation parameter. It is interesting to note that, the sample of 66 $0.47 < z < 0.92$ galaxies from the Canada-France Redshift Survey (CFRS) presented in Lilly et al. (2003) exhibit values of $O_{32} < 1$ meaning F([O II]λ3727) > F([O II]$\lambda\lambda$4959, 5007). This galaxy has $O_{32} = 1.11 \pm 0.16$, meaning that the oxygen lines have comparable intensity. The LBGs at $z \geq 1.9$ from Lemoine-Busserolle et al. (2003) and Pettini et al. (2001) all exhibit $O_{32} > 1$, and the majority have $O_{32} > 2$. Clearly, there is a large change in the dominant ionisation state of oxygen between these two epochs, and this galaxy at $z = 0.7895$ would appear to have

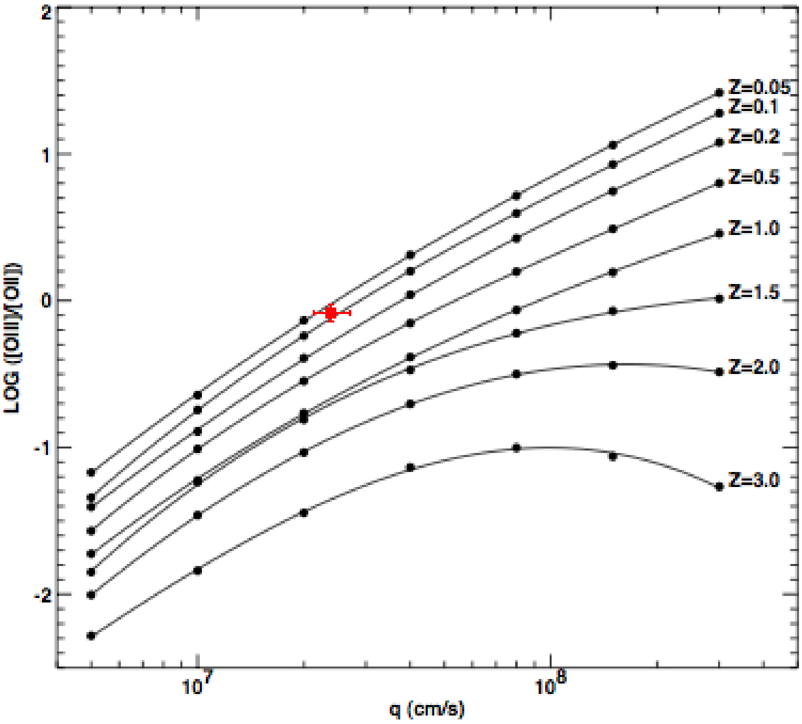

Figure 7.8: *Plot showing log([O III]/[O II]) vs q calculated using photoionisation models for a range of metallicities from 0.05 to 3 times solar. Filled points represent the model data points at ionisation paramters (from left to right): 5 $\times 10^6$, 1e7, 2$\times 10^7$, 4$\times 10^7$, 8$\times 10^7$, 1.5$\times 10^7$ & 3$\times 10^7$ cm s^{-1}. This figure is reproduced from KD02 These authors define O_{32} as F([O III])λ5007/F([O II]), and so ([O III]) in the y-axis title refers to F([O III])λ5007. The range of values of [O III]λ5007/[O II] and q for which we find physical solutions for the metallicity are plotted as the red point with associated error bars. The range in [O III]λ5007/[O II] is 0.84± 0.12, giving values for q of 2.14-2.69 $\times 10^7$.*

an intermediate ionisation state.

In order to determine the metallicity of the $z = 0.79$ galaxy ,we explore a number of calibrations. The results for these calibrations are shown in Table 7.4. The calibration of M91 is presented here in its analytical form which was given by Kobulnicky et al. (1999)) :

$$\begin{aligned} 12 + \log(\mathrm{O/H})_{\mathrm{lower}} &= 12 - 4.944 + 0.767x + 0.602x^2 \\ &\quad - y(0.29 + 0.332x - 0.331x^2) \end{aligned} \tag{7.7}$$

$$\begin{aligned} 12 + \log(\mathrm{O/H})_{\mathrm{upper}} &= 12 - 2.939 - 0.2x - 0.237x^2 - 0.305x^3 - 0.0283x^4 \\ &\quad - y(0.0047 - 0.0221x - 0.102x^2 - 0.0817x^3 - 0.00717x^4) \end{aligned} \tag{7.8}$$

where $x = \log(\mathrm{R}_{23})$ and $y = \log(\mathrm{O}_{32})$.
The R_{23} calibration of KK04 is based on the models of KD02, and is carried out in an iterative process, first estimating the ionisation parameter q:

$$\begin{aligned} \log q = &\{32.81 - 1.153y^2 + [12 + \log(\mathrm{O/H})](-3.396 - 0.025y + 0.1444y^2)\} \\ \times &\{4.603 - 0.3119y - 0.163y^2 + [12 + \log(\mathrm{O/H})](-0.48 + 0.0271y + 0.02037y^2)\}^{-1} \end{aligned} \tag{7.9}$$

where $y = \log(\mathrm{O}_{32})$. The $12 + \log(\mathrm{O/H})$ used here is an initial guess, the choice of which will not affect the final solution. We choose 7.5 as the guess for the lower branch, and 9.5 as the guess for the upper branch, which are the range of values plotted in Figure 7 of KK04 . The first estimate of ionisation parameter generated from this equation is used to derive an improved metallicity estimate from one of the following equations (Equations 7.10 and 7.11), depending on whether the upper or lower branch is assumed. Again, $x = \log(\mathrm{R}_{23})$.

$$\begin{aligned} 12 + \log(\mathrm{O/H})_{\mathrm{lower}} &= 9.72 - 0.777x - 0.951x^2 - 0.072x^3 - 0.811x^4 \\ &\quad - \log q(0.0737 - 0.0713x - 0.141x^2 + 0.0373x^3 - 0.058x^4) \end{aligned} \tag{7.10}$$

$$\begin{aligned} 12 + \log(\mathrm{O/H})_{\mathrm{upper}} &= 9.40 + 4.65x + 3.17x^2 \\ &\quad - \log q(0.272 + 0.547x - 0.513x^2) \end{aligned} \tag{7.11}$$

Equation 7.9 and Equation 7.10 or Equation 7.11 are iterated until the value of 12 + log(O/H) converges, typically 4 or 5 iterations. The range of values for q determined from this method are 2.14 - 2.69 $\times 10^7$, as shown in Figure 7.8.

The calibration provided by T04 is based on a large SDSS sample of $\sim$ 53000 galaxies, and is based on a sophisticated fit to the first four Balmer lines, and to the forbidden lines [O II] λ3727, [O III] $\lambda\lambda$4959, 5007, [N II] $\lambda\lambda$6548, 6584 and [N II] $\lambda\lambda$6717, 6731, adapted from the method of Charlot and Longhetti (2001). An analytical fit is provided to their Bayesian metallicity values for the upper branch (12 + log(O/H) > 8.5) only, as their sample does not cover the lower branch well. This fit is given as:

$$12 + \log(\mathrm{O/H}) = 9.185 - 0.313x - 0.264x^2 - 0.321x^3 \tag{7.12}$$

where $x = \log(\mathrm{R}_{23})$.

The calibration of Zaritsky et al. (1994) is only valid for the upper branch of the R$_{23}$ relationship, where 12 + log(O/H) > 8.4. It is given as:

$$12 + \log(\mathrm{O/H}) = 9.265 - 0.33x - 0.202x^2 - 0.207x^3 - 0.333x^4 \tag{7.13}$$

where $x = \log(\mathrm{R}_{23})$. This fit does not explicitly account for the ionisation parameter and so the other calibrations given here are preferable. Of the empirical calibrations, the only one based on R$_{23}$ is that of Pilyugin and Thuan (2005). This is given as:

$$12 + \log(\mathrm{O/H})_{\mathrm{lower}} = \frac{R_{23} + 106.4 + 106.8P - 3.40P^2}{17.72 + 6.60P + 6.95P^2 - 0.302R_{23}} \tag{7.14}$$

$$12 + \log(\mathrm{O/H})_{\mathrm{upper}} = \frac{R_{23} + 726.1 + 842.2P - 337.5P^2}{85.96 + 82.76P + 43.98P^2 + 1.793R_{23}} \tag{7.15}$$

where the factor P accounts for the ionisation parameter and is given as ([O III]$\lambda\lambda$4959, 5007 / Hβ)/R$_{23}$. However, the upper branch calibration is only valid for 12 + log(O/H) > 8.25 and the lower branch for 12 + log(O/H) < 8.0. Using our range of values for R$_{23}$ and P, Equation 7.15 gives only values for 12 + log(O/H) which are less than 8.25 and Equation 7.14 gives only values for 12 + log(O/H) greater than 8.0, indicating that this calibration does not provide a valid solution for this galaxy. For this reason, we do not adopt this calibration further.

Table 7.4. Metallicity Estimates for $z = 0.79$ Galaxy

Calibration	Upper	Lower
M91	8.36 - 8.53	8.18 - 8.34
KK04	8.49 - 8.62	8.37 - 8.47
T04	8.5 - 8.54	$\cdots$
Z94	8.41 - 8.55	$\cdots$

The value of R_{23} for this galaxy (given in Table 7.2) is 8.84 ± 1.82, and the corresponding value of O_{32} is 1.11 ± 0.16. Unfortunately, this value is very close to the turnaround region on the R_{23} - abundance diagram. If the R_{23} value for this galaxy placed it further away from the turnaround region, a comparison between the calibrations outlined above would be strongly recommended. In this case however, the position of the of the R_{23} value in this overlap region means that within the errors on the line fluxes, the calibrations which provide discrete solutions for the two branches do not give a physical result in every case, i.e. one in which the metallicity calculated for the upper branch is higher than that calculated for the lower branch. As mentioned in Moustakas et al. (2010), objects in this overlap region which are statistically consistent with being on either the upper or lower branch must have correspondingly large errors on the abundance. Following their method of searching for the physically valid subset of solutions within the range of solutions close to the turnaround region, we explore the range of possible values of 12 + log(O/H) given our line flux errors. The calibrations of Zaritsky et al. (1994) and T04 are only valid for the upper branch of R_{23}. If we are to assume the upper branch ($12 + \log(O/H) > 8.4$) the range of values given for the Zaritsky et al. (1994) calibration by Equation 7.13 are $8.41 \lesssim 12 + \log(O/H) \lesssim 8.55$. Likewise, assuming the upper branch ($12 + \log(O/H) > 8.5$) for the T04 calibration, Equation 7.12 gives $8.5 \lesssim 12 + \log(O/H) \lesssim 8.54$. Within the range of R_{23} and corresponding O_{32} values, we find a range of physical values of metallicities for the lower branch of the M91 calibration ranging from $8.18 \lesssim 12 + \log(O/H) \lesssim 8.34$, and for the upper branch, $8.36 \lesssim 12 + \log(O/H) \lesssim 8.53$, but a number of unphysical solutions can also be found. The calibration of KK04 generally gives higher values than M91. While the formal values of R_{23}

and O_{32} listed in Table 7.2 give unphysical solutions for the KK04 calibration, within the line flux errors a range of valid solutions for this calibration can be found covering $8.37 \lesssim 12 + \log(O/H) \lesssim 8.47$ on the lower branch, and $8.49 \lesssim 12 + \log(O/H) \lesssim 8.62$ on the upper branch. Moustakas et al. (2010) use the middle panel of their Figure 6 to illustrate a situation similar to this using the KK04 calibration, and find that galaxies which have an ambiguous branch determination also have large associated errors. In such cases, they take the metallicity to be the average of the two branches, and typically find these to lie at around $12 + \log(O/H) \sim 8.5$. The average of the two branches for our KK04 calibration is indeed $12 + \log(O/H) = 8.495 \pm 0.125$ and we caution that until further observations provide more lines, specifically Hα and [N II], to be used in other strong-line ratio calibrations, we are unfortunately probing a galaxy lying at the most uncertain region of the R_{23} - abundance diagram. Integral field spectroscopy data in the infrared could be the key in this case, as it could probe the correct wavelength range for these lines, and also potentially allow one to search for a radial abundance gradient, which could provide crucial constraints on inside-out gas distribution and star formation. Gas-phase metallicities have been observed to decrease from the centre of disk galaxies to the outside (Zaritsky et al. 1994; Pilyugin et al. 2004). Part of the problem of differences between the various metallicity calibrations could be related to the issue of using integrated spectra to derive the metallicity, which may not account for radial abundance gradients.

Ideally one would use a line ratio such as [N II]/Hα or [N II]/[O II] (KE08) to break the degeneracy in R_{23} and determine the correct branch from which to take the metallicity. As both of these involve [N II] which is beyond the scope of the $z = 0.79$ observations, future observations in the infrared regime may hold the key to a definitive determination of which branch to assume. As a tentative step towards identifying the location in the R_{23} - abundance diagram, we adopt the method of (Nagao et al. 2006). These authors use two samples, one of which is effectively taken from the upper branch theoretically-calibrated sample of T04, and the other consisting of relatively low metallicity galaxies ($7.0 \lesssim 12 + \log(O/H) \lesssim 8.5$) determined from direct measurements of the [O III]λ4363Å line. Given the tendency of direct measurements to underestimate the abundances, it is likely that in terms of empirical calibrations our galaxy falls within this lower range given its theoretical abundance from the KK04 calibration of $12 + \log(O/H) \sim 8.495 \pm 0.125$. In order to compare our abundance with the lower-metallicity sample, this theoretical value must be converted to a calibration based on direct measurements. KE08 give conversion coefficients allowing the conversion to the empirical calibration of Pettini and Pagel (2004). Their "O3N3" method, based on [O III] and [N II] line ratios is chosen, as it is recommended by KE08 as the most robust empirical calibration to use as a base. Following the conversion, the original KK04 lower branch values become $8.15 \lesssim 12 + \log(\mathrm{O/H}) \lesssim 8.19$, and the upper branch becomes $8.19 \lesssim 12 + \log(\mathrm{O/H}) \lesssim 8.28$. Nagao et al. (2006) suggest a number of possible methods to break the degeneracy in R_{23} and to determine the correct branch for a particular value. The peak or turnaround in the R_{23} - abundance relation for these galaxies measured using the direct method occurs at 12 + log(O/H) $\sim$ 8.0, at which point the empirically derived ratio of [O III]λ5007/[O II] is $\sim$ 2. Therefore, if [O III]λ5007/[O II] ≤ 2, one can expect the R_{23} value to be the part of the upper branch of the sequence. While we caution that this relation is based on observations of local SDSS galaxies, the intrinsic value of [O III]λ5007/[O II] $= 0.84 \pm 0.12$ would indicate that this galaxy occupies the upper branch, compounded by the fact that the metallicity in terms of the Pettini and Pagel (2004) empirical calibration is greater than the turnaround value of $12 + \log(\mathrm{O/H}) = 8.0$. The relationship between [O III]λ5007/[O II] and abundance is shown in Figure 9 of Nagao et al. (2006), reproduced here in Figure 7.9. These authors note that [O III]λ5007/[O II] can be used in this manner since even though O_{32} is not a good metallicity indicator due to its dependence on ionisation parameter, the spread in ionisation parameter for a given metallicity is small. Another crude indicator that the upper branch is a reasonable assumption is the fact that the local luminosity-metallicity (L-Z) relation shows that objects more luminous than $M_B \simeq -18$ tend to have metallicities greater than 12 + log(O/H) $\sim$ 8.4 (Kewley et al. 2004). The L-Z relationship is examined for a sample of 64 galaxies in the redshift range $0.26 \leq z \leq 0.82$ in Kobulnicky et al. (2003), and some evidence is found for an evolution with redshift. Galaxies in the range $z = 0.6 - 0.82$ in this sample are found to be about 40% more metal-poor at fixed luminosity than local galaxies. Figure 6 of Kobulnicky et al. (2003) would indicate that for $z = 0.6 - 1.0$, all objects more luminous than $M_B \simeq -19.5$ have metallicities greater than 12 + log(O/H) $\sim$ 8.4. In terms of this relationship, the value of M_B = -21.3 found for our galaxy would again indicate a location on the upper branch. However we do note that the sample shown in Figure 6 of Kobulnicky et al. (2003) for

$z = 0.6 - 1.0$ does not show any other galaxies with a metallicity as low as our estimated value of 12 + log(O/H) $\simeq$ 8.5 with a luminosity as high as M_B = -21.3.

A further relation shown by Nagao et al. (2006) for their two samples is the relationship between abundance and the ratio [Ne III]λ3869/[O II]λ3727. The value calculated for this line ratio is given in Table 7.2 as 0.07±0.04. Figure 15 of (Nagao et al. 2006) is reproduced (with slight modification) here in Figure 7.10. Placing [Ne III]λ3869/[O II]λ3727 = 0.05±0.03 on the polynomial fit to the points in this abundance diagram results in a metallicity close to $Z_\odot$, which is higher than estimates from the R_{23} indicators. There is a large flux error on the [Ne III] line as it is located in a noisy region of the spectrum and is not an extremely strong line. There is also evidence of a large dispersion in relationships between abundance and [Ne III]/[O II] (e.g. Pérez-Montero et al. (2007)), due to the fact that this ratio is strongly affected by the ionisation paramter, and so is not the most reliable diagnostic of the metallicity. Hence we do not adopt this high value of 12 + log(O/H), but take it as a further indicator of a location on the upper branch. Nagao et al. (2006) also point out that in low-metallicity galaxies (12 + log(O/H) < 8.0), the intensity of [Ne

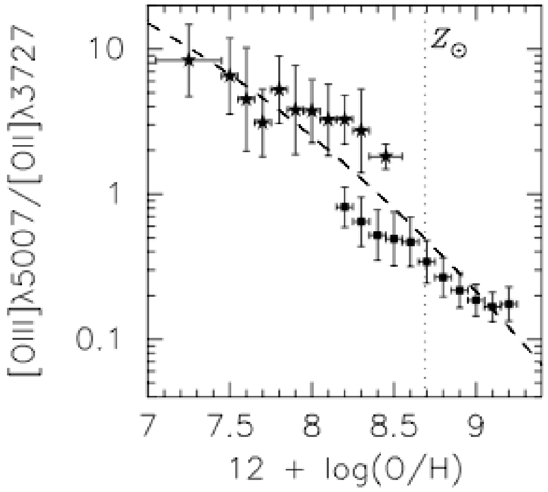

Figure 7.9: *Relationship between abundance and the [O III]λ5007/[O II] ratio, from Nagao et al. (2006), their Figure 9 (modified). The stars are the lower metallicity sample, with metallicities from direct measurements of [O III]λ4363Å. The squares are taken from the SDSS sample of Tremonti et al. (2004) and hence have metallicities from theoretical calibration. The samples have been separated into oxygen abundance bins of width Δ[log(o/h)] = 0.1, with the best-fit polynomial function shown as a dashed line. The dotted vertical line indicates solar metallicity of 12 + log(O/H) = 8.69.*

III]λ3869Å becomes comparable to [O II]λ3727Å as can be seen in the shape of the slope in Figure 7.10. One way in which this relation can be utilised is to examine the variation of the F([Ne III])λ3869/F([O II])λ3727 across the spatial extent of the galaxy. As outlined in Section 4.4, as well as extracting an individual spectrum for the whole galaxy from the Keck data, it was also possible to extract individual spectra over 5-pixel wide extraction ranges across the spatial extent of the galaxy. There is a clear variation in the strength of the [Ne III] line compared to the [O II] line in these spectra. The central extraction range has a [Ne III]/[O II] ratio of 0.05, comparable to the ratio for the overall spectrum. However, in the outer extraction ranges, the strength of [Ne III] relative to [O II] increases by a factor of four to 0.2. The actual strength of [O II] is strongest in the central spectra and falls off towards the edges as expected, ruling out a false effect resulting from incorrect extraction ranges. This decrease in the [Ne III]/[O II] ratio could be construed as an indication of an abundance gradient. The slope of Figure 7.10 shows that the ratio decreases with increasing abundance. The values of F([Ne III])λ3869/F([O II])λ3727 for each spectral slice are shown in Figure 7.11, along with their relative position on the 2D spectrum. The position of the spatial extraction regions are shown overlaid on the [O II] emission line only here for clarity, but the same ranges were used across the entire wavelength range. A value for the topmost spatial spectrum is not included as this is very noisy, and [Ne III] is not formally detected above the noise. The general shape of the left-hand plot indicates higher metallicity at the centre of the galaxy, decreasing towards the edges. If the values of [Ne III]/[O II] found for each of the spectra are placed on the lower diagram in Figure 7.10, a variation of $\sim$ 0.75 dex in abundance is inferred between the centre and edge. In order to estimate the gradient the physical size of this region must be determined. The overall extraction range corresponds to $4\farcs148$. At this redshift, the scale is 7.476 kpc per arcsecond, giving a size of 31 kpc. This must be corrected for the magnification factor of 4, resulting in an intrinsic physical size of 7.75 kpc. The variation of 0.75 dex occurs from the centre to the edge, i.e. 3.875 kpc. This allows us to make a rough estimate of the gradient as -0.19 dex/kpc. The trend for disk galaxies to display metallicity gradients decreasing from the centre outwards is well documented (Zaritsky et al. 1994; Pilyugin et al. 2004). Local disk galaxies typically display gradients of $\sim$ -0.05 dex/kpc (Rupke et al. 2010). These authors, along with Kewley et al. (2010) have also measured the abundance gradient in strongly-interacting pairs, and have revealed the lack of a gradient in merging galaxies. The physical mechanism involved is thought to be the tidal motion caused by the merger which allows lower metallicity gas at high radii to flow into the high-metallicity centre, diluting the local abundance and wiping out the gradient. At high redshift, Jones et al. (2010) have recently presented evidence of a strong metallicity gradient of $\sim$ -0.3 dex/kpc in a gravitationally-lensed galaxy at $z = 2$ using integral field spectroscopy and measurements of the [O III], Hα and [N II] lines. Metallicity gradients are a key signpost to inside-out formation. Further observations at this key epoch in the star-formation history of the Universe will help bridge the gap in the understanding of galaxy assembly between high-redshift and local galaxies.

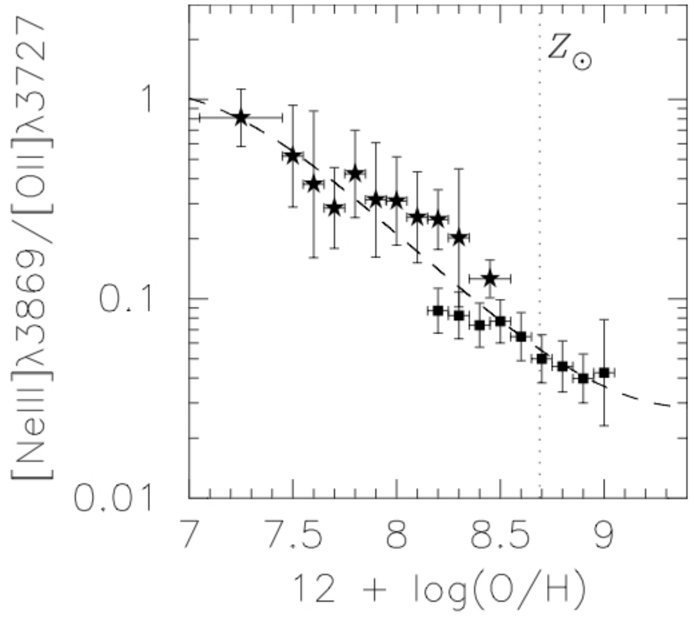

Figure 7.10: *Relationship between abundance and the [Ne III]/[O II] ratio, from Nagao et al. (2006), their Figure 15 (modified). The black stars and squares have the same meaning as Figure 7.9. The [Ne III]/[O II] ratio decreases with increasing metallicity for both empirically and theoretically calibrated samples.*

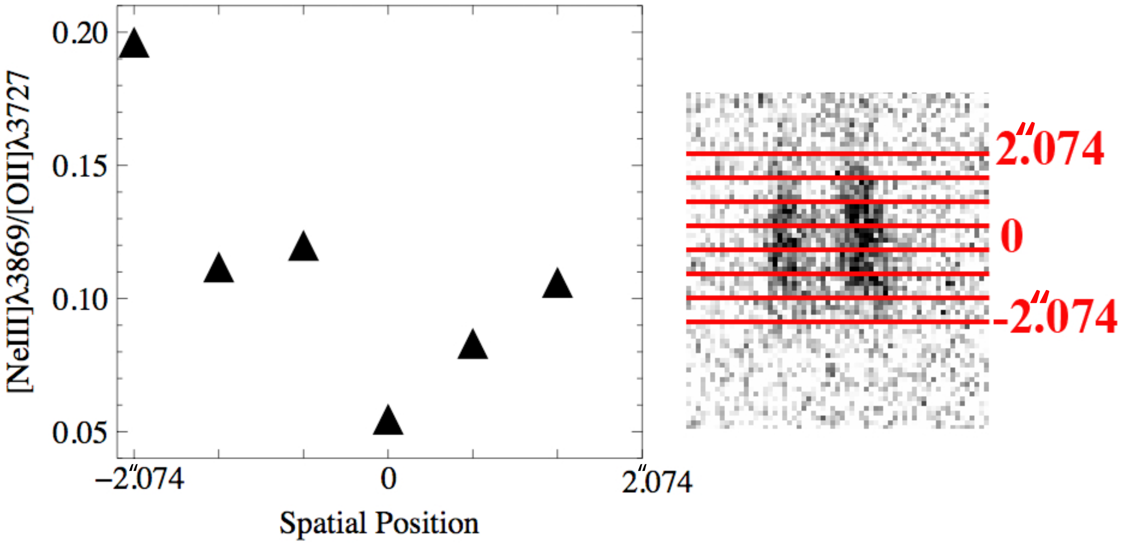

Figure 7.11: *Left panel shows the variation of the [Ne III]/[O II] ratio with spatial position, indicating a metallicity gradient across the spatial extent of galaxy. The extraction range of the overall spectrum was 4.″148, and 7 individual spectra were extracted across this range. The right panel indicates the location of each individual spectrum in the spatial direction, overlaid on the [O II] emission line for clarity. [Ne III] was not formally detected in the noisy uppermost spectrum.*

A correlation between mass and metallicity arises if low mass galaxies have larger gas fractions than higher mass galaxies as is observed in local galaxies (T04). Theory predicts that in a closed box model, as time progresses, mean stellar metallicity of galaxies increases with age as galaxies undergo chemical enrichment, while the stellar mass of a galaxy will increase with time as galaxies are built through merging processes, leading to the observed slope in the M-Z relation at high redshifts (Jabran Zahid et al. 2010; Pérez-Montero et al. 2009; Kobulnicky et al. 2003). The study of the M-Z relation is of extreme importance, as both mass and metallicity address key stages of the lifecycle of gas in a galaxy. The stellar mass indicates how much of the galaxy's gas exists as stars, while the metallicity can be viewed as an indication of the extent to which this gas has been reproccesed by stars and interacts with the environment. As the SFR density has decreased strongly between $z \sim 2$ and $z = 0$, it is central to understand how these quantities evolve on the same timescale. KE08 compare nine strong-line calibrations, and find that the choice of calibration can change the y-intercept of the mass-metallicity ($M - Z$) relation by up to 0.7 dex in 12 + log(O/H). These authors caution that due to the range of calibrations available, there is no way of telling which one is correct, although comparison between calibrations shows that differing the ionisation parameter among galaxies does not cause or contribute to the scatter. A relative conversion between the indicators is provided by KE08, so that relative comparisons of metallicities are reliable in a sample of galaxies. This is useful for comparing the M-Z relations from different samples by authors who may define their metallicities from different calibrations, and allows the M-Z relation to be built up to higher redshifts by using all available data in a consistent manner. Recent observations of higher redshift galaxies in terms of the M-Z relation shows evidence for evolution of the zero-point of the relationship with redshift-there is a trend for galaxies at a fixed mass to have higher abundances at lower redshifts. This has been reported for the VIMOS VLT Deep Survey (VVDS) (Lamareille et al. 2009; Pérez-Montero et al. 2009) at $0.5 \lesssim z \lesssim 1.24$, for the DEEP2 Galaxy Redshift Survey by both Jabran Zahid et al. (2010) ($0.75 \lesssim z \lesssim 0.82$) and Liu et al. (2008) ($1.0 \lesssim z \lesssim 1.5$), as well as for a sample at $z < 3$ (Maiolino et al. 2008). The relationship between luminosity and metallicity (L-Z) has also been explored; however optical luminosity may not be a reliable proxy for the stellar mass of a galaxy as luminosities are sensitive to the level of current star formation and are extinguished by dust.

Figure 7.12 is reproduced from Figure 8 of Jabran Zahid et al. (2010). The solid line is the L-Z relation found for a large sample at the same redshift range as our galaxy ($0.75 \lesssim z \lesssim 0.82$), and shows a significant offset from the local relation found in T04, indicated with the dashed line. The fact that we measure low metallicity and yet have a very high luminosity means that this galaxy is considerably off the L-Z relation. This again raises the question as to a possible AGN contribution. As well as increasing the luminosity, an AGN would serve to increase the R_{23} ratio, as the ionised oxygen would be increased relative to Hβ. If this galaxy were originally an upper-branch galaxy as we postulate, the increased R_{23} value caused by AGN contribution would serve to lower the metallicity and push the value toward the turnaround region, which is indeed the location of the galaxy on the R_{23} - abundance diagram.

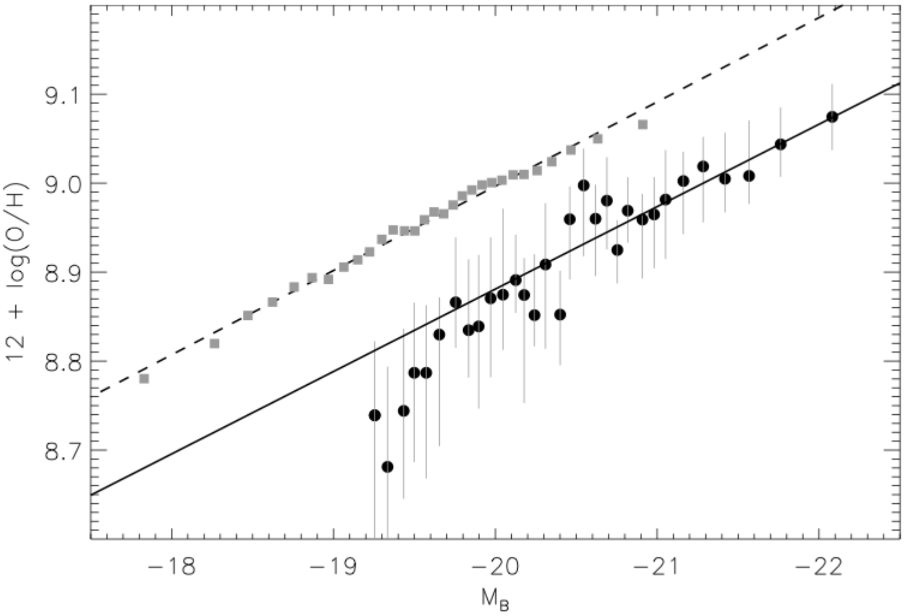

Figure 7.12: *Luminosity-metallicity (L-Z) relationship as shown in Jabran Zahid et al. (2010). The black circles are binned data from their sample at* $0.75 \lesssim z \lesssim 0.82$*, with the L-Z fit to these points shown as solid line. The grey squares fit by the dashed line are from the local sample of Tremonti et al. (2004).*

7.7 Star Formation Rate

The global star formation rate (SFR) is a fundamental parameter in the study of the formation and evolution of galaxies. Studies of cosmic evolution are concerned with untangling the mystery of how and when the buildup of mass in the Universe occurred. The luminosity density of the Universe has increased by at least an order of magnitude since $z \sim 1$ (Lilly et al. 1996), and this steepening of the luminosity function has been shown to be due to the increasing space density of blue star-forming galaxies at moderate redshift (Ellis et al. 1996). Understanding the growth of stellar mass in different types of galaxies is key to understanding galaxy evolution as a function of redshift. In individual galaxies, star formation rates probe the evolutionary history of the galaxy. Multi-wavelength, complete large-scale spectroscopic surveys are providing a wealth of data to probe the star-formation rate density and the luminosity function across a range of redshifts. SFRs can be estimated using a variety of methods, depending on the redshift of the source and which part of the spectrum is available for analysis. Common proxies which are sensitive to the ionising flux from young stars include the luminosity of emission lines such as Hα or [O II], or the far-UV continuum luminosity (Kennicutt (1998), henceforth K98). The difference between the SFR$_{FUV}$ and SFR$_{H\alpha}$ indicators lies in the type of stars they are sensitive to. Nebular Hα emission lines come from gas which has been ionised by the most massive O- and early B-type stars, with stellar masses of M$_* \gtrsim 17\ M_\odot$, tracing the SFR over the lifetime of such stars ($\sim$ few $\times 10^6$ years). The photospheres of significantly lower mass (M$_* \gtrsim 3\ M_\odot$) O- to late B-type stars are responsible for the UV flux used to estimate SFR$_{FUV}$, and thus this method is sensitive to star-formation averaged over timescales on the order of $\sim 10^8$ years (Lee et al. 2009). It has been shown in numerous studies including Rosa-González et al. (2002) and Kewley et al. (2002), that after correction of Hα for stellar absorption and reddening, these two indicators show good agreement. At higher redshifts, mid- or far-infrared (IR) radiation can also be used to estimate the SFR, as these measure the fraction of the flux from young stars which is absorbed by dust and then re-radiated at these wavelengths (K98). Unfortunately, there is widespread discrepancy between the UV, optical and IR indicators, and it is an important aim of future research to consolidate these, so that SFRs can be measured in a uniform way at every redshift. The Hα line luminosity, $L(H\alpha)$

is widely accepted as the most reliable tracer of star formation. Hα can be easily corrected for reddening and underlying stellar absorption as described in Sections 7.4 and 7.3. We take the equation for SFR$_{H\alpha}$ from K98:

$$\mathrm{SFR}_{H\alpha}(\mathrm{M}_{\odot}\mathrm{yr}^{-1}) = 7.9 \times 10^{-42} L(H\alpha)(\mathrm{ergs\ s}^{-1}) \tag{7.16}$$

Although our observations do not reach a high enough wavelength to observe the redshifted Hα line, an initial estimate of SFR$_{H\alpha}$ can be made by inferring the Hα line flux from the E(B-V) value calculated using Hβ and Hγ, and the intrinsic ratio between Hα and Hβ (Osterbrock 1989). The ratio is Hα/Hβ = 2.85, assuming Case B recombination, a temperature of of 10000K and electron density of 10^4 cm^{-3}. The Hα flux is then computed via:

$$\mathrm{F(H}\alpha)(\mathrm{ergs\ s}^{-1}\mathrm{cm}^{-2}) = \mathrm{F(H}\beta) \times 2.85 \times 10^{-0.4\,E(B-V)\,(k(\lambda_{H\alpha})-k(\lambda_{H\beta}))} \tag{7.17}$$

This results in an intrinsic Hα flux (de-magnified and corrected for reddening) of 2.0 $\pm 0.27 \times 10^{-15}$ ergs s^{-1} cm^{-2}, and a Hα luminosity L(Hα) of 5.81 $\times 10^{42}$ ergs s^{-1}. Using this value in Equation 7.16 gives an estimate on the Hα star formation rate of 46.14 $\pm$ 6.16 M$_{\odot}$ yr^{-1}. For redshifts beyond $z \sim 0.4$, Hα is redshifted beyond the optical window into the near infrared. At these higher redshifts $0.4 \lesssim z \lesssim 1.5$, the [O II] λ3727Å emission line can be used in place of Hα to estimate SFR. However, SFR$_{[OII]}$ is difficult to accurately calibrate as it more sensitive to reddening, oxygen abundance and ionisation parameter. Many earlier calibrations of SFR$_{[OII]}$, including K98, did not take these dependencies into account; however these are corrected for in the treatment of Kewley et al. (2004, henceforth K04). We examine SFR$_{[OII]}$ firstly using their equation 4, which makes no assumptions about typical reddening, allowing the user to correct for the amount of dust in individual galaxies.

$$\mathrm{SFR}_{[OII]}(\mathrm{M}_{\odot}\mathrm{yr}^{-1}) = (6.58 \pm 1.65) \times 10^{-42} L([OII])(\mathrm{ergs\ s}^{-1}) \tag{7.18}$$

Where $L([OII])$ must be corrected for reddening at [O II]. We have intrinsic F$_{[OII]}$ = 2.87 $\pm 0.17 \times 10^{-15}$ ergs s^{-1}cm^{-2}, which has been corrected to account for magnification due to lensing and reddening. The conversion to luminosity is given by:

$$L_{[OII]} = F_{[OII]} \times 4\pi D_L^2 = 8.37 \pm 0.5 \times 10^{42}\ \mathrm{ergs\ s}^{-1} \tag{7.19}$$

Table 7.5. $\mathrm{SFR}_{[OII],Z,o}$ from Kewley et al. (2004) Calibration

Diagnostic	a	b	12 + log(O/H)	$\mathrm{SFR}_{[OII]}$
M91	-2.29	21.21	8.36 - 8.53	17.79 ± 0.24
Z94	-1.75	16.73	8.41 - 8.55	12.27 ± 0.3
KD02[a]	-1.99	18.67	8.38 - 8.51	14.74 ± 0.27

[a] As we do not have an estimate for the KD02 metallicity, we use the conversion in KE08 to convert the upper-branch metallicity from KK04 into the KD02 system.

where D_L is the luminosity distance at $z = 0.7895$ in units of centimetres, and errors are based on the reported line flux errors in Table 7.1. Using this value in Equation 7.18, we compute $\mathrm{SFR}_{[OII]} = 55.9 \pm 17.1$ $\mathrm{M}_\odot$ yr^{-1}, where the error is based on that given in Equation 7.18 as well as the error in $L([OII])$. K04 examine a local sample of galaxies from the Nearby Field Galaxy Survey (NGFS) and find a strong relationship between metallicity and the relative strengths of [O II] and Hα. They further refine their calibration of $\mathrm{SFR}_{[OII]}$ by introducing a correction to account for the effect of metallicity on the SFR, based on the observed relationship between metallicity, and the [O II]/Hα ratio, thus bringing the $\mathrm{SFR}_{[OII]}$ more into line with $\mathrm{SFR}_{H\alpha}$. The corrected $\mathrm{SFR}_{[OII]}$ is given in their equation 9 as

$$\mathrm{SFR}_{[OII],Z,o}(\mathrm{M}_\odot \mathrm{yr}^{-1}) = \frac{7.9 \times 10^{-42} L([OII])(\mathrm{ergs\ s}^{-1})}{a[12 + \log(\mathrm{O/H})] + b} \tag{7.20}$$

where a and b are coefficients given in Table 7.5. The subscript "o" indicates correction based on observed [O II]/Hα values. This equation is only valid for a limited number of metallicity calibrations, which does not include the KK04 calibration. In order to examine the $\mathrm{SFR}_{[OII]}$ in terms of this, we convert these metallicities to the system of KD02 using the conversion given in KE08. This equation is also only valid for the upper branch and so for M91 and KK04 metallicities we use the upper branch results. The resulting $\mathrm{SFR}_{[OII],Z,o}$ from the three available metallicities are given in Table 7.5.

The final refinement of $\mathrm{SFR}_{[OII]}$ made by K04 is to introduce a dependency on ionisation parameter. Theoretical models are used to relate the [O II]/Hα

ratio to metallicity for a range of ionisation parameters. The curve for each ionisation parameter is characterized by a polynomial $\frac{[OII]}{H\alpha} = a + bx + cx^2 + dx^3$, which is then used to estimate the SFR in their Equation 14:

$$\mathrm{SFR}_{[OII],Z,t}(\mathrm{M}_\odot \mathrm{yr}^{-1}) = \frac{7.9 \times 10^{-42} L([OII])(\mathrm{ergs\ s}^{-1})}{a + bx + cx^2 + dx^3} \tag{7.21}$$

where subscript "t" indicates theoretical correction. The coefficients for ionisation parameters 2 $\times 10^7$ and 3 $\times 10^7$ are provided in K04, which bracket the range of ionisation parameters found for our galaxy in Section 7.6. Applying Equation 7.21 to the range of metallicities found for both M91 and KK04 upper branch calibrations ($8.36 \leq 12 + \log(\mathrm{O/H}) \leq 8.62$), we find $\mathrm{SFR}_{[OII],Z,t} = 41.39 \pm 7.28$, which we take to be the best estimate of the star formation rate. This analysis also allows us to verify our inferred value for Hα. The range of [O II]/Hα given by this metallicity and ionisation parameter range is 1.44 - 1.82. Using our known value for [O II], this places the value of Hα in the range $1.61 \times 10^{-15} - 2.03 \times 10^{-15}$ ergs s^{-1} cm^{-2}, consistent with the value of $2.0 \pm 0.26 \times 10^{-15}$ inferred from the Hβ flux.

In general, Hβ is not thought to be as effective as Hα to infer star formation rates, as Hβ suffers more strongly from underlying stellar absorption. KK04 give a lower limit on SFR from Hβ for their sample of 204 galaxies at $0.3 < z < 1.0$ in the GOODS-N (Great Observatories Origins Deep Survey-North) field using the equivalent width of Hβ and the absolute B-band magnitude M$_B$ to calculate the Hβ luminosity and hence the SFR:

$$L_{H\beta} = 5.49 \times 10^{31} \times 2.5^{-M_B} \mathrm{EW}_{H\beta} \tag{7.22}$$

$$\mathrm{SFR}_{H\beta}(\mathrm{M}_\odot \mathrm{yr}^{-1}) = \frac{2.8\, L_{H\beta}}{1.28 \times 10^{41}} \tag{7.23}$$

These equations do not account for extinction or underlying stellar absorption, and are necessarily a lower limit on SFR. However, we have corrected for stellar absorption using our best fit SED model, and can use the resulting Hβ EW in these calculations. As we are using a luminosity based on the intrinsic M$_B$, correction for magnification has already been carried out. Using these equations without any extinction correction as above, we calculate a lower limit of $\mathrm{SFR}_{H\beta} = 11.75$ M$_\odot$ yr^{-1}. We introduce a reddening correction using

Table 7.6. All Calculated Values of SFR for $z = 0.79$ Galaxy

Diagnostic	SFR $M_\odot$ yr^{-1}
Hα [a]	46.14 ± 6.16
[OII] [b]	55.9 ± 17.1
$[OII]_{Z,o}$ [c]	15.0 ± 3.03
$[OII]_{Z,t}$	41.39 ± 7.28
Hβ	44.81 ± 5.98

[a] Using the range of Hα values 2.6-3.3$\times 10^{-15}$ ergs s^{-1} cm^{-2}.

[b] From K04 Equation 4

[c] From K04 Equation 9, range of values from the three calibrations given in Table 7.5

our value of E(B-V) = 0.277 and correct via

$$L_{H\beta,corr} = L_{H\beta} \times 10^{0.4\,E(B-V)\,k(H\beta)}$$

This gives SFR$_{H\beta,corr}$ = 38.05 $M_\odot$ yr^{-1}, more in line with the estimates from theoretically-corrected [O II] and inferred Hα. KK04 use equivalent widths to investigate SFR and abundance, as their sample lacks accurate fluxing information. If in Equation 7.23, we use the Hβ luminosity calculated from the line flux and corrected for extinction, $2.05 \pm 0.27 \times 10^{42}$ ergs s^{-1}we calculate SFR$_{H\beta,corr}$ = 44.81 ± 5.98 $M_\odot$ yr^{-1}, consistent with the estimates from [O II] and Hα. The star formation rates from the various diagnostics are summarized in Table 7.6.

8

VLT Observations of Two Strongly Lensed Lyman Break Galaxies

In this Chapter I present spectra of two strongly-lensed Lyman Break galaxies at $z \sim 2 - 3$, both of which have been lensed by single massive elliptical galaxies at $z \sim 0.4 - 0.5$. These galaxies have been significantly magnified due to the lensing effect. These galaxies represent a bridge between the very high redshift galaxy studied in Chapter 5, when the Universe was in the early rapid stages of star formation, and the epoch at $z \sim 1$ studied in Chapter 7, when the star formation density had begun to decline. Lyman Break galaxies at $z \sim 2 - 3$ explore the peak of star formation history. A detailed glimpse at the inner workings of galaxies at such redshifts can only be afforded by gravitational lensing, and to date $\lesssim 20$ of these have been detected. These include the multiply-imaged "Sextet Arcs" (Frye et al. (2007), on which I am a co-author), the "8 o'clock arc" (Allam et al. 2006), the "Arc+Core" (Nesvadba et al. 2006), the "Cosmic Eye" (Smail et al. 2006), and the well-studied MS 1512-cB58 (more commonly referred to as cB58, Yee et al. (1996); Pettini et al. (2002)). These galaxies show a range of properties in their star formation, interstellar media, metallicities and dynamical states, which attests to the diversity of the galactic population at this interesting and active epoch in the history of the Universe.

8.1 Lyman Break Galaxies (LBGs)

Understanding the properties of galaxies at all epochs since the reionisation of the Universe is essential if astronomers are to constrain the history of galaxy evolution and the formation of the Hubble sequence. Until relatively recently (mid-1990s), observations of normal star-forming galaxies with redshifts larger than z $\sim$ 1 were virtually nonexistent, as a robust search method to identify these objects had not been developed. The main thrust of searches for galaxies beyond z $\sim$ 1 focused on searching for Lyα emission, and were largely unsuccessful. The pioneering break-through in studying galaxies in the redshift range $2.5 \lesssim z \lesssim 5$ came with the advent of imaging technology sensitive enough to identify "Lyman Break" galaxies. The Lyman break or continuum discontinuity at 912Å is very pronounced in the UV spectra of star-forming galaxies. The break, of an order of magnitude in luminosity density, is produced in the stellar atmospheres of high-mass stars, and is amplified due to photoelectric absorption by neutral hydrogen in the interstellar medium (ISM) and in the intervening intergalactic medium (IGM). The basic premise of the Lyman break technique is to image a particular field in 3 optical passbands, with wavelength sensitivity tuned such that the bluest filter is sensitive to photons from the blue side of the galaxy's Lyman-limit. The intermediate filter ideally images the portion of the spectrum which lies between the Lyα transition at rest-frame 1216Å and the Lyman break at 912Å, as this part of the spectrum can also be dimmed due to line-blanketing by the intervening Lyα forest. The reddest filter images the opacity-free part of the spectrum longward of the Lyα transition at 1216Å. For the redshift range $\sim 2.5 \lesssim z \lesssim 3.5$, in ground-based surveys, the U-band will image shortward of the Lyman break and hence will not detect any photons from the galaxy. If the field imaged in this manner contains a galaxy in this redshift range, the galaxy will appear in the two images taken in the redder bandpasses G and R, but will not show up in the U-band image. Such galaxies which "drop out" of a particular photometric bandpass due to the location of their rest-frame Lyman continuum discontinuity are known as "Lyman Break Galaxies" (LBGs). Steidel et al. (1996a,b) were the first to present follow-up spectroscopy of a number of these candidate LBGs using the LRIS spectrometer (Oke et al. 1995) on the 10 metre Keck telescope. The confirmation of a large proportion of these galaxies as normal star-forming galaxies at z > 2, showing no evidence for AGN activity, was the initial indication of the immense utility of the Lyman-break technique. For a redshift range $\sim 2.5 \lesssim$ z $\lesssim 3.5$, the U-band is the filter in which the galaxy "disappears" due to the Lyman-break; at higher redshifts, the galaxies drop out of redder filters-ie B[1]- or G-band dropouts at z $\sim$ 4, and V-band

---

[1] Ground-based filters

dropouts at z $\sim$ 5. The $z = 4.9$ galaxy discussed in Chapter 5 was initially selected for follow-up spectroscopy as a V-band dropout from a ground-based galaxy cluster survey, along with a number of other galaxies (Frye et al. 2002). A cut-out of this galaxy in the HST ACS images in the F475W, F625W and F775W filters is shown in Figure 8.1. The position of these filters relative to the UV spectrum of a template galaxy[2] at $z = 4.9$ is shown in Figure 8.2, and as expected from this figure, the galaxy drops out of the F475W filter.

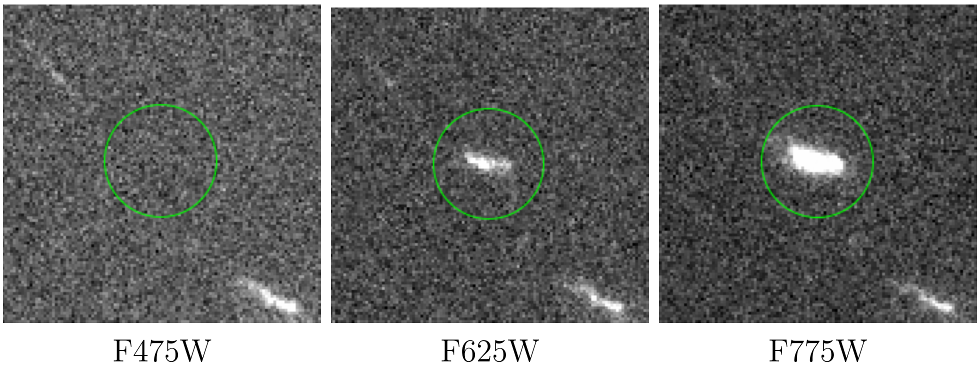

Figure 8.1: $z = 4.9$ *galaxy in three HST ACS filters, highlighting the dropout in the F475W band.*

Subsequent to the identification of $2.2 \lesssim z \lesssim 3.6$ galaxies presented in Steidel et al. (1996a,b), numerous LBG surveys were undertaken, and thousands of LBGs with $2.5 \lesssim z \lesssim 5$ have been identified. In general, individual LBGs are too distant and faint to study in detail, and their due to their great distance, the ground-based spectra have such low resolution that they are not useful beyond redshift identification using the strongest lines. At z > 2, in-depth studies of individual galaxies have focused on the most luminous or active galaxies, or else the small subset of galaxies which are magnified due to their serendipitous location along the line of sight to massive gravitational lenses. One approach which allows the examination of the characteristic rest-frame spectra of LBGs is the composite spectra method of Shapley et al. (2003). This approach involves the co-addition of the rest-frame UV spectra of large numbers of LBGs-the composite spectra presented in Shapley et al. (2003) combine 811 galaxies. This approach proved invaluable in characterising the typical attributes of this class of galaxy. These composite spectra can be broken down into galaxies showing Lyα in emission, in absorption or a combination of the two. Low-ionisation resonance metal lines such as Si II λ1260, O I λ1302,

---

[2] The template galaxy is taken from the model galaxies included in the Bruzual and Charlot (2003) GALAXEV package, and were originally presented by Tremonti et al. (2004).

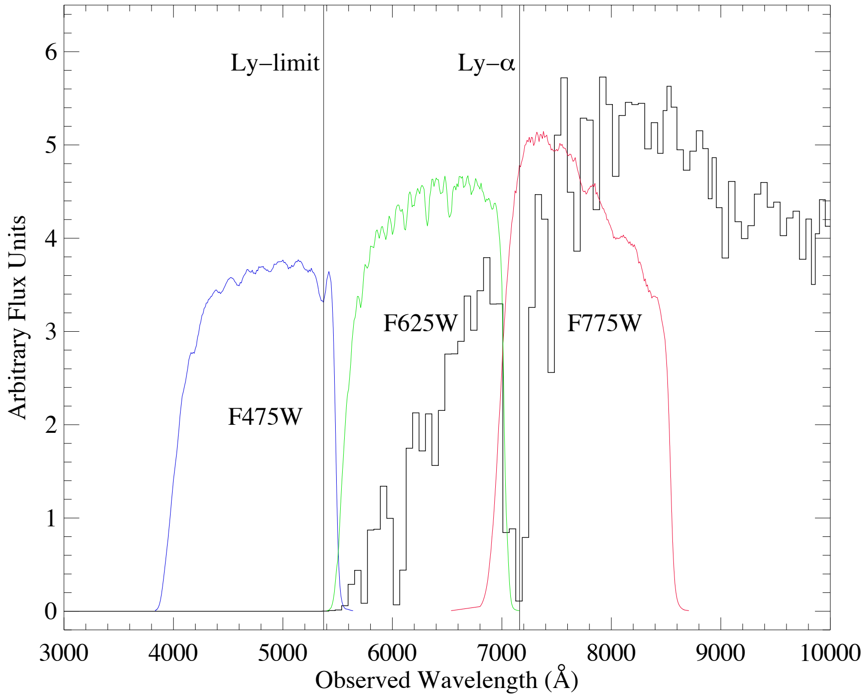

Figure 8.2: *A template galaxy SED from Tremonti et al. (2004) with an age of 100 Myrs and solar metallicity, redshifted to* $z = 4.9$. *HST ACS filters are overlaid to highlight the fact that the sharp break at the Lyman limit, 912Å* × *(1+z) occurs redward of the F475W filter. A galaxy at* $z = 4.9$ *will drop out of the F475W filter, as is shown in Fig. 8.1.*

+ Si II λ1304, C II λ1334, Si II λ1526, Fe II λ1608, and Al II λ1670, which are associated with the neutral interstellar medium (ISM) are observed. Also present in LBG spectra are metal lines of highly-ionised species including NV λλ1238.8,1242.8, Si IV λλ1393.8,1402.8 and C IV λλ1548.2,1550.8, which are associated with ionised interstellar gas and with P-Cygni stellar wind features originating in massive stars. Lyα when observed in emission in LBGs is similar to that discussed in Chapter 5 for the galaxy at $z \sim 5$. The line tends to be asymmetric with a blue absorption edge and an extended red wing. The blue side of the line is absorbed due to resonant scattering, and the asymmetrical emission in the red side of the line is interpreted to be due to Lyα photons being backscattered from the receding part of an outflowing "shell" of ISM gas. Signatures of such large scale outflows are ubiquitous in LBG spectra, with evidence for outflow velocities of > 300km s^{-1}, and star formation rates and physical sizes capable of driving "superwinds" similar to those seen in local starbursts (Heckman 2002; Lehnert and Heckman 1996).

8.2 Results of VLT Observations of "The Cosmic Horseshoe"

In this section I present the results from the 2.33 hours of VLT observations of this almost-complete Einstein ring (Section 3.1.5) which I reduced using the data reduction methods described in Chapter 4, with some modifications introduced specifically for this dataset (Section 4.5). Figure 8.3 (reproduction of Figure 3.8 for convenience) shows an SDSS r-band image of the Einstein ring with the slit overlaid. The Cosmic Horseshoe is an almost-complete Einstein ring with a diameter of $\sim$10″. It is formed by the gravitational lensing of a blue background galaxy at $z = 2.38$, due to the presence of a single massive foreground elliptical galaxy at $z = 0.444$. The initial discovery of the lensing system from the SDSS Data Release 5 (DR5) was presented by Belokurov et al. (2007), using low-resolution spectroscopy to determine the lens and source redshifts. These authors indicate four clumps with maximum surface brightness in the ring, and label these A, B, C and D. As shown in Figure 8.3, the slit position angle for these observations was chosen to allow light through the aperture from components A and D, while avoiding any contamination from the central galaxy. The resolution, measured from the 6300Å skyline is R = 1315. This galaxy has been studied in great detail by Quider et al. (2009) using

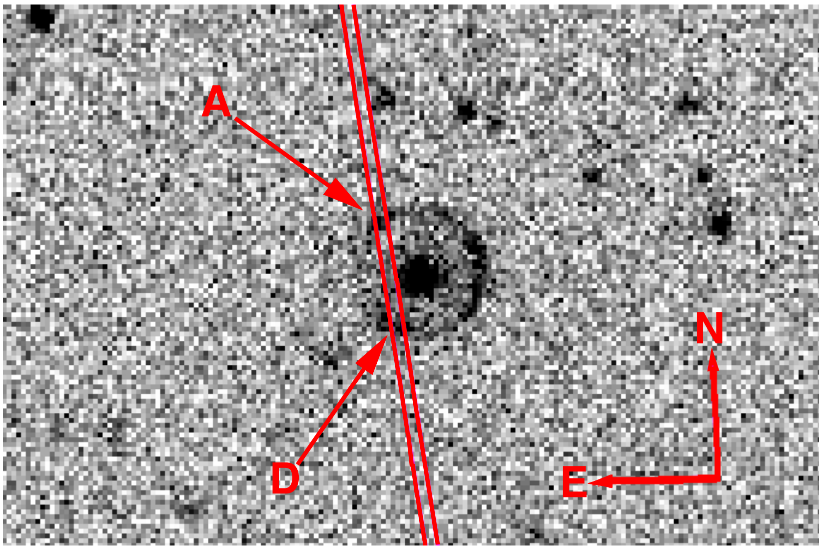

Figure 8.3: *Section of an SDSS r-band image showing the position of the 1.″0 width longslit used for the VLT FORS2 observations of the Cosmic Horseshoe. The slit was carefully aligned so as to cover two of the brightest knots in the Einstein ring, while minimizing contribution from the central lensing galaxy at* $z = 0.444$.

the Keck II telescope and the Echellete Spectrograph and Imager. The data presented therein (consisting of a total of 10 hours of exposure) are also in the rest frame UV bandpass, but with higher resolution (R ≈ 4000) and a wider spectral range (4000 - 10000Å, or 1184 - 2959Å in the rest frame) than the spectra presented in this chapter. Quider et al. (2009) find a systemic redshift of 2.38115, a metallicity of approximately $0.5Z_{\odot}$, velocities ranging from -800 km s^{-1} $< v <$ +250km s^{-1}, and evidence that the outflowing gas only covers a fraction ($\sim$ 60%) of the UV stellar continuum. The detailed lensing models constructed by Dye et al. (2008) give overall magnification factors of 24 ± 2. This galaxy was also observed by Hainline et al. (2009) in the near infra-red with the NIRSPEC instrument on the Keck II telescope. These authors found an overall extinction E(B-V) $\sim$ 0.15 from the Balmer decrement method (Section 7.4), a virial mass of $M_{vir} \simeq 10^{10} M_{\odot}$ and a star formation rate from the Hα line of 113 $M_{\odot}$ yr^{-1} after correction for reddening and magnification.

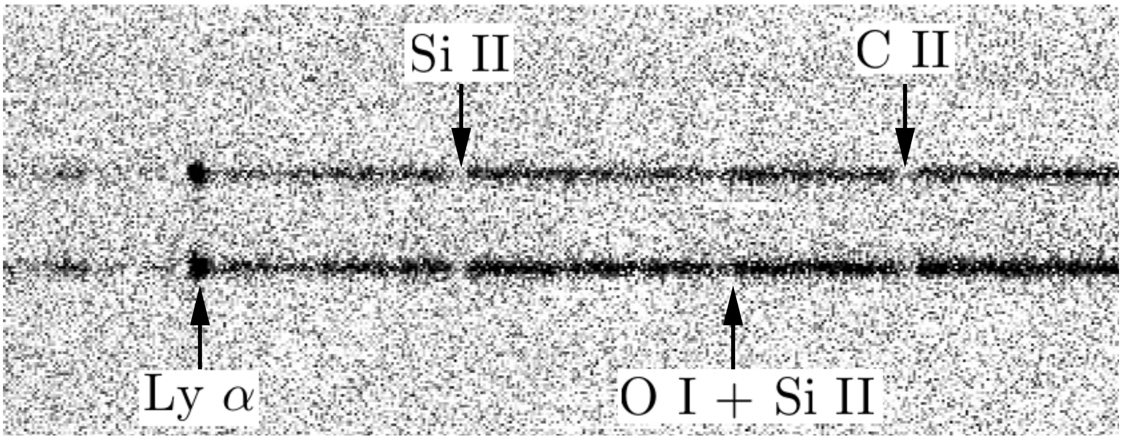

Figure 8.4: *A coadded image of all six 1400 second exposures of the Cosmic Horseshoe. The slit was aligned to intersect the horseshoe-shaped arc at two locations, hence we see two individual spectra of the galaxy in the image. Any differences in the two spectra are due to relative gas motions within the galaxy, or surface brightness variations. The upper spectrum here corresponds to the component marked "A" in Figure 8.3, while the lower spectrum corresponds to component "D".*

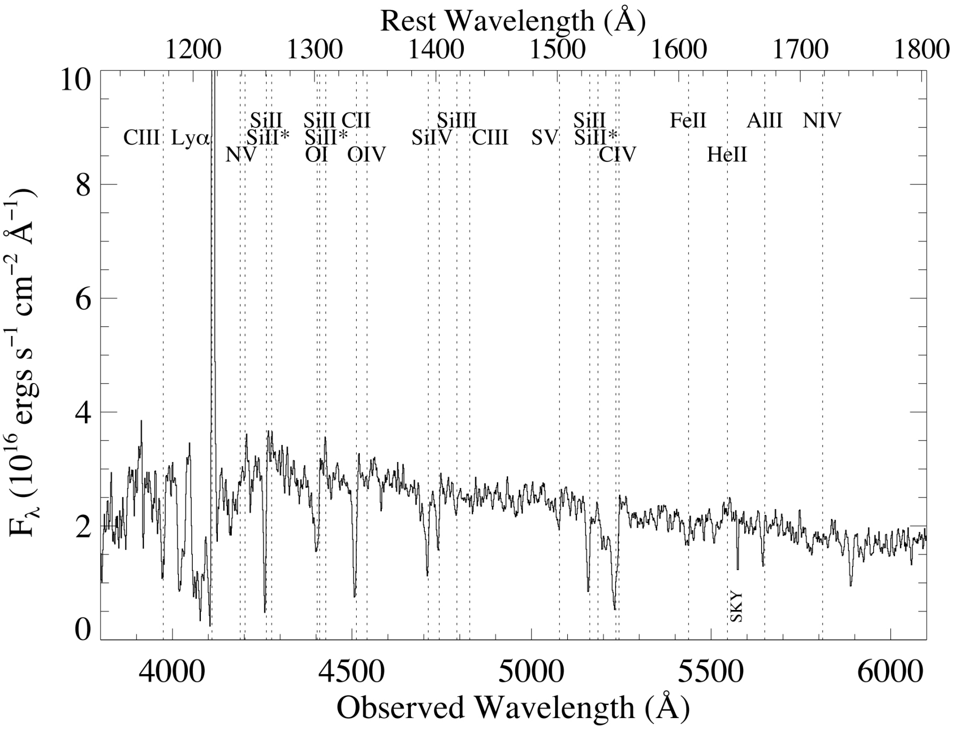

Figure 8.5: *Combined spectrum of the "Cosmic Horseshoe" galaxy at $z = 2.38115$, with both upper and lower spectra from each exposure combined, effectively doubling the exposure time.*

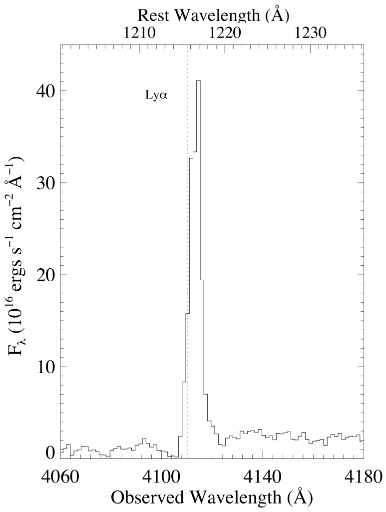

Figure 8.6: *Close up of the Lyα emission line of the Cosmic Horseshoe galaxy. The position of Lyα at the systemic redshift of $z = 2.38115$ is marked with a dotted vertical line.*

Figure 8.5 shows the final spectrum extracted from the six 1400 second exposures of the Cosmic Horseshoe. The Lyα line is shown separately in Figure 8.6. The line displays the typical asymmetric profile as seen in the $z \sim 5$ galaxy, with the nature of such emission discussed in Section 5.1. Quider et al. (2009) are able to resolve a double peaked structure in this line, with a narrow symmetric component of FWHM 50 km s^{-1} after correction for instrumental resolution; however detection of this component is beyond the resolution limit of the present data.

The alignment of the slit across two separate parts of the lensed arc while avoiding the central lensing galaxy means that two distinct spectra are formed on the 2D image, as shown in Figure 8.4. The upper spectrum in this image corresponds to the component marked "A" in Figure 8.3, while the lower spectrum is that of clump "D", deduced from the relative position of two other objects which are contained in the slit. It is found that the spectrum from component D is uniformly brighter in flux than that of component A by a factor of 1.52. Care was taken to use the same extraction width for both components. The Lyα emission line is also significantly weaker in the upper component. The only other significant difference in the spectra is at a wavelength corresponding to $\sim$ 1244Å in the rest frame, at which point an emission line is detected in component A which is absent in component D. This variation is highlighted in Figure 8.7, which shows the upper spectrum, labelled "A", offset from the lower spectrum "D" for clarity. This is close to the expected position of the N

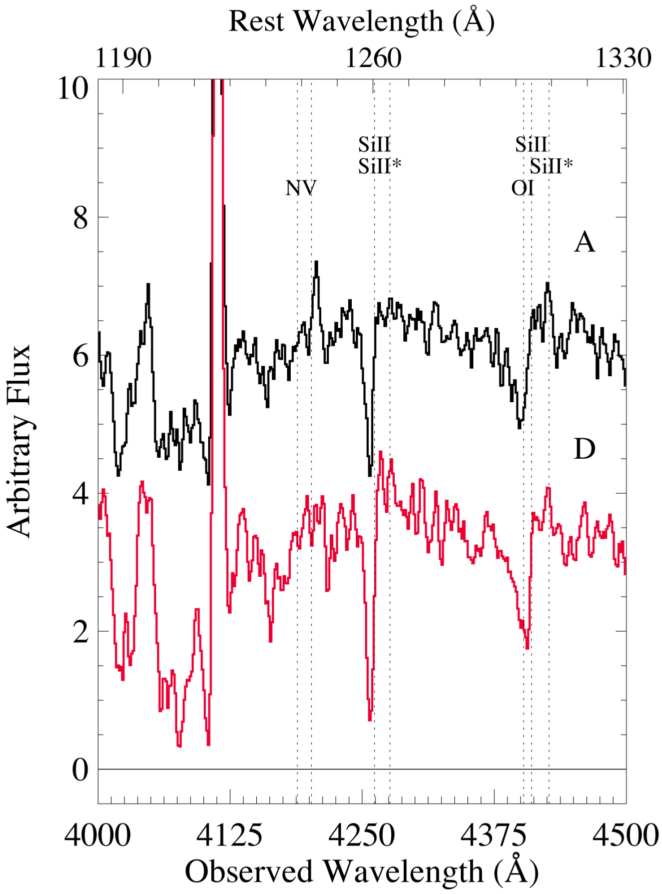

Figure 8.7: *Upper and lower spectra of the Cosmic Horseshoe in the vicinity of the N* V *line. Emission is clearly detected in the upper spectrum at* ∼ 1244*Å, while it is absent in the lower spectrum.*

V λ1238.8,1242.8 feature, which is not clearly resolved. N V is often found in LBGs with a P-Cygni profile (e.g. cB58, Pettini et al. (2000)). Strong P-Cygni lines of N V and C IV λ1549 are formed in the expanding winds of the most luminous O and B stars, and are formed within ∼10 Myrs of the most recent burst of star formation. As the P-Cygni profile of C IV λ1549 is present in the spectrum (Figure 8.8), it would seem plausible that the emission line in the upper spectrum at $\lambda \sim$ 1244Å is a redshifted component of the emission part of a N V P Cygni line, but we see no evidence for a corresponding absorption part of such a profile. There is the possibility of contamination of the N V λ1238.8,1242.8 feature by N IV λ1240 in emission, and if this line is present, its contribution may be cancelling out the absorbing part of the N V λ1238.8,1242.8 feature, leaving only an emitting part. The fact that this emission line is only present in one of the two apertures is puzzling. Quider et al. (2009) examine the same two bright knots of the galaxy (albeit with the position angle of their slit at a slightly different orientation) and find no variation in the two spectra. However, they do find that the flux in clump D is brighter than that of clump A by a factor of 1.19, while these data show that factor to be 1.52, indicating that the two sets of observations cover slightly different parts of the galaxy. Dye et al. (2008) find that the two knots A and D are due to the same object in the source plane. They do note however that the knot A may include a small contribution from the fainter component $\sim$ $0\farcs7$ to the North. They suggest that the multiple surface brightness peaks may be an indicator of substructure in the source plane, and it is possible that this substructure is responsible for the variation in the Lyα and N V lines between the two spectra. Unfortunately, Quider et al. (2009) do not provide a plot of this region of their spectrum for comparison.

Figure 8.8 shows the P Cygni profile of the C IV $\lambda\lambda$1548.204,1550.781 doublet. This feature is also detected in the spectrum of cB58 (Pettini et al. 2000), and can be an indicator of the metallicity of the system, as well as an indicator of recent star formation, as it is formed due to massive short-lived O stars with masses greater than $50M_{\odot}$(Leitherer et al. 1995). Quider et al. (2009) use this line in conjunction with continuous star formation models to deduce a metallicity of approximately half solar. The spectrum of Quider et al. (2009) shows 21 interstelllar absorption lines, with absorption from -800km s^{-1} to +250km s^{-1} across all of these with little variation. In this spectrum, the Al II λ1670.79 line shows a identical velocity width to that found by Quider et al. (2009), but some of the other low-ionisation interstellar lines show slightly higher velocities. Si II λ1526 extends to -1000km s^{-1} in the blueshifted direction, with the redshifted component consistent with +250km s^{-1}. Both C II λ1334 and Si II λ1260 also reach -1000km s^{-1} in the blueshifted direction, and reach +400km s^{-1} and +500km s^{-1} respectively in the redshifted direction. The nature and location of the redshifted gas is unexplained.

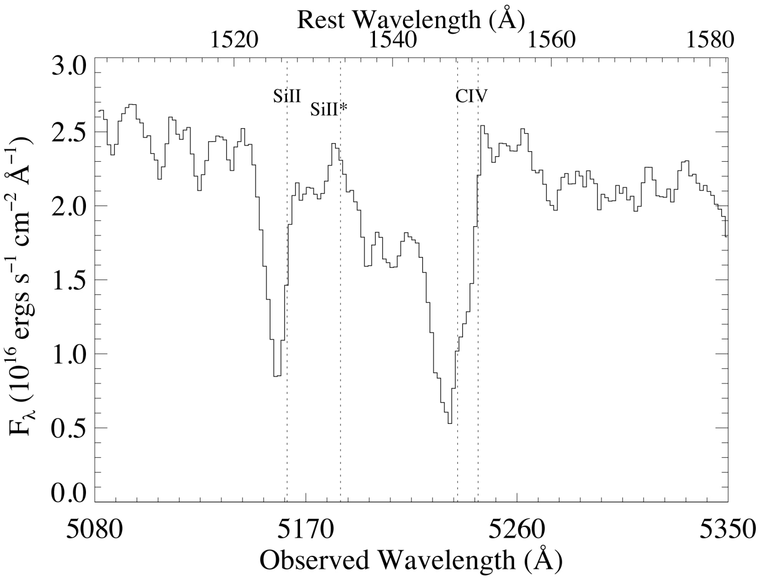

Figure 8.8: *Region of the spectrum containing the C* IV *$\lambda\lambda$1548.204, 1550.781 P-Cygni wind profile. The dotted vertical line at rest frame wavelength λ1533.4312 indicates the Si* II* *nebular emission, and the blueshifted interstellar absorption line of Si* II *λ1526.707 is also evident.*

8.3 Results of VLT Observations of Einstein Ring ER 0047 -2808

The Einstein Ring ER 0047 -2808 was serendipitously discovered by Warren et al. (1996) due to an anomalous emission line at $\lambda \sim 5588$Å superposed on the spectrum of an extremely red early-type galaxy at $z = 0.485$. The subsequent discovery of the [O II] $\lambda\lambda$4959, 5007 lines at $\sim 2.3\mu m$ (Warren et al. 1998) confirmed that the initial emission line was Lyα at a redshift of $z = 3.595$. Imaging data revealed the Einstein ring shape of the system (Warren et al. 1999). The system has subsequently been the subject of multiple studies, the majority of which have focused on the lensing geometry of the system rather than the properties of the source galaxy. Brewer and Lewis (2006) give a value for the overall magnification of 17.9±1.7. Wayth et al. (2005), Dye and Warren (2005) and Brewer and Lewis (2006) find that the reconstruction of the source plane indicates that the galaxy is made up of two distinct components, possibly indicative of a pair of galaxies in the midst of a merger. Wayth et al. (2005) find that the two components have approximately equal brightness, but that one component is larger, and this is the object which lies directly on a fold caustic and is imaged into the large arc part of the ring. An image of the source

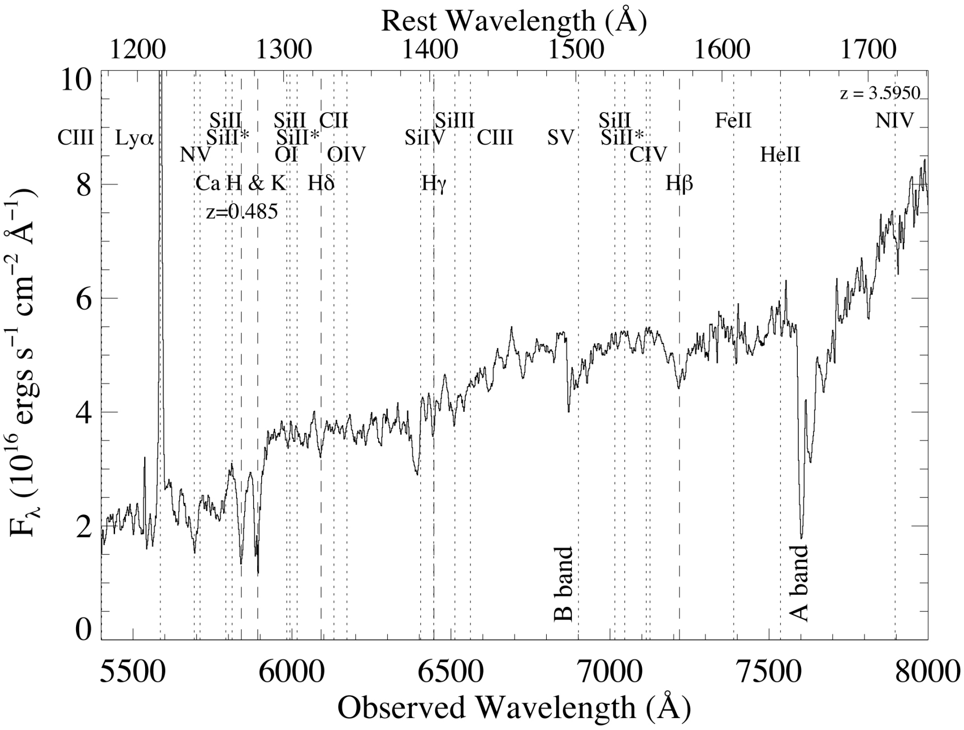

Figure 8.9: *Combined spectrum of the Einstein Ring galaxy ER 0047 -2808 at z = 3.595. There is significant contamination of this lensed galaxy spectrum due to the lensing galaxy. The expected location of features intrinsic to the galaxy are marked with vertical dotted lines, while the location of the strongest features intrinsic to the z = 0.485 lensing galaxy are marked with vertical dashed lines.*

is shown in Figure 8.10, reproduced from Figure 2 of Dye and Warren (2005), which is an interlaced image taken with the HST WFC F555W filter, which covers the wavelength of the strong Lyα emission. The smaller component of the binary system in the source plane is imaged as the smaller knot located towards the upper left corner in this image.

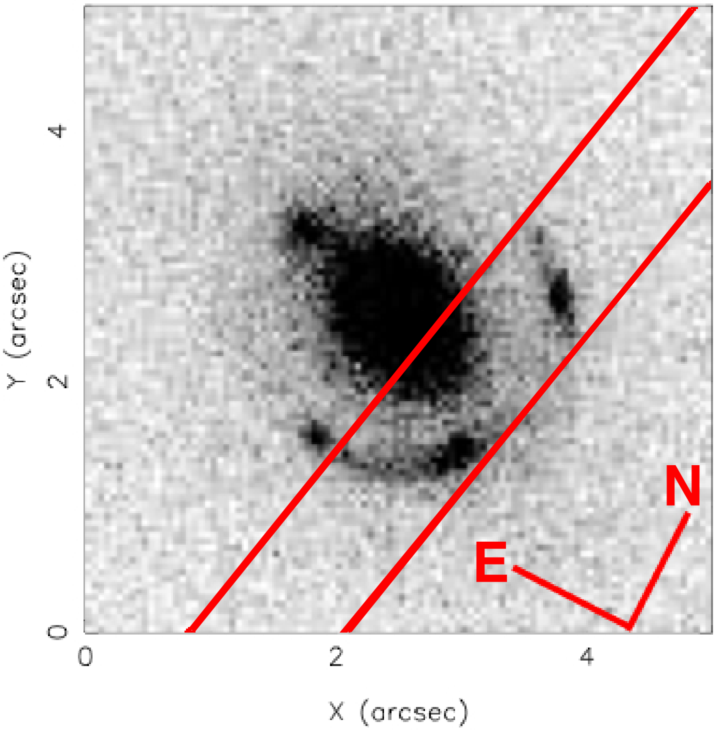

Figure 8.10: *HST Image of Einstein Ring ER 0047 -2808 reproduced from Dye and Warren (2005). In this figure, the vertical axis is at a position angle of* $27\overset{\circ}{.}44$ *east of north. The compass and the location of the slit for these observations have been added to this image for clarity.*

Figure 8.9 shows the spectrum extracted from 5.445 hours of VLT observations as described in Section 3.1.5. Unfortunately, this dataset suffers from a multitude of problems. The primary issue is that this spectrum of the Einstein Ring ER 0047 -2808 is highly contaminated by the lensing galaxy at $z = 0.485$ due to the location of the slit across both the lens and the lensed galaxy. The Ca H & K $\lambda\lambda$3933,3968 lines from the lensing galaxy are prominent in Figure 8.9, as are Hβ, Hγ and Hδ. The region of the spectrum close to the Ca H & K lines is close to the 4000Å break, which is large in old, metal rich galaxies due to the build up of a large number of high-opacity absorption lines from ionised

metals. These lines are likely to be present in the spectrum of an elliptical galaxy like the central lens. Secondly, the wavelength range of these observations means that there is also contamination from the atmospheric A and B bands at ∼6875Å and ∼7600Å respectively. A final issue is the fact that Lyα line is detected very close to the red side of the prominent skyline at λ5577Å, and it is likely that some of the blue side of Lyα may be covered by the skyline, meaning the background subtraction of the skyline will have caused some of the Lyα flux to be removed, and only lower limit measurements can be made from this line.
The possible stellar features which would be normally be available to calculate the systemic redshift are ruled out in this case: stellar lines C II + N III which have a central wavelength of 1324.418Å are contaminated by Hδ from the lensing galaxy; S V λ1501 cannot be identified as it falls at an observed wavelength of ∼6897 close to the region of the spectrum affected by the B band, and O IV λ1343 or N IV λ1718 cannot be detected above the noise. Unfortunately almost all of the lines which appear as possible genuine absorption features in the spectrum of the Einstein ring are also explained by the central galaxy. In order to examine the extent of this contamination, the spectrum was compared with the template galaxies provided by the BC03 model suite which were originally presented in Tremonti et al. (2004). An excellent fit to the spectrum is found using a template with solar metallicity, a simple stellar population formed in a single burst, and an age of 11 Gyrs. This template was scaled to match the observed spectrum, and is overlaid in red in Figure 8.11.

No high S/N spectrum of this lensed Einstein ring galaxy exists in the literature, and while these observations cannot provide any insight into the conditions in the galaxy due to the contamination, further observations of this galaxy are recommended, with a slit positioned so as to avoid any contribution to the light from the lensing galaxy. The majority of the lensed LBGs studied thus far have been examples of single galaxies with large-scale outflows. The presence of a dual component in this lensed galaxy could allow a rare glimpse at a merging or interacting pair of LBGs, if the light from the source and the lensing galaxy can be sufficiently disentangled.

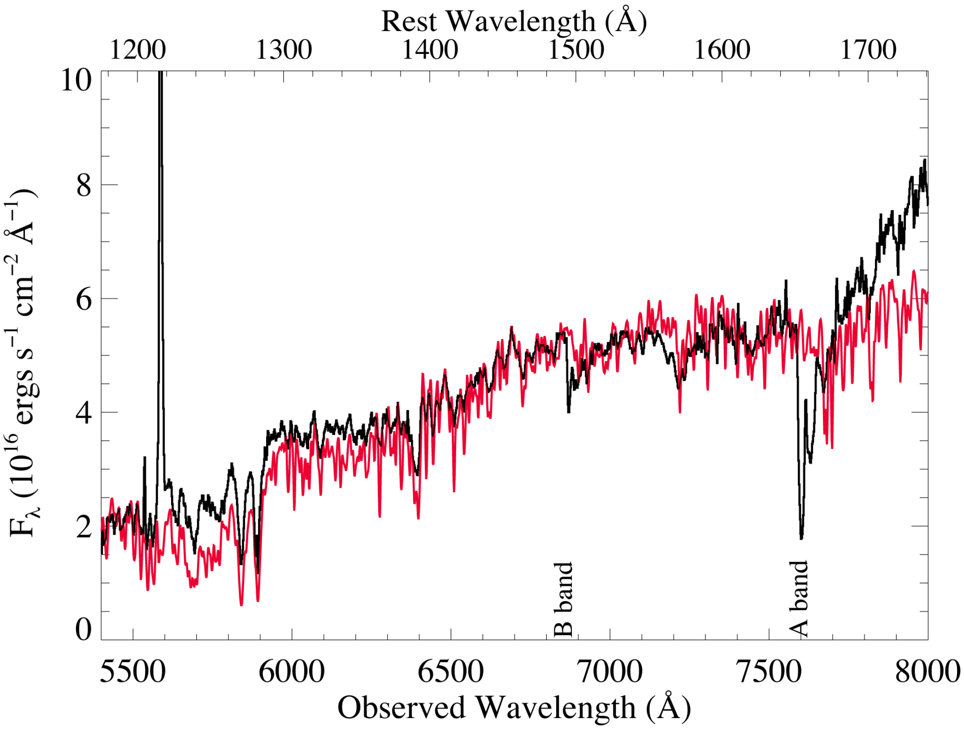

Figure 8.11: *Spectrum of the Einstein Ring system. The spectrum overlaid in red is a template from the BC03 model suite, which is a simple stellar population with an age of 11 Gyrs and a metallicity of* $Z_\odot$. *The template has been scaled by* 6×10^{-16} *and shifted to a redshift of* $z = 0.485$, *and matches the observed spectrum extremely well, indicating the dominance of the central lensing elliptical galaxy.*

9

Conclusions and Future Prospects

The overarching aim of this work is to use these studies of the kinematics and physical characteristics of galaxies as a starting point to understand galaxy formation and dynamics, from the development of ordered rotation in disks to the emergence of the Hubble sequence of galaxy types. A parallel aim is to use the redshifts of strongly-lensed samples to constrain total mass models of the luminous plus dark matter contained in the lenses, thus contributing towards furthering our understanding of the nature of dark matter. Observations of distant galaxies afford us an instantaneous snapshot of the past, since due to the cosmological stretching of photons we are observing such galaxies as they were when these photons left them. This means that although we can observe galaxies over a wide range in redshift, it is impossible to chart the evolution and fate of high-redshift galaxies and their direct descendants in the local Universe. While such fundamental questions remain unanswered in the field of galactic evolution, the acquisition and study of new observations will remain central to addressing these issues. This thesis has presented spectroscopic studies of a number of galaxies and the findings of each individual chapter are summarised below:

Chapter 4:
This chapter outlines the specific steps involved in reducing the spectroscopic data obtained from the observations described in the preceding chapter. This is a complete code in the IDL language, which was originally written for use with a ground-based redshift survey (Frye et al. 2007), but to which I introduced a number of modifications and specialised routines. For huge datasets such as the SDSS, data reduction without an automated pipeline would be unfeasible, while telescope pipelines provide a method for "quick-look" in-

spection of data, which can be useful during an observing run. However, the data reduction process described in Chapter 4 has a number of advantages over automated reduction techniques, particularly for reducing the faint spectra acquired from distant galaxies. Generating the final one-dimensional spectrum from the original raw data output by the telescope CCD involves a number of steps. As the code I have built up is separated out into clear procedures to carry out each of these processes, I have acquired a deep understanding of what I need the code to do in each step, and am able to introduce solutions to deal with any unexpected characteristics of a particular dataset, or any variation in the output from one telescope to another. This allows for the extraction of the optimum spectrum from all datasets.

Chapter 5:

The spectrum of the galaxy A1689-7.1 at $z = 4.87$ reveals strong Lyα emission which is similar to that seen at lower redshifts ($z \sim 2 - 3$, e.g. Shapley et al. (2003)). Blueshifted absorption lines are also present, which in combination with the asymmetric Lyα line indicate an outflow of interstellar material into the surrounding IGM. SED modelling reveals a small, dust-free galaxy, which has a relatively evolved stellar population, with the presence of a Balmer break ruling out timescales less than 100 Myrs since the onset of star formation. Star formation rates are found to be $\sim 6 - 11 M_{\odot}$ yr^{-1}.

The most important result gleaned from this data comes from the fact that due to lensing, we are able to measure for the first time the Gunn-Peterson effective optical depth towards a galaxy. As a result, an overdensity of H I in the IGM was discovered in this location. This novel measurement has a promising future. Subsequent studies based on this result (Matsuda et al. 2010) have revealed an overdensity of galaxies close to A1689-7.1, suggesting that such H I-rich locations in the IGM may also be prime locations for the formation of protoclusters. The Sloan Digital Sky Survey (SDSS) has a vast public archive containing the spectra of thousands of QSOs. A significant fraction of those at $z \sim 1 - 2$ are bright enough also to measure τ_{eff}^{GP} along the line of sight and outside of the proximity zone. Such a survey will reveal whether IGM overdensities exist at intermediate redshifts, and allow for a search for further correlations between IGM overdensity and protocluster formation.

Chapter 6:
Slitless grism spectroscopy proves to be an effective method of simultaneously observing a large number of sources with no prior selection constraints. The results presented in this chapter have been acquired with a relatively low expenditure of observing time, 3 orbits of HST. Galaxy cluster fields have not previously been targeted for grism studies, perhaps owing to the crowded nature of such a field, which could potentially increase problems due to overlapping spectral orders. However, the results presented here (and in Hurley et al. (2011), in prep) show that targeting a cluster field can yield a similarly-sized sample as an equally deep survey in the Hubble Deep Field North (Meurer et al. 2007). In addition, the cluster field detects both cluster members and background galaxies simultaneously. Abell 1689 is an extremely well studied cluster due to its large Einstein radius of $\sim 50\farcs0$ and hence its huge lensing potential. However, many other less famous clusters are known out to redshifts of $\sim$ 1.9 (cluster JKCS 041, Andreon et al. (2009)). With a modest amount of HST exposure time, a cluster and any lensed background sources could be surveyed in grism mode, while complementary imaging in two or more filters could allow for colour-selection, increasing the likelihood of solid redshift determinations of distant galaxies such as the one at $z = 5.13$ found in this survey. Pirzkal et al. (2007) have used this technique effectively to detect nine Lyα emitting galaxies in the Hubble Ultra Deep Field, and the added advantage of strong lensing should make the detection of such objects in further clusters fields a distinct possibility. The high spatial resolution of the grism is its primary advantage over other observing modes. Among the sources displaying multiple emission line sources in this survey, we focus on a single strongly-lensed arc at $z = 0.79$ containing three individual star-forming regions, each displaying strong [O II] and [O III] emission lines.

Chapter 7:
Spatially resolved spectroscopy at $z = 1$ is relatively rare, and as a galaxy class, spectroscopy of objects at $z \sim 1$ is woefully incomplete. From the spectroscopy of a $z = 0.79$ galaxy, although very low signal-to-noise, there is evidence that the line profiles of the emission lines vary in relative intensity and equivalent width across the long axis of the arc. These lines encode valuable information about the galaxy class, metallicity and star formation rates. Smaller equivalent width in the galaxy interior is suggestive of inside-out formation. This finding

is complemented by the observation of a gradient in the [Ne III]/[O II] ratio which is indicative of a metallicity gradient also consistent with inside-out formation. The future of this study is to obtain spatially-resolved spectroscopy in the near-IR to obtain what remains the most important star formation diagnostic, the hydrogen Balmer Hα line at rest wavelength 6563Å, along with the [N II] and [Si II] lines which lie close in wavelength space to Hα. Obtaining further observations of the $z = 0.79$ galaxy at near-infrared wavelengths using an integral field spectrograph would be a natural next step to explore this galaxy further. This would allow us to directly probe the star formation and any possible AGN activity using the Hα line. The three-dimensional nature of integral field spectroscopy means that such observations would allow one to study the dynamics of the galaxy as a whole, constrain the dynamical mass of the galaxy from the Hα line width, and to map the star formation over the spatial extent of the arc, potentially verifying the inside-out formation hinted at in the results of this chapter.

Understanding the contribution to the H I ionising background from star-forming galaxies is crucial to solving the puzzle of galaxy assembly. The census of high-z quasars shows a dropping off in their space densities towards the highest redshifts, indicating that there are too few of them at the highest redshift to be the primary source of ionising photons for the reionisation of the Universe. This indicates that star-forming galaxies must have also played a significant role in the provision of ionising emission. It is still unclear what fraction of ionising photons can bypass the expected absorption by high column density neutral gas surrounding star-forming regions and escape into the IGM. This escape fraction f_{esc} is related to the ratio of flux levels between rest frame 1500Å and the Lyman-continuum (LyC, $\lambda < 912$Å). The search for f_{esc} at high redshift has produced varying results thus far- Steidel et al. (2001) report that for their sample of 29 LBGs at $z \sim 3.4$, the majority of the LyC photons are escaping into the IGM, while Shapley et al. (2006) find low relative escape fractions of $f_{esc} < 0.25$ for a deeper LBG sample. Iwata et al. (2009) find large escape fractions for $\sim 10\%$ of their sample of 198 LBGs and Lyα-emitters at $z \sim 3$. However, no conclusive detection has been made for any escaping photons in searches at redshifts $0 < z < 1.5$ (Siana et al. 2010; Cowie et al. 2009). The galaxy studied here at $z = 0.79$ appears to be a bright young starburst with a mass and metallicity similar to those of the LBG population. If the same amount of ionising photons are produced by its massive stars as are produced in LBGs at higher redshifts, a similar escape fraction should be observable. Siana et al. (2010) suggest that, due to the lack of detections of LyC photons, the ionising emissivity of $z \sim 1$ galaxies must be lower than that of galaxies of comparable luminosity at $z \sim 3$. The boost in brightness of lensed galaxies at $z \sim 1$ would make this population an excellent target for further searches for LyC photons. If a detection could be made, the extended nature of lensed sources such as the giant arc studied in Chapter 7 could also in theory allow a determination of the exact location of the escaping photons from the galaxy, depending on the lensing model. The availability of complementary spectra such as that shown in Chapter 7 could help to identify differences between galaxies with similar stellar populations at low and high redshifts in order to probe the cause for any decline in ionising emissivity between the two epochs.

Chapter 8:

The existing sample of strongly-lensed LBGs at $z \sim 2-3$ (<20) is a very small subset of a massive and varied population. The variation in the spectra of such galaxies is shown by Shapley et al. (2003) and is achieved through the coaddition of a large number of low-resolution spectra of non-lensed galaxies. The low number of known strongly-lensed galaxies at $z \sim 2-3$ make these new observations of the Cosmic Horseshoe relatively important. This study in combination with the others in the literature has led to the important results that starbursting galaxies at high redshift have high star formation rates and large interstellar pressures that drive powerful gaseous outflows. Additional data on the LBG population is very valuable and gives us the best information regarding the kinematics and physical processes that govern the physics of young galaxies. Further work on the Cosmic Horseshoe and the Einstein Ring ER 0047 -2808 would be to utilise the SED modelling process discussed in Chapters 5 and 7 to determine some of the galaxy properties. Results from such modelling could provide a useful step toward disentangling the properties of ER 0047 -2808 from the nearby elliptical galaxies in further observations of this relatively-unstudied galaxy at $z = 3.6$, which is also possibly a rare example of a merging or dual component LBG.

In closing, this thesis has concerned the evolution of galaxies in the Universe, a fundamental question in astrophysics. The studies have included observations of gravitationally-lensed but otherwise ordinary star forming galaxies over a broad redshift range, $z = 1 - 5$, and has concentrated on the study of the physical processes at work in individual objects. The observations were reduced with custom-built code designed to maximize the signal-to-noise, and with the addition of methods to follow the flexure-induced curvature of the 2d spectroscopic images and to optimally-extract the data. At $z \sim 1$ it was discovered that the line widths and equivalent widths of the Balmer emission lines, and the metallicity all decrease towards the galaxy center, lending support to the inside-out model of galaxy formation. Follow-up work would be critical to improving our understanding the galaxy-scale kinematics of this object. In a galaxy at z=4.9 the first discovery of an IGM overdensity was made. The discovery of additional IGM overdensities will be important to the field of extragalactic astronomy if such regions are found to be the sites of newly-forming galaxy clusters. All of this will be valuable ground work in preparation for observations with the advent of the joint European-U. S. James Webb Space Telescope (JWST), of which Ireland is a **full** member. This pioneering new facility will mean that the high redshift Universe will become accessible as never before, increasing our horizons by probing the near-infrared wavelengths with ultra-deep surveys. JWST is expected to be able to observe all the way back in time to $z \sim 20$, less than 200 million years after the Big Bang.

Bibliography

K. L. Adelberger, C. C. Steidel, A. E. Shapley, and M. Pettini. Galaxies and Intergalactic Matter at Redshift z∼3: Overview. *Astrophysical Journal*, 584: 45–75, February 2003. 50, 53

S. S. Allam, D. L. Tucker, H. Lin, H. T. Diehl, J. Annis, E. J. Buckley-Geer, and J. A. Frieman. The 8 o'clock Arc: A Serendipitous Discovery of a Strongly Lensed Lyman Break Galaxy in the SDSS DR4 Imaging Data. *ArXiv Astrophysics e-prints*, pages 11138–+, November 2006. 121

C. Allende Prieto, D. L. Lambert, and M. Asplund. The Forbidden Abundance of Oxygen in the Sun. *Astrophysical Journal*, 556:L63–L66, July 2001. 100

S. Andreon, B. Maughan, G. Trinchieri, and J. Kurk. JKCS 041: a colour-detected galaxy cluster at $z_{phot} \sim 1.9$ with deep potential well as confirmed by X-ray data. *A&A*, 507:147–157, November 2009. 138

H. Atek, D. Kunth, M. Hayes, G. Östlin, and J. M. Mas-Hesse. On the detectability of Lyα emission in star forming galaxies. The role of dust. *A&A*, 488:491–509, September 2008. 62

S. Bajtlik, R. C. Duncan, and J. P. Ostriker. Quasar ionization of Lyman-alpha clouds - The proximity effect, a probe of the ultraviolet background at high redshift. *Astrophysical Journal*, 327:570–583, April 1988. 48

J. A. Baldwin, M. M. Phillips, and R. Terlevich. Classification parameters for the emission-line spectra of extragalactic objects. *PASP*, 93:5–19, February 1981. 97

M. L. Balogh, S. L. Morris, H. K. C. Yee, R. G. Carlberg, and E. Ellingson. Differential Galaxy Evolution in Cluster and Field Galaxies at z∼0.3. *Astrophysical Journal*, 527:54–79, December 1999. 91

M. L. Balogh, W. J. Couch, I. Smail, R. G. Bower, and K. Glazebrook. An Hα survey of the rich cluster A 1689. *Mon. Not. R. A. S.*, 335:10–22, September 2002. 65, 68, 70, 71, 72

G. D. Becker, M. Rauch, and W. L. W. Sargent. The Evolution of Optical Depth in the Lyα Forest: Evidence Against Reionization at z∼6. *Astrophysical Journal*, 662:72–93, June 2007. doi: 10.1086/517866. 3, 51, 52, 54

R. H. Becker, X. Fan, R. L. White, M. A. Strauss, V. K. Narayanan, R. H. Lupton, J. E. Gunn, J. Annis, N. A. Bahcall, J. Brinkmann, A. J. Connolly, I. Csabai, P. C. Czarapata, M. Doi, T. M. Heckman, G. S. Hennessy, Ž. Ivezić, G. R. Knapp, D. Q. Lamb, T. A. McKay, J. A. Munn, T. Nash, R. Nichol, J. R. Pier, G. T. Richards, D. P. Schneider, C. Stoughton, A. S. Szalay, A. R. Thakar, and D. G. York. Evidence for Reionization at z$\sim$6: Detection of a Gunn-Peterson Trough in a z=6.28 Quasar. *Astronomical Journal*, 122:2850–2857, December 2001. 49

V. Belokurov, N. W. Evans, A. Moiseev, L. J. King, P. C. Hewett, M. Pettini, L. Wyrzykowski, R. G. McMahon, M. C. Smith, G. Gilmore, S. F. Sanchez, A. Udalski, S. Koposov, D. B. Zucker, and C. J. Walcher. The Cosmic Horseshoe: Discovery of an Einstein Ring around a Giant Luminous Red Galaxy. *Astrophysical Journal*, 671:L9–L12, December 2007. 26, 125

E. Berger, B. E. Penprase, S. B. Cenko, S. R. Kulkarni, D. B. Fox, C. C. Steidel, and N. A. Reddy. Spectroscopy of GRB 050505 at z = 4.275: A logN(H I) = 22.1 DLA Host Galaxy and the Nature of the Progenitor. *Astrophysical Journal*, 642:979–988, May 2006. 53

Y. Birnboim and A. Dekel. Virial shocks in galactic haloes? *Mon. Not. R. A. S.*, 345:349–364, October 2003. 54

R. D. Blandford and R. Narayan. Cosmological applications of gravitational lensing. *ARA&A*, 30:311–358, 1992. 10

R. J. Bouwens, G. D. Illingworth, P. A. Oesch, M. Stiavelli, P. van Dokkum, M. Trenti, D. Magee, I. Labbé, M. Franx, C. M. Carollo, and V. Gonzalez. Discovery of z $\sim$ 8 Galaxies in the Hubble Ultra Deep Field from Ultra-Deep WFC3/IR Observations. *Astrophysical Journal*, 709:L133–L137, February 2010. 6

B. J. Brewer and G. F. Lewis. The Einstein Ring 0047-2808 Revisited: A Bayesian Inversion. *Astrophysical Journal*, 651:8–13, November 2006. 131

T. Broadhurst, N. Benítez, D. Coe, K. Sharon, K. Zekser, R. White, H. Ford, R. Bouwens, J. Blakeslee, M. Clampin, N. Cross, M. Franx, B. Frye, G. Hartig, G. Illingworth, L. Infante, F. Menanteau, G. Meurer, M. Postman, D. R. Ardila, F. Bartko, R. A. Brown, C. J. Burrows, E. S. Cheng, P. D. Feldman, D. A. Golimowski, T. Goto, C. Gronwall, D. Herranz, B. Holden,

N. Homeier, J. E. Krist, M. P. Lesser, A. R. Martel, G. K. Miley, P. Rosati, M. Sirianni, W. B. Sparks, S. Steindling, H. D. Tran, Z. I. Tsvetanov, and W. Zheng. Strong-Lensing Analysis of A1689 from Deep Advanced Camera Images. *Astrophysical Journal*, 621:53–88, March 2005. 14, 17, 22, 44, 56

A. G. Bruzual. Spectral evolution of galaxies. I - Early-type systems. *Astrophysical Journal*, 273:105–127, October 1983. 91

G. Bruzual and S. Charlot. Stellar population synthesis at the resolution of 2003. *Mon. Not. R. A. S.*, 344:1000–1028, October 2003. 8, 44, 55, 90, 123

W. L. Burke. Multiple Gravitational Imaging by Distributed Masses. *Astrophysical Journal*, 244:L1+, February 1981. 13

D. Calzetti. The Dust Opacity of Star-forming Galaxies. *PASP*, 113:1449–1485, December 2001. 96

D. Calzetti, L. Armus, R. C. Bohlin, A. L. Kinney, J. Koornneef, and T. Storchi-Bergmann. The Dust Content and Opacity of Actively Star-forming Galaxies. *Astrophysical Journal*, 533:682–695, April 2000. 57, 96

R. F. Carswell, J. A. J. Whelan, M. G. Smith, A. Boksenberg, and D. Tytler. Observations of the spectra of Q0122-380 and Q1101-264. *Mon. Not. R. A. S.*, 198:91–110, January 1982. 48

W. Cash. Generation of Confidence Intervals for Model Parameters in X-ray Astronomy. *A&A*, 52:307–+, October 1976. 59, 60

G. Chabrier. Galactic Stellar and Substellar Initial Mass Function. *PASP*, 115:763–795, July 2003. 57, 93

S. Charlot and M. Longhetti. Nebular emission from star-forming galaxies. *Mon. Not. R. A. S.*, 323:887–903, May 2001. 102, 106

D. Coe, N. Benitez, T. Broadhurst, L. Moustakas, and H. Ford. The Highest Resolution Mass Map of Galaxy Cluster Substructure To Date Without Assuming Light Traces Mass: LensPerfect Analysis of Abell 1689. *ArXiv e-prints*, May 2010. 14

D. A. Coe, N. Benitez, T. J. Broadhurst, K. C. Zekser, R. L. White, B. Frye, H. C. Ford, G. D. Illingworth, and ACS Science Team. Bayesian Photometric Redshift Analysis of Deep ACS and Ground-based Imaging of Abell 1689.

In *Bulletin of the American Astronomical Society*, volume 35 of *Bulletin of the American Astronomical Society*, pages 1407–+, December 2003. 56, 65

L. L. Cowie, A. J. Barger, and L. Trouille. Measuring the Sources of the Intergalactic Ionizing Flux. *Astrophysical Journal*, 692:1476–1488, February 2009. 139

M. Davis, S. M. Faber, J. Newman, A. C. Phillips, R. S. Ellis, C. C. Steidel, C. Conselice, A. L. Coil, D. P. Finkbeiner, D. C. Koo, P. Guhathakurta, B. Weiner, R. Schiavon, C. Willmer, N. Kaiser, G. A. Luppino, G. Wirth, A. Connolly, P. Eisenhardt, M. Cooper, and B. Gerke. Science Objectives and Early Results of the DEEP2 Redshift Survey. In P. Guhathakurta, editor, *Society of Photo-Optical Instrumentation Engineers (SPIE) Conference Series*, volume 4834 of *Presented at the Society of Photo-Optical Instrumentation Engineers (SPIE) Conference*, pages 161–172, February 2003. 41

G. De Lucia, V. Springel, S. D. M. White, D. Croton, and G. Kauffmann. The formation history of elliptical galaxies. *Mon. Not. R. A. S.*, 366:499–509, February 2006. 5

A. Dekel and Y. Birnboim. Galaxy bimodality due to cold flows and shock heating. *Mon. Not. R. A. S.*, 368:2–20, May 2006. 4

C. C. Dow-Hygelund, B. P. Holden, R. J. Bouwens, A. van der Wel, G. D. Illingworth, A. Zirm, M. Franx, P. Rosati, H. Ford, P. G. van Dokkum, S. A. Stanford, P. Eisenhardt, and G. G. Fazio. UV Continuum Spectroscopy of a $6L_*$ z = 5.5 Starburst Galaxy,. *"Astrophys. J. Lett."*, 630:L137–L140, September 2005. 53

A. Dressler. The Evolution of Galaxies in Clusters. *ARA&A*, 22:185–222, 1984. 21

A. Dressler, T. Hare, B. C. Bigelow, and D. J. Osip. IMACS: the wide-field imaging spectrograph on Magellan-Baade. In *Society of Photo-Optical Instrumentation Engineers (SPIE) Conference Series*, volume 6269 of *Society of Photo-Optical Instrumentation Engineers (SPIE) Conference Series*, July 2006. 23

P.-A. Duc, B. M. Poggianti, D. Fadda, D. Elbaz, H. Flores, P. Chanial, A. Franceschini, A. Moorwood, and C. Cesarsky. Hidden star-formation in the cluster of galaxies Abell 1689. *A&A*, 382:60–83, January 2002. 22, 65, 68, 70, 71, 77, 82, 83

S. Dye and S. J. Warren. Decomposition of the Visible and Dark Matter in the Einstein Ring 0047-2808 by Semilinear Inversion. *Astrophysical Journal*, 623:31–41, April 2005. vi, 131, 133

S. Dye, N. W. Evans, V. Belokurov, S. J. Warren, and P. Hewett. Models of the Cosmic Horseshoe gravitational lens J1004+4112. *Mon. Not. R. A. S.*, 388:384–392, July 2008. 126, 130

E. Egami, G. H. Rieke, J. R. Rigby, C. Papovich, J.-P. Kneib, G. P. Smith, E. Le Floc'h, K. A. Misselt, P. G. Peréz-González, J.-S. Huang, H. Dole, and D. T. Frayer. The Spitzer Massive Lensing Cluster Survey. In L. Armus and W. T. Reach, editors, *Astronomical Society of the Pacific Conference Series*, volume 357 of *Astronomical Society of the Pacific Conference Series*, pages 242–+, December 2006. 56

E. Ellingson. Galaxy evolution in clusters. *Ap&SS*, 285:9–18, 2003. doi: 10.1023/A:1024641221686. 21

R. S. Ellis, M. Colless, T. Broadhurst, J. Heyl, and K. Glazebrook. Autofib redshift survey - i. evolution of the galaxy luminosity function. *Mon. Not. R. A. S.*, 280:235–251, May 1996. 116

D. K. Erb, M. Pettini, A. E. Shapley, C. C. Steidel, D. R. Law, and N. A. Reddy. Physical Conditions in a Young, Unreddened, Low-metallicity Galaxy at High Redshift. *Astrophysical Journal*, 719:1168–1190, August 2010. 47

L. P. Eyles, A. J. Bunker, E. R. Stanway, M. Lacy, R. S. Ellis, and M. Doherty. Spitzer imaging of i'-drop galaxies: old stars at z$\sim$ 6. *Mon. Not. R. A. S.*, 364:443–454, December 2005. 6

S. M. Faber, A. C. Phillips, R. I. Kibrick, B. Alcott, S. L. Allen, J. Burrous, T. Cantrall, D. Clarke, A. L. Coil, D. J. Cowley, M. Davis, W. T. S. Deich, K. Dietsch, D. K. Gilmore, C. A. Harper, D. F. Hilyard, J. P. Lewis, M. McVeigh, J. Newman, J. Osborne, R. Schiavon, R. J. Stover, D. Tucker, V. Wallace, M. Wei, G. Wirth, and C. A. Wright. The DEIMOS spectrograph for the Keck II Telescope: integration and testing. In M. Iye &

A. F. M. Moorwood, editor, *Society of Photo-Optical Instrumentation Engineers (SPIE) Conference Series*, volume 4841 of *Society of Photo-Optical Instrumentation Engineers (SPIE) Conference Series*, pages 1657–1669, March 2003. doi: 10.1117/12.460346. 25

X. Fan, V. K. Narayanan, M. A. Strauss, R. L. White, R. H. Becker, L. Pentericci, and H.-W. Rix. Evolution of the Ionizing Background and the Epoch of Reionization from the Spectra of z$\sim$6 Quasars. *Astronomical Journal*, 123: 1247–1257, March 2002. 49

X. Fan, M. A. Strauss, R. H. Becker, R. L. White, J. E. Gunn, G. R. Knapp, G. T. Richards, D. P. Schneider, J. Brinkmann, and M. Fukugita. Constraining the Evolution of the Ionizing Background and the Epoch of Reionization with z $\sim$ 6 Quasars. II. A Sample of 19 Quasars. *Astronomical Journal*, 132: 117–136, July 2006. 3, 50, 51, 52, 54

M. Franx, G. D. Illingworth, D. D. Kelson, P. G. van Dokkum, and K.-V. Tran. A Pair of Lensed Galaxies at z=4.92 in the Field of CL 1358+62. *Astrophys. J. Lett.*, 486:L75, 1997. 53

B. Frye, T. Broadhurst, and N. Benítez. Spectral Evidence for Widespread Galaxy Outflows at z $>$ 4. *Astrophysical Journal*, 568:558–575, April 2002. 16, 28, 44, 68, 75, 76, 123

B. L. Frye, D. Coe, D. V. Bowen, N. Benítez, T. Broadhurst, P. Guhathakurta, G. Illingworth, F. Menanteau, K. Sharon, R. Lupton, G. Meylan, K. Zekser, G. Meurer, and M. Hurley. The Sextet Arcs: A Strongly Lensed Lyman Break Galaxy in the ACS Spectroscopic Galaxy Survey toward Abell 1689. *Astrophysical Journal*, 665:921–935, August 2007. 44, 61, 65, 68, 71, 121, 136

B. L. Frye, D. V. Bowen, M. Hurley, T. M. Tripp, X. Fan, B. Holden, P. Guhathakurta, D. Coe, T. Broadhurst, E. Egami, and G. Meylan. Observations of the Gas Reservoir around a Star-Forming Galaxy in the Early Universe. *Astrophysical Journal*, 685:L5–L8, September 2008. 19, 44, 55

R. M. González Delgado, C. Leitherer, and T. M. Heckman. Synthetic Spectra of H Balmer and HE I Absorption Lines. II. Evolutionary Synthesis Models for Starburst and Poststarburst Galaxies. *ApJS*, 125:489–509, December 1999. 95

R. Guimarães, P. Petitjean, E. Rollinde, R. R. de Carvalho, S. G. Djorgovski, R. Srianand, A. Aghaee, and S. Castro. Evidence for overdensity around $z_{em} > 4$ quasars from the proximity effect. *Mon. Not. R. A. S.*, 377:657–666, May 2007. 53

J. E. Gunn and B. A. Peterson. On the Density of Neutral Hydrogen in Intergalactic Space. *Astrophysical Journal*, 142:1633–1641, November 1965. 49

K. N. Hainline, A. E. Shapley, K. A. Kornei, M. Pettini, E. Buckley-Geer, S. S. Allam, and D. L. Tucker. Rest-Frame Optical Spectra of Three Strongly Lensed Galaxies at z $\sim$ 2. *Astrophysical Journal*, 701:52–65, August 2009. 126

M. Hamuy, N. B. Suntzeff, S. R. Heathcote, A. R. Walker, P. Gigoux, and M. M. Phillips. Southern spectrophotometric standards, 2. *PASP*, 106: 566–589, June 1994. 34, 43

T. M. Heckman. Galactic Superwinds Circa 2001. In J. S. Mulchaey & J. T. Stocke, editor, *Extragalactic Gas at Low Redshift*, volume 254 of *Astronomical Society of the Pacific Conference Series*, pages 292–+, 2002. 47, 125

T. M. Heckman. An optical and radio survey of the nuclei of bright galaxies - Activity in normal galactic nuclei. *A&A*, 87:152–164, July 1980. 97

L. C. Ho, A. V. Filippenko, and W. L. W. Sargent. A Search for “Dwarf” Seyfert Nuclei. III. Spectroscopic Parameters and Properties of the Host Galaxies. *ApJS*, 112:315–+, October 1997. 97

D. W. Hogg, I. K. Baldry, M. R. Blanton, and D. J. Eisenstein. The K correction. *ArXiv Astrophysics e-prints*, October 2002. 61

K. Horne. An optimal extraction algorithm for CCD spectroscopy. *"PASP"*, 98:609–617, June 1986. 34, 36

I. Iwata, A. K. Inoue, Y. Matsuda, H. Furusawa, T. Hayashino, K. Kousai, M. Akiyama, T. Yamada, D. Burgarella, and J.-M. Deharveng. Detections of Lyman Continuum from Star-Forming Galaxies at z $\sim$ 3 through Subaru/Suprime-Cam Narrow-Band Imaging. *Astrophysical Journal*, 692: 1287–1293, February 2009. 4, 139

H. Jabran Zahid, L. J. Kewley, and F. Bresolin. The Mass-Metallicity and Luminosity-Metallicity Relation from DEEP2 at z $\sim$ 0.8. *ArXiv e-prints*, June 2010. vi, 103, 114, 115

T. Jones, R. S. Ellis, E. Jullo, and J. Richard. Measurement of a Metallicity Gradient in a z=2 Galaxy: Implications for Inside-Out Assembly Histories. *ArXiv e-prints*, October 2010. 112

E. Jullo, P. Natarajan, J.-P. Kneib, A. D'Aloisio, M. Limousin, J. Richard, and C. Schimd. Cosmological Constraints from Strong Gravitational Lensing in Clusters of Galaxies. *Science*, 329:924–927, August 2010. 6, 7, 14

N. Kaiser and G. Squires. Mapping the dark matter with weak gravitational lensing. *Astrophysical Journal*, 404:441–450, February 1993. 15

G. Kauffmann, T. M. Heckman, C. Tremonti, J. Brinchmann, S. Charlot, S. D. M. White, S. E. Ridgway, J. Brinkmann, M. Fukugita, P. B. Hall, Ž. Ivezić, G. T. Richards, and D. P. Schneider. The host galaxies of active galactic nuclei. *Mon. Not. R. A. S.*, 346:1055–1077, December 2003a. 91, 98

G. Kauffmann, T. M. Heckman, S. D. M. White, S. Charlot, C. Tremonti, J. Brinchmann, G. Bruzual, E. W. Peng, M. Seibert, M. Bernardi, M. Blanton, J. Brinkmann, F. Castander, I. Csábai, M. Fukugita, Z. Ivezic, J. A. Munn, R. C. Nichol, N. Padmanabhan, A. R. Thakar, D. H. Weinberg, and D. York. Stellar masses and star formation histories for 10^5 galaxies from the Sloan Digital Sky Survey. *Mon. Not. R. A. S.*, 341:33–53, May 2003b. 91

N. Kawai, G. Kosugi, K. Aoki, T. Yamada, T. Totani, K. Ohta, M. Iye, T. Hattori, W. Aoki, H. Furusawa, K. Hurley, K. S. Kawabata, N. Kobayashi, Y. Komiyama, Y. Mizumoto, K. Nomoto, J. Noumaru, R. Ogasawara, R. Sato, K. Sekiguchi, Y. Shirasaki, M. Suzuki, T. Takata, T. Tamagawa, H. Terada, J. Watanabe, Y. Yatsu, and A. Yoshida. An optical spectrum of the afterglow of a γ-ray burst at a redshift of z = 6.295. *"Nature"*, 440: 184–186, March 2006. 53

R. C. Kennicutt, Jr. The integrated spectra of nearby galaxies - General properties and emission-line spectra. *Astrophysical Journal*, 388:310–327, April 1992. 94

R. C. Kennicutt, Jr. Star Formation in Galaxies Along the Hubble Sequence. *ARA&A*, 36:189–232, 1998. 72, 116

R. C. Kennicutt, Jr., F. Bresolin, and D. R. Garnett. The Composition Gradient in M101 Revisited. II. Electron Temperatures and Implications for the Nebular Abundance Scale. *Astrophysical Journal*, 591:801–820, July 2003. 103

D. Kereš, N. Katz, D. H. Weinberg, and R. Davé. How do galaxies get their gas? *Mon. Not. R. A. S.*, 363:2–28, October 2005. 4, 54

L. J. Kewley and M. A. Dopita. Using Strong Lines to Estimate Abundances in Extragalactic H II Regions and Starburst Galaxies. *ApJS*, 142:35–52, September 2002. 88, 102

L. J. Kewley and S. L. Ellison. Metallicity Calibrations and the Mass-Metallicity Relation for Star-forming Galaxies. *Astrophysical Journal*, 681: 1183–1204, July 2008. 102

L. J. Kewley, M. J. Geller, R. A. Jansen, and M. A. Dopita. The Hα and Infrared Star Formation Rates for the Nearby Field Galaxy Survey. *Astronomical Journal*, 124:3135–3143, December 2002. 116

L. J. Kewley, M. J. Geller, and R. A. Jansen. [O II] as a Star Formation Rate Indicator. *Astronomical Journal*, 127:2002–2030, April 2004. vii, 62, 109, 117, 118

L. J. Kewley, B. Groves, G. Kauffmann, and T. Heckman. The host galaxies and classification of active galactic nuclei. *Mon. Not. R. A. S.*, 372:961–976, November 2006. 98

L. J. Kewley, D. Rupke, H. Jabran Zahid, M. J. Geller, and E. J. Barton. Metallicity Gradients and Gas Flows in Galaxy Pairs. *Astrophysical Journal*, 721:L48–L52, September 2010. 111

H. A. Kobulnicky and L. J. Kewley. Metallicities of $0.3 < z < 1.0$ Galaxies in the GOODS-North Field. *Astrophysical Journal*, 617:240–261, December 2004. 88, 91, 102

H. A. Kobulnicky and A. C. Phillips. Measuring Global Galaxy Metallicities Using Emission-Line Equivalent Widths. *Astrophysical Journal*, 599:1031–1042, December 2003. 95

H. A. Kobulnicky, R. C. Kennicutt, Jr., and J. L. Pizagno. On Measuring Nebular Chemical Abundances in Distant Galaxies Using Global Emission-Line Spectra. *Astrophysical Journal*, 514:544–557, April 1999. 105

H. A. Kobulnicky, C. N. A. Willmer, A. C. Phillips, D. C. Koo, S. M. Faber, B. J. Weiner, V. L. Sarajedini, L. Simard, and N. P. Vogt. The DEEP Groth Strip Survey. VII. The Metallicity of Field Galaxies at $0.26 < z < 0.82$ and the Evolution of the Luminosity-Metallicity Relation. *Astrophysical Journal*, 599:1006–1030, December 2003. 109, 114

E. Komatsu, J. Dunkley, M. R. Nolta, C. L. Bennett, B. Gold, G. Hinshaw, N. Jarosik, D. Larson, M. Limon, L. Page, D. N. Spergel, M. Halpern, R. S. Hill, A. Kogut, S. S. Meyer, G. S. Tucker, J. L. Weiland, E. Wollack, and E. L. Wright. Five-Year Wilkinson Microwave Anisotropy Probe Observations: Cosmological Interpretation. *ApJS*, 180:330–376, February 2009. 3, 54

E. Komatsu, K. M. Smith, J. Dunkley, C. L. Bennett, B. Gold, G. Hinshaw, N. Jarosik, D. Larson, M. R. Nolta, L. Page, D. N. Spergel, M. Halpern, R. S. Hill, A. Kogut, M. Limon, S. S. Meyer, N. Odegard, G. S. Tucker, J. L. Weiland, E. Wollack, and E. L. Wright. Seven-Year Wilkinson Microwave Anisotropy Probe (WMAP) Observations: Cosmological Interpretation. *ArXiv e-prints*, January 2010. 2

I. Labbé, R. Bouwens, G. D. Illingworth, and M. Franx. Spitzer IRAC Confirmation of z_{850}-Dropout Galaxies in the Hubble Ultra Deep Field: Stellar Masses and Ages at $z \sim 7$. *Astrophysical Journal*, 649:L67–L70, October 2006. 6

I. Labbé, V. González, R. J. Bouwens, G. D. Illingworth, M. Franx, M. Trenti, P. A. Oesch, P. G. van Dokkum, M. Stiavelli, C. M. Carollo, M. Kriek, and D. Magee. Star Formation Rates and Stellar Masses of z = 7-8 Galaxies from IRAC Observations of the WFC3/IR Early Release Science and the HUDF Fields. *Astrophysical Journal*, 716:L103–L108, June 2010. 6

F. Lamareille, M. Mouhcine, T. Contini, I. Lewis, and S. Maddox. The luminosity-metallicity relation in the local Universe from the 2dF Galaxy Redshift Survey. *Mon. Not. R. A. S.*, 350:396–406, May 2004. 98, 99

F. Lamareille, J. Brinchmann, T. Contini, C. J. Walcher, S. Charlot, E. Pérez-Montero, G. Zamorani, L. Pozzetti, M. Bolzonella, B. Garilli, S. Paltani, A. Bongiorno, O. Le Fèvre, D. Bottini, V. Le Brun, D. Maccagni, R. Scaramella, M. Scodeggio, L. Tresse, G. Vettolani, A. Zanichelli, C. Adami, S. Arnouts, S. Bardelli, A. Cappi, P. Ciliegi, S. Foucaud, P. Franzetti, I. Gavignaud, L. Guzzo, O. Ilbert, A. Iovino, H. J. McCracken, B. Marano, C. Marinoni, A. Mazure, B. Meneux, R. Merighi, R. Pellò, A. Pollo, M. Radovich, D. Vergani, E. Zucca, A. Romano, A. Grado, and L. Limatola. Physical properties of galaxies and their evolution in the VIMOS VLT Deep Survey. I. The evolution of the mass-metallicity relation up to z $\sim$ 0.9. *A&A*, 495:53–72, February 2009. 88, 93, 98, 99, 114

J. C. Lee, A. Gil de Paz, C. Tremonti, R. C. Kennicutt, S. Salim, M. Bothwell, D. Calzetti, J. Dalcanton, D. Dale, C. Engelbracht, S. J. J. G. Funes, B. Johnson, S. Sakai, E. Skillman, L. van Zee, F. Walter, and D. Weisz. Comparison of Hα and UV Star Formation Rates in the Local Volume: Systematic Discrepancies for Dwarf Galaxies. *Astrophysical Journal*, 706: 599–613, November 2009. 116

M. D. Lehnert and T. M. Heckman. The Nature of Starburst Galaxies. *Astrophysical Journal*, 472:546–+, December 1996. 47, 125

C. Leitherer, C. Robert, and T. M. Heckman. Atlas of Synthetic Ultraviolet Spectra of Massive Star Populations. *ApJS*, 99:173–+, July 1995. 130

M. Lemoine-Busserolle, T. Contini, R. Pelló, J.-F. Le Borgne, J.-P. Kneib, and C. Lidman. Physical properties of two low-luminosity $z \sim 1.9$ galaxies behind the lensing cluster AC 114. *A&A*, 397:839–849, January 2003. 103

S. J. Lilly, O. Le Fevre, F. Hammer, and D. Crampton. The Canada-France Redshift Survey: The Luminosity Density and Star Formation History of the Universe to Z approximately 1. *Astrophysical Journal*, 460:L1+, March 1996. 116

S. J. Lilly, C. M. Carollo, and A. N. Stockton. The Metallicities of Star-forming Galaxies at Intermediate Redshifts $0.47 < z < 0.92$. *Astrophysical Journal*, 597:730–750, November 2003. 103

M. Limousin, J. Richard, E. Jullo, J.-P. Kneib, B. Fort, G. Soucail, A. Eliasdottir, P. Natarajan, R. S. Ellis, I. Smail, O. Czoske, G. P. Smith, P. Hudelot,

S. Bardeau, H. Ebeling, E. Egami, and K. K. Knudsen. Combining Strong and Weak Gravitational Lensing in Abell 1689. *Astrophysical Journal*, 668: 643–666, October 2007. 14

X. Liu, A. E. Shapley, A. L. Coil, J. Brinchmann, and C.-P. Ma. Metallicities and Physical Conditions in Star-forming Galaxies at z $\sim$ 1.0-1.5. *Astrophysical Journal*, 678:758–779, May 2008. 114

A. Loeb. The Frontier of Reionization: Theory and Forthcoming Observations. *ArXiv e-prints*, 711, November 2007. 2, 4

P. Madau. Radiative transfer in a clumpy universe: The colors of high-redshift galaxies. *Astrophysical Journal*, 441:18, 1995. 50, 57

R. Maiolino, T. Nagao, A. Grazian, F. Cocchia, A. Marconi, F. Mannucci, A. Cimatti, A. Pipino, S. Ballero, F. Calura, C. Chiappini, A. Fontana, G. L. Granato, F. Matteucci, G. Pastorini, L. Pentericci, G. Risaliti, M. Salvati, and L. Silva. AMAZE. I. The evolution of the mass-metallicity relation at z $>$ 3. *A&A*, 488:463–479, September 2008. 114

S. Malhotra and PEARS collaboration. Pears: Probing Evolution And Reionization Spectroscopically. In *Bulletin of the American Astronomical Society*, volume 38 of *Bulletin of the American Astronomical Society*, pages 104–+, May 2007. 20, 75

S. Malhotra and J. E. Rhoads. Luminosity Functions of Lyα Emitters at Redshifts z=6.5 and z=5.7: Evidence against Reionization at z<=6.5. *Astrophysical Journal*, 617:L5–L8, December 2004. 3

S. Malhotra and J. E. Rhoads. The Volume Fraction of Ionized Intergalactic Gas at Redshift z=6.5. *Astrophysical Journal*, 647:L95–L98, August 2006. 54

C. B. Markwardt. Non-linear Least-squares Fitting in IDL with MPFIT. In D. A. Bohlender, D. Durand, & P. Dowler, editor, *Astronomical Society of the Pacific Conference Series*, volume 411 of *Astronomical Society of the Pacific Conference Series*, pages 251–+, September 2009. 87

J. M. Mas-Hesse, D. Kunth, G. Tenorio-Tagle, C. Leitherer, R. J. Terlevich, and E. Terlevich. Lyα Emission in Starbursts: Implications for Galaxies at High Redshift. *Astrophysical Journal*, 598:858–877, December 2003. 47

Y. Matsuda, T. Yamada, T. Hayashino, H. Tamura, R. Yamauchi, T. Murayama, T. Nagao, K. Ohta, S. Okamura, M. Ouchi, K. Shimasaku, Y. Shioya, and Y. Taniguchi. Large-Scale Filamentary Structure around the Protocluster at Redshift z = 3.1. *Astrophysical Journal*, 634:L125–L128, December 2005. 55

Y. Matsuda, J. Richard, I. Smail, N. Kashikawa, K. Shimasaku, B. L. Frye, T. Yamada, Y. Nakamura, T. Hayashino, and T. Fujii. A search for galaxies in and around an HI overdense region at z = 5. *Mon. Not. R. A. S.*, 403: L54–L58, March 2010. 55, 137

S. S. McGaugh. H II region abundances - Model oxygen line ratios. *Astrophysical Journal*, 380:140–150, October 1991. 88, 102

M. McQuinn. Promising Observational Methods for Detecting the Epoch of Reionization. *ArXiv e-prints*, March 2010. 54

G. R. Meurer, Z. I. Tsvetanov, C. Gronwall, P. Capak, J. P. Blakeslee, N. Benítez, H. C. Ford, G. D. Illingworth, L. D. Bradley, N. Pirzkal, J. Walsh, R. J. Bouwens, and S. Srinivasan. Automated Selection and Characterization of Emission-Line Sources in Advanced Camera for Surveys Wide Field Camera Grism Data. *Astronomical Journal*, 134:77–95, July 2007. 21, 72, 138

S. Mieske, L. Infante, M. Hilker, G. Hertling, J. P. Blakeslee, N. Benítez, H. Ford, and K. Zekser. Discovery of two M 32 twins in Abell 1689. *A&A*, 430:L25–L28, January 2005. 71

J. Moustakas, R. C. Kennicutt, Jr., C. A. Tremonti, D. A. Dale, J.-D. T. Smith, and D. Calzetti. Optical Spectroscopy and Nebular Oxygen Abundances of the Spitzer/SINGS Galaxies. *ApJS*, 190:233–266, October 2010. 102, 107, 108

J. A. Muñoz and A. Loeb. Constraining the Minimum Mass of High-Redshift Galaxies and Their Contribution to the Ionization State of the IGM. *ArXiv e-prints*, October 2010. 5

T. Nagao, R. Maiolino, and A. Marconi. Gas metallicity diagnostics in star-forming galaxies. *A&A*, 459:85–101, November 2006. v, 88, 108, 109, 110, 112

R. Narayan and M. Bartelmann. Lectures on gravitational lensing. In *Proc. 1995 Jerusalem Winter School*, 1995. iv, 10, 11

N. P. H. Nesvadba, M. D. Lehnert, F. Eisenhauer, R. Genzel, S. Seitz, R. I. Davies, R. P. Saglia, D. Lutz, L. Tacconi, R. Bender, and R. Abuter. Lyman Break Galaxies under a Microscope: The Small-Scale Dynamics and Mass of an Arc in the Cluster 1E 0657-56. *Astrophysical Journal*, 650:661–668, October 2006. 121

J. B. Oke. Faint spectrophotometric standard stars. *Astronomical Journal*, 99:1621–1631, May 1990. 34, 41, 42

J. B. Oke and J. E. Gunn. Secondary standard stars for absolute spectrophotometry. *Astrophysical Journal*, 266:713–717, March 1983. 9, 58

J. B. Oke et al. The Keck Low-Resolution Imaging Spectrometer. *"PASP"*, 107:375, 1995. 122

D. Osterbrock. *The Astrophysics of Gaseous Nebulae and Active Galactic Nuclei.* Univ. Science Books, Mill Valley, 1989. 95, 96, 117

D. E. Osterbrock, J. P. Fulbright, A. R. Martel, M. J. Keane, S. C. Trager, and G. Basri. Night-Sky High-Resolution Spectral Atlas of OH and O2 Emission Lines for Echelle Spectrograph Wavelength Calibration. *PASP*, 108:277–+, March 1996. 32

B. E. J. Pagel, M. G. Edmunds, D. E. Blackwell, M. S. Chun, and G. Smith. On the composition of H II regions in southern galaxies. I - NGC 300 and 1365. *Mon. Not. R. A. S.*, 189:95–113, October 1979. 88, 101

C. Papovich, M. Dickinson, and H. C. Ferguson. The Stellar Populations and Evolution of Lyman Break Galaxies. *Astrophysical Journal*, 559:620–653, October 2001. 90

L. Pentericci, J. D. Kurk, H. J. A. Röttgering, G. K. Miley, W. van Breugel, C. L. Carilli, H. Ford, T. Heckman, P. McCarthy, and A. Moorwood. A search for clusters at high redshift. II. A proto cluster around a radio galaxy at z=2.16. *A&A*, 361:L25–L28, September 2000. 55

E. Pérez-Montero, G. F. Hägele, T. Contini, and Á. I. Díaz. Neon and argon optical emission lines in ionized gaseous nebulae: implications and applications. *Mon. Not. R. A. S.*, 381:125–135, October 2007. 110

E. Pérez-Montero, T. Contini, F. Lamareille, J. Brinchmann, C. J. Walcher, S. Charlot, M. Bolzonella, L. Pozzetti, D. Bottini, B. Garilli, V. Le Brun, O. Le Fèvre, D. Maccagni, R. Scaramella, M. Scodeggio, L. Tresse, G. Vettolani, A. Zanichelli, C. Adami, S. Arnouts, S. Bardelli, A. Cappi, P. Ciliegi, S. Foucaud, P. Franzetti, I. Gavignaud, L. Guzzo, O. Ilbert, A. Iovino, H. J. McCracken, B. Marano, C. Marinoni, A. Mazure, B. Meneux, R. Merighi, S. Paltani, R. Pellò, A. Pollo, M. Radovich, D. Vergani, G. Zamorani, and E. Zucca. Physical properties of galaxies and their evolution in the VIMOS VLT Deep Survey. II. Extending the mass-metallicity relation to the range z $\approx$ 0.89-1.24. *A&A*, 495:73–81, February 2009. 88, 98, 114

S. Perlmutter, G. Aldering, G. Goldhaber, R. A. Knop, P. Nugent, P. G. Castro, S. Deustua, S. Fabbro, A. Goobar, D. E. Groom, I. M. Hook, A. G. Kim, M. Y. Kim, J. C. Lee, N. J. Nunes, R. Pain, C. R. Pennypacker, R. Quimby, C. Lidman, R. S. Ellis, M. Irwin, R. G. McMahon, P. Ruiz-Lapuente, N. Walton, B. Schaefer, B. J. Boyle, A. V. Filippenko, T. Matheson, A. S. Fruchter, N. Panagia, H. J. M. Newberg, W. J. Couch, and The Supernova Cosmology Project. Measurements of Omega and Lambda from 42 High-Redshift Supernovae. *Astrophysical Journal*, 517:565–586, June 1999. 1

M. Pettini and B. E. J. Pagel. [OIII]/[NII] as an abundance indicator at high redshift. *Mon. Not. R. A. S.*, 348:L59–L63, March 2004. 101, 109

M. Pettini, C. C. Steidel, K. L. Adelberger, M. Dickinson, and M. Giavalisco. The Ultraviolet Spectrum of MS 1512-CB58: An Insight into Lyman-Break Galaxies. *Astrophysical Journal*, 528:96–107, January 2000. 129, 130

M. Pettini, A. E. Shapley, C. C. Steidel, J.-G. Cuby, M. Dickinson, A. F. M. Moorwood, K. L. Adelberger, and M. Giavalisco. The Rest-Frame Optical Spectra of Lyman Break Galaxies: Star Formation, Extinction, Abundances, and Kinematics. *Astrophysical Journal*, 554:981–1000, June 2001. 84, 86, 103

M. Pettini, S. A. Rix, C. C. Steidel, K. L. Adelberger, M. P. Hunt, and A. E. Shapley. New Observations of the Interstellar Medium in the Lyman Break Galaxy MS 1512-cB58. *Astrophysical Journal*, 569:742–757, April 2002. 47, 121

L. S. Pilyugin. Oxygen abundances in dwarf irregular galaxies and the metallicity-luminosity relationship. *A&A*, 374:412–420, August 2001. 101

L. S. Pilyugin and T. X. Thuan. Oxygen Abundance Determination in H II Regions: The Strong Line Intensities-Abundance Calibration Revisited. *Astrophysical Journal*, 631:231–243, September 2005. 101, 106

L. S. Pilyugin, J. M. Vílchez, and T. Contini. Oxygen and nitrogen abundances in nearby galaxies. Correlations between oxygen abundance and macroscopic properties. *A&A*, 425:849–869, October 2004. 108, 111

N. Pirzkal, C. Xu, S. Malhotra, J. E. Rhoads, A. M. Koekemoer, L. A. Moustakas, J. R. Walsh, R. A. Windhorst, E. Daddi, A. Cimatti, H. C. Ferguson, J. P. Gardner, C. Gronwall, Z. Haiman, M. Kümmel, N. Panagia, A. Pasquali, M. Stiavelli, S. di Serego Alighieri, Z. Tsvetanov, J. Vernet, and H. Yan. GRAPES, Grism Spectroscopy of the Hubble Ultra Deep Field: Description and Data Reduction. *ApJS*, 154:501–508, October 2004. 20, 75

N. Pirzkal, S. Malhotra, J. E. Rhoads, and C. Xu. Optical-to-Mid-Infrared Observations of Lyα Galaxies at z$\sim$5 in the Hubble Ultra Deep Field: A Young and Low-Mass Population. *Astrophysical Journal*, 667:49–59, September 2007. 59, 62, 75, 138

P. A. Price, A. Songaila, L. L. Cowie, J. Bell Burnell, E. Berger, A. Cucchiara, D. B. Fox, I. Hook, S. R. Kulkarni, B. Penprase, K. C. Roth, and B. Schmidt. Properties of a Gamma-Ray Burst Host Galaxy at z $\sim$ 5. *Astrophysical Journal*, 663:L57–L60, July 2007. 53

J. R. Pritchard, A. Loeb, and J. S. B. Wyithe. Constraining reionization using 21-cm observations in combination with CMB and Lyα forest data. *Mon. Not. R. A. S.*, 408:57–70, October 2010. 4

A. M. Quider, M. Pettini, A. E. Shapley, and C. C. Steidel. The ultraviolet spectrum of the gravitationally lensed galaxy 'the Cosmic Horseshoe': a close-up of a star-forming galaxy at z $\sim$ 2. *Mon. Not. R. A. S.*, 398:1263–1278, September 2009. 27, 125, 126, 128, 130

M. Rauch. The Lyman Alpha Forest in the Spectra of QSOs. *ARA&A*, 36: 267–316, 1998. 48

M. J. Rees and J. P. Ostriker. Cooling, dynamics and fragmentation of massive gas clouds - Clues to the masses and radii of galaxies and clusters. *Mon. Not. R. A. S.*, 179:541–559, June 1977. 4

R. Reyes, N. L. Zakamska, M. A. Strauss, J. Green, J. H. Krolik, Y. Shen, G. T. Richards, S. F. Anderson, and D. P. Schneider. Space Density of Optically Selected Type 2 Quasars. *Astronomical Journal*, 136:2373–2390, December 2008. 98

J. E. Rhoads, S. Malhotra, N. Pirzkal, M. Dickinson, S. Cohen, N. Grogin, N. Hathi, C. Xu, I. Ferreras, C. Gronwall, A. Koekemoer, M. Kümmel, G. Meurer, N. Panagia, A. Pasquali, R. Ryan, A. Straughn, J. Walsh, R. A. Windhorst, and H.-J. Yan. Spectroscopic Confirmation of Faint Lyman Break Galaxies Near Redshift Five in the Hubble Ultra Deep Field. *Astrophysical Journal*, 697:942–949, May 2009. 75

A. G. Riess, A. V. Filippenko, P. Challis, A. Clocchiatti, A. Diercks, P. M. Garnavich, R. L. Gilliland, C. J. Hogan, S. Jha, R. P. Kirshner, B. Leibundgut, M. M. Phillips, D. Reiss, B. P. Schmidt, R. A. Schommer, R. C. Smith, J. Spyromilio, C. Stubbs, N. B. Suntzeff, and J. Tonry. Observational Evidence from Supernovae for an Accelerating Universe and a Cosmological Constant. *Astronomical Journal*, 116:1009–1038, September 1998. 1

C. S. Rola, E. Terlevich, and R. J. Terlevich. New diagnostic methods for emission-line galaxies in deep surveys. *Mon. Not. R. A. S.*, 289:419–427, August 1997. 98

D. Rosa-González, E. Terlevich, and R. Terlevich. An empirical calibration of star formation rate estimators. *Mon. Not. R. A. S.*, 332:283–295, May 2002. 116

D. S. N. Rupke, L. J. Kewley, and L.-H. Chien. Gas-phase Oxygen Gradients in Strongly Interacting Galaxies. I. Early-stage Interactions. *Astrophysical Journal*, 723:1255–1271, November 2010. 111

S. Salim, R. M. Rich, S. Charlot, J. Brinchmann, B. D. Johnson, D. Schiminovich, M. Seibert, R. Mallery, T. M. Heckman, K. Forster, P. G. Friedman, D. C. Martin, P. Morrissey, S. G. Neff, T. Small, T. K. Wyder, L. Bianchi, J. Donas, Y.-W. Lee, B. F. Madore, B. Milliard, A. S. Szalay, B. Y. Welsh, and S. K. Yi. UV Star Formation Rates in the Local Universe. *ApJS*, 173: 267–292, December 2007. 93

E. E. Salpeter. The Luminosity Function and Stellar Evolution. *Astrophysical Journal*, 121:161–+, January 1955. 57, 93

B. D. Savage and J. S. Mathis. Observed properties of interstellar dust. *ARA&A*, 17:73–111, 1979. 96

P. Schneider. The amplification caused by gravitational bending of light. *A&A*, 140:119–124, November 1984. 13

A. E. Shapley, C. C. Steidel, M. Pettini, and K. L. Adelberger. Rest-Frame Ultraviolet Spectra of z $\sim$ 3 Lyman Break Galaxies. *Astrophysical Journal*, 588:65–89, May 2003. 45, 47, 50, 59, 123, 137, 140

A. E. Shapley, C. C. Steidel, M. Pettini, K. L. Adelberger, and D. K. Erb. The Direct Detection of Lyman Continuum Emission from Star-forming Galaxies at z$\sim$3. *Astrophysical Journal*, 651:688–703, November 2006. 4, 139

R. A. Shaw and R. J. Dufour. Software for the Analysis of Emission Line Nebulae. *PASP*, 107:896–+, September 1995. 89

B. Siana, H. I. Teplitz, H. C. Ferguson, T. M. Brown, M. Giavalisco, M. Dickinson, R.-R. Chary, D. F. de Mello, C. J. Conselice, C. R. Bridge, J. P. Gardner, J. W. Colbert, and C. Scarlata. A Deep Hubble Space Telescope Search for Escaping Lyman Continuum Flux at z $\sim$ 1.3: Evidence for an Evolving Ionizing Emissivity. *Astrophysical Journal*, 723:241–250, November 2010. 139, 140

J. Silk. On the fragmentation of cosmic gas clouds. I - The formation of galaxies and the first generation of stars. *Astrophysical Journal*, 211:638–648, February 1977. 4

I. Smail, A. M. Swinbank, J. Richard, H. Ebeling, J. . Kneib, A. C. Edge, D. Stark, R. S. Ellis, S. Dye, G. P. Smith, and C. Mullis. A very bright, highly magnified Lyman-break galaxy at z=3.07. *ArXiv Astrophysics e-prints*, November 2006. 121

A. Songaila. The Evolution of the Intergalactic Medium Transmission to Redshift 6. *Astronomical Journal*, 127:2598–2603, May 2004. 50, 51, 52

V. Springel, S. D. M. White, A. Jenkins, C. S. Frenk, N. Yoshida, L. Gao, J. Navarro, R. Thacker, D. Croton, J. Helly, J. A. Peacock, S. Cole, P. Thomas, H. Couchman, A. Evrard, J. Colberg, and F. Pearce. Simulations of the formation, evolution and clustering of galaxies and quasars. *"Nature"*, 435:629–636, June 2005. 5, 54

V. Springel, C. S. Frenk, and S. D. M. White. The large-scale structure of the Universe. *Nature*, 440:1137–1144, April 2006. iv, 5

C. C. Steidel, M. Giavalisco, M. Dickinson, and K. L. Adelberger. Spectroscopy of Lyman Break Galaxies in the Hubble Deep Field. *Astronomical Journal*, 112:352–+, August 1996a. 122, 123

C. C. Steidel, M. Giavalisco, M. Pettini, M. Dickinson, and K. L. Adelberger. Spectroscopic Confirmation of a Population of Normal Star-forming Galaxies at Redshifts Z $>$ 3. *Astrophysical Journal*, 462:L17+, May 1996b. 122, 123

C. C. Steidel, K. L. Adelberger, A. E. Shapley, M. Pettini, M. Dickinson, and M. Giavalisco. Lyα Imaging of a Proto-Cluster Region at <z>=3.09. *Astrophysical Journal*, 532:170–182, March 2000. 55

C. C. Steidel, M. Pettini, and K. L. Adelberger. Lyman-Continuum Emission from Galaxies at Z $\sim=$ 3.4. *Astrophysical Journal*, 546:665–671, January 2001. 4, 139

C. C. Steidel, K. L. Adelberger, A. E. Shapley, M. Pettini, M. Dickinson, and M. Giavalisco. Lyman Break Galaxies at Redshift z $\sim$ 3: Survey Description and Full Data Set. *Astrophysical Journal*, 592:728–754, August 2003. 20

D. Stern, S. A. Yost, M. E. Eckart, F. A. Harrison, D. J. Helfand, S. G. Djorgovski, S. Malhotra, and J. E. Rhoads. A Galaxy at z = 6.545 and Constraints on the Epoch of Reionization. *Astrophysical Journal*, 619:12–18, January 2005. 54

P. J. Storey and C. J. Zeippen. Theoretical values for the [Oiii] 5007/4959 line-intensity ratio and homologous cases. *Mon. Not. R. A. S.*, 312:813–816, March 2000. 84

A. M. Swinbank, R. G. Bower, G. P. Smith, R. J. Wilman, I. Smail, R. S. Ellis, S. L. Morris, and J.-P. Kneib. Resolved spectroscopy of a gravitationally lensed L* Lyman-break galaxy at z $\sim$ 5. *Mon. Not. R. A. S.*, 376:479–491, April 2007. 53, 54, 62

P. F. Teague, D. Carter, and P. M. Gray. The dynamics and structure of rich clusters of galaxies. I - Velocity data. *ApJS*, 72:715–753, April 1990. 71

T. Tepper-García and U. Fritze. Stochastic absorption of the light of background sources due to intergalactic neutral hydrogen - I. Testing different line-number evolution models via the cosmic flux decrement. *Mon. Not. R. A. S.*, 383:1671–1685, February 2008. 51

C. A. Tremonti, T. M. Heckman, G. Kauffmann, J. Brinchmann, S. Charlot, S. D. M. White, M. Seibert, E. W. Peng, D. J. Schlegel, A. Uomoto, M. Fukugita, and J. Brinkmann. The Origin of the Mass-Metallicity Relation: Insights from 53,000 Star-forming Galaxies in the Sloan Digital Sky Survey. *Astrophysical Journal*, 613:898–913, October 2004. 95, 110, 115, 123, 124, 134

K. Umetsu and T. Broadhurst. Combining Lens Distortion and Depletion to Map the Mass Distribution of A1689. *Astrophysical Journal*, 684:177–203, September 2008. 15

K. Umetsu, E. Medezinski, T. Broadhurst, A. Zitrin, N. Okabe, B.-C. Hsieh, and S. M. Molnar. The Mass Structure of the Galaxy Cluster Cl0024+1654 from a Full Lensing Analysis of Joint Subaru and ACS/NIC3 Observations. *Astrophysical Journal*, 714:1470–1496, May 2010. 15

P. M. Vreeswijk, S. L. Ellison, C. Ledoux, R. A. M. J. Wijers, J. P. U. Fynbo, P. Møller, A. Henden, J. Hjorth, G. Masi, E. Rol, B. L. Jensen, N. Tanvir, A. Levan, J. M. Castro Cerón, J. Gorosabel, A. J. Castro-Tirado, A. S. Fruchter, C. Kouveliotou, I. Burud, J. Rhoads, N. Masetti, E. Palazzi, E. Pian, H. Pedersen, L. Kaper, A. Gilmore, P. Kilmartin, J. V. Buckle, M. S. Seigar, D. H. Hartmann, K. Lindsay, and E. P. J. van den Heuvel. The host of GRB 030323 at z=3.372: A very high column density DLA system with a low metallicity. *A&A*, 419:927–940, June 2004. 53

D. Walsh, R. F. Carswell, and R. J. Weymann. 0957 + 561 A, B - Twin quasistellar objects or gravitational lens. *Nature*, 279:381–384, May 1979. 13

S. J. Warren, P. C. Hewett, G. F. Lewis, P. Moller, A. Iovino, and P. A. Shaver. A candidate optical Einstein ring. *Mon. Not. R. A. S.*, 278:139–145, January 1996. 26, 131

S. J. Warren, A. Iovino, P. C. Hewett, and P. A. Shaver. Spectroscopy of the optical Einstein ring 0047-2808. *Mon. Not. R. A. S.*, 299:1215–1219, October 1998. 26, 131

S. J. Warren, G. F. Lewis, P. C. Hewett, P. Møller, P. Shaver, and A. Iovino. A VLT colour image of the optical Einstein ring 0047-2808. *A&A*, 343: L35–L39, March 1999. 131

R. B. Wayth, S. J. Warren, G. F. Lewis, and P. C. Hewett. The lens and source of the optical Einstein ring gravitational lens ER 0047-2808. *Mon. Not. R. A. S.*, 360:1333–1344, July 2005. 131

S. D. M. White and M. J. Rees. Core condensation in heavy halos - A two-stage theory for galaxy formation and clustering. *Mon. Not. R. A. S.*, 183: 341–358, May 1978. 4

G. D. Wirth, C. N. A. Willmer, P. Amico, F. H. Chaffee, R. W. Goodrich, S. Kwok, J. E. Lyke, J. A. Mader, H. D. Tran, A. J. Barger, L. L. Cowie, P. Capak, A. L. Coil, M. C. Cooper, A. Conrad, M. Davis, S. M. Faber, E. M. Hu, D. C. Koo, D. Le Mignant, J. A. Newman, and A. Songaila. The Team Keck Treasury Redshift Survey of the GOODS-North Field. *Astronomical Journal*, 127:3121–3136, June 2004. 41

H. K. C. Yee, E. Ellingson, J. Bechtold, R. G. Carlberg, and J.-C. Cuillandre. A Proto-Galaxy Candidate at z=2.7 Discovered by its Young Stellar Population. *Astronomical Journal*, 111:1783–+, May 1996. 121

T.-T. Yuan and L. J. Kewley. First Direct Metallicity Measurement Of a Lensed Star-Forming Galaxy at z = 1.7. *Astrophysical Journal*, 699:L161–L164, July 2009. 100

D. Zaritsky, R. C. Kennicutt, Jr., and J. P. Huchra. H II regions and the abundance properties of spiral galaxies. *Astrophysical Journal*, 420:87–109, January 1994. 102, 106, 107, 108, 111